

MICROCOPY

CHART

2

HgCdTe SURFACE AND DEFECT STUDY PROGRAM

J. A. WILSON AND V. A. COTTON
Santa Barbara Research Center
Goleta, California 93117

J.A. Silberman, G. P. Carey, C. K. Shih, C. S. Stahl
D. J. Friedman, and W. E. Spicer
Stanford Electronics Laboratories
Stanford, California 94305

A. Sher and A. B. Chen
SRI International
Menlo Park, California

January 1985

DTIC
ELECTE
APR 22 1986
S D

FOURTH INTERIM TECHNICAL REPORT

CONTRACT No. MDA-903-83-C-0108

The views, opinions, and findings contained in this report are those of the authors and should not be construed as an official Department of Defense position, policy, or decision, unless so designated by other official documentation.

Prepared for:

DARPA
1400 Wilson Blvd.
Arlington, Virginia 22209
Attention: **Dr. J. Murphy**
Defense Science Office

DISTRIBUTION STATEMENT A
Approved for public release
Distribution Unlimited

CLEARED

FOR OPEN PUBLICATION

APR 17 1986 3

1370

UNCLASSIFIED FOR FREEDOM OF INFORMATION
AND SECURITY REVIEW (GASD-PA)
DEPARTMENT OF DEFENSE

~~86-4-22-182~~

86 4 22 182

AD-A166 793

DTIC FILE COPY

HgCdTe SURFACE AND DEFECT STUDY PROGRAM

J. A. WILSON AND V. A. COTTON
Santa Barbara Research Center
Goleta, California 93117

J.A. Silberman, G. P. Carey, C. K. Shih, C. S. Stahle
D. J. Friedman, and W. E. Spicer
Stanford Electronics Laboratories
Stanford, California 94305

A. Sher and A. B. Chen
SRI International
Menlo Park, California

January 1985

FOURTH INTERIM TECHNICAL REPORT

CONTRACT No. MDA-903-83-C-0108

The views, opinions, and findings contained in this report are those of the authors and should not be construed as an official Department of Defense position, policy, or decision, unless so designated by other official documentation.

Prepared for:

DARPA
1400 Wilson Blvd.
Arlington, Virginia 22209
Attention: **Dr. J. Murphy**
Defense Science Office

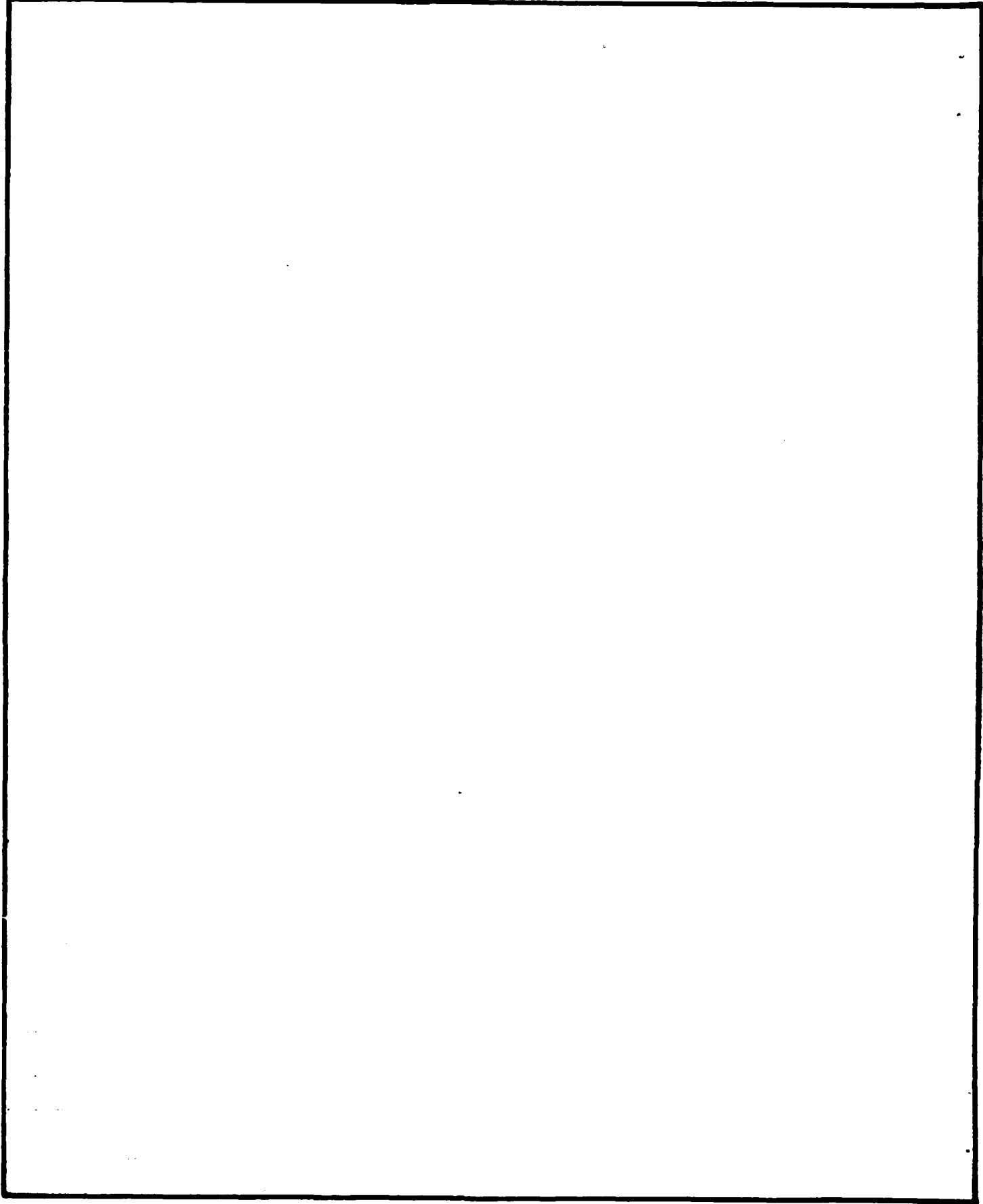
UNCLASSIFIED

SECURITY CLASSIFICATION OF THIS PAGE

REPORT DOCUMENTATION PAGE

1a. REPORT SECURITY CLASSIFICATION UNCLASSIFIED		1b. RESTRICTIVE MARKINGS	
2a. SECURITY CLASSIFICATION AUTHORITY		3. DISTRIBUTION/AVAILABILITY OF REPORT	
2b. DECLASSIFICATION/DOWNGRADING SCHEDULE			
4. PERFORMING ORGANIZATION REPORT NUMBER(S) RPT52871		5. MONITORING ORGANIZATION REPORT NUMBER(S)	
6a. NAME OF PERFORMING ORGANIZATION SANTA BARBARA RESEARCH CENTER	6b. OFFICE SYMBOL (If applicable)	7a. NAME OF MONITORING ORGANIZATION DARPA/DSO	
6c. ADDRESS (City, State and ZIP Code) 75 Coromar Dr Goleta, CA 93117		7b. ADDRESS (City, State and ZIP Code) 1400 Wilson Blvd Arlington, VA 22209	
8a. NAME OF FUNDING/SPONSORING ORGANIZATION DARPA/DSO	8b. OFFICE SYMBOL (If applicable)	9. PROCUREMENT INSTRUMENT IDENTIFICATION NUMBER	
8c. ADDRESS (City, State and ZIP Code) 1400 Wilson Blvd Arlington, VA 22209		10. SOURCE OF FUNDING NOS.	
		PROGRAM ELEMENT NO.	TASK NO.
		PROJECT NO.	WORK UNIT NO.
11. TITLE (Include Security Classification) HgCdTe Surface and Defect Study Program			
12. PERSONAL AUTHOR(S) Wilson, J.A.; Cotton, V.A.			
13a. TYPE OF REPORT Interim Technical	13b. TIME COVERED FROM 7/1/84 TO 12/31/84	14. DATE OF REPORT (Yr., Mo., Day) January 1985	15. PAGE COUNT
16. SUPPLEMENTARY NOTATION Authors of papers included in this report: Silberman, J.A.; Carey, G.P.; Shih, C.K.; Stahle, C.S.; Sher, A.; and Chen, A.B.			
17. COSATI CODES		18. SUBJECT TERMS (Continue on reverse if necessary and identify by block number)	
FIELD	GROUP	HgCdTe, HgTe, CdTe, II-VI alloys, photoelectron spectroscopy, surfaces, defects, electronic structure, interface, storage time, minority carrier lifetime.	
19. ABSTRACT (Continue on reverse if necessary and identify by block number) This report presents program results for the six-month period ending January 1, 1985. Measurements of MIS storage time at the PHOTOX SiO ₂ /Hg _{0.7} Cd _{0.3} Te interface indicate that minority carrier lifetime is bulk rather than surface limited, and is nonuniformly distributed. DLTS of ion-implanted wafers reveal a single bulk trap at E = E _c - 0.20 eV (E _g = 0.26 eV at 77K), which is associated with the resultant lattice damage. Continuing studies of the initial stages of oxidation reveal that the reaction occurring at the surface is not directly photon assisted. Initial PES characterization of the alteration of surface structure and composition by chemical processes is presented. Data showing precise removal of Hg from the surface using an incident electron beam is also presented. An initial study of the reaction chemistry between Ag and Al and the HgCdTe surface is described. Finally, the sensitivity of defect energy levels in semiconductors to the host band structures and impurity potentials have been studied for approximately 30 impurities in CdTe using four different band structure models. <i>Keywords:</i>			
20. DISTRIBUTION/AVAILABILITY OF ABSTRACT UNCLASSIFIED/UNLIMITED <input checked="" type="checkbox"/> SAME AS RPT. <input type="checkbox"/> OTIC USERS <input type="checkbox"/>		21. ABSTRACT SECURITY CLASSIFICATION UNCLASSIFIED	
22a. NAME OF RESPONSIBLE INDIVIDUAL		22b. TELEPHONE NUMBER (Include Area Code)	22c. OFFICE SYMBOL

SECURITY CLASSIFICATION OF THIS PAGE



SECURITY CLASSIFICATION OF THIS PAGE

SUMMARY

Measurements of MIS storage times, [proportional to minority carrier (hole) lifetime] in n-type $Hg_{0.7}Cd_{0.3}Te$ indicate values that range from less than 1.5 ms up to 10^3 sec. Amplitude of the structure seen in capacitance and conductance versus bias curves taken when the interface region is inverted correlate inversely with measured storage times. This correlation combined with the lack of correlation of storage time with interface trap or donor impurity concentration suggest that lifetime is fundamentally limited by bulk defects rather than interface properties.

Trap levels associated with random (nonchanneled) ion implantation in $Hg_{1-x}Cd_xTe$ ($x \approx 0.3$) have been characterized for the first time using deep level transient spectroscopy (DLTS), secondary ion mass spectroscopy (SIMS), and high-frequency (1 MHz) capacitance voltage (CV) techniques. A deep level trap with an activation energy (E_t) of $E_c - 0.20$ eV and capture cross section (σ_n) of $9.2 \times 10^{-20} \text{ cm}^{-2}$ has been seen in samples implanted with 200 keV chlorine. The trap concentration with depth, from DLTS profiling, is five times the ion concentration as measured by SIMS. The resulting donor concentration measured by CV is increased over the ion concentration by a factor of about 100. Another state is seen at 0.053 eV, which is thought to be associated with interface traps. These results indicate that separate mechanisms producing the deep trap level and the donor activity are caused by lattice distortion and atomic displacement due to the implant process.

Comparison of photoelectron spectra of the clean as-cleaved surface, the surface exposed with the direct path for activated oxygen blocked by a lithium fluoride (LiF) window, and the surface subsequently exposed to oxygen with the window removed so as to permit straight line travel to the surface for oxygen excited by a hot filament indicate that no oxidation occurs when the radiation and oxygen ambient are present, but the fact that the line-of-sight path for excited atoms or molecules is removed demonstrates that an excited species rather than thermal or photoexcited effects is responsible for the activated uptake of oxygen. Based on our previous work this particle must also be neutral.

It is also possible that the high-temperature filament catalyzes reactions between O_2 and molecules in the background gas to generate excited

<input checked="" type="checkbox"/>
<input type="checkbox"/>
<input type="checkbox"/>

Set on file



Dist	Special
A-1	

molecules of oxygen containing species such as CO_2 or H_2O . These synthesized molecules would have to gain activity due to excitation since the sample would not be expected to show such a strong dependence on the line-of-sight nature of the exposure. An experiment to probe this possibility by the application of mass spectroscopy to the flux of particles leaving the filament is planned for future work.

Initial conclusions can be drawn at this point in our continuing study of HgCdTe surfaces that are prepared for subsequent passivation. The etching and cleaning techniques used clearly alter the surface. Three main conclusions concerning this change of the surface are:

1. Independent of material growth, or technique of surface preparation, the valence band electronic structures of the resulting surfaces are altered from that of atomically clean surfaces and show increased emission, probably due to O and C contamination and/or oxidized TeO_2 or elemental Te.
2. All of the samples studied exhibited n-type surface behavior subsequent to the surface preparations including bulk p-type material.
3. All but one of the approximately dozen samples was Cd deficient after surface preparation. One explanation of the first sample's Cd increase could be that different (111) faces were studied, either the Cd or Te (A or B) terminated face.

Although these experiments have shed some light on the effects of surface preparation on HgCdTe, there is still great uncertainty and many questions need to be answered. Results from exposure to ultraviolet light suggest a possible method for cleaning surface contaminants such as carbon and oxygen.

Electron beam heating effect plays a major role in the electron beam-induced Hg desorption (we don't exclude the possibility that electronic excitation may be incorporated in the bond-breaking process). Hg depletion saturates after a few monolayers are depleted of Hg, leaving the surface with excess Te. The surface Te layer may act as an activation barrier for the outdiffusion of the Hg atoms from the subsurface to the surface.

A study of metal contacts on HgCdTe was begun. Employing thermodynamic guidelines, Ag and Al were chosen as examples of nonreactive and reactive candidate metals. As expected, deposition of Al causes a depletion of Hg from the surface of the semiconductor. The Ag/Hg_{1-x}Cd_xTe interface, on the other hand, shows little evidence for chemical reaction. There is also little if

any Hg depletion. However, the Ag does not go on in a simple, laminar manner; rather, it appears to form islands at low coverages.

Sensitivity of defect energy levels in semiconductors to the host band structures and impurity potentials has been studied for approximately 30 impurities in CdTe using four different band structure models. The discrepancies in the defect levels between two different sets of band structures and impurity potentials are found to range from less than 0.1 eV to the whole band gap (1.6 eV). The band-structure effects are analyzed here in terms of detailed partial densities of states. Examples of contradictory predictions from different band structures are illustrated, and ways to improve the theory are suggested.

ACKNOWLEDGEMENTS

We wish to acknowledge many helpful discussions with T.N. Casselman and C.E. Jones. We especially acknowledge the technical assistance of R.E. Cole and C.R. Curtis for bulk crystal growth and M.S. Langell for wafer preparation and MIS fabrication and M.E. Boyd and J.F. Santarosa for technical assistance in recording capacitance data.

We are also appreciative of the many collaborations which have aided this work, specifically; W.A. Harrison, A.B. Chen, F. Pollak and S. Perkowitz. Finally, we are grateful for the support and encouragement of the program sponsors R.A. Reynolds and J. Murphy of DARPA/DSO.

CONTENTS

<u>Section</u>	<u>Page</u>
INTRODUCTION.....	1
I Interface Study.....	9
Storage Time at the HgCdte - SiO ₂ Interface.....	9
II Channeled Implants.....	25
Carrier Trapping Centers in Randomly Implanted HgCdTe.....	25
III Surface Study.....	33
Investigation into the Nature of Excited Oxygen.....	35
Photoemission Studies of Technologically Important Surfaces of HgCdTe.....	43
Electron Beam Induced Hg Desorption Study on Hg _{1-x} Cd _x Te.....	69
Metals on Hg _{1-x} Cd _x Te.....	79
IV Alloy Bonding.....	83
Sensitivity of Defect Energy Levels to Host Band Structures..	83



SANTA BARBARA RESEARCH CENTER
a subsidiary

(This page left intentionally blank)

INTRODUCTION

The objective of this program is to develop a detailed understanding of the physical processes that dominate HgCdTe surfaces and interfaces, particularly the passivated interface incorporated in an MIS device made with PHOTOX™ SiO₂ on MWIR HgCdTe. The program has also relied on measurements of the effects of this interface on photovoltaic (PV) device performance, particularly R₀A, to decide which interface properties were of the greatest significance and, therefore, most important to quantify and eventually control. The simplicity of the fabrication of an MIS device has allowed us to separate individual effects and examine each in greater detail than if we were to deconvolute the more complicated interaction between the surface and junction regions in a detector. As discussed in previous reports, the total or net interface charge plays a prominent, if not actually a dominant, role in controlling surface leakage in double-layer heterojunction devices (DLHJ). Recall that this charge consists of fixed charge, interface trap charge and relatively slowly responding charge sites in the PHOTOX™ SiO₂ itself. None of these sources can be ignored. Depending on the device design and the device processing steps, each one can individually or collectively determine the size of the surface leakage.

The interface charge is very important because, depending on device design, it can be optimized to drive carriers away from or attract them to the surface. Thus, it turns on or off certain leakage mechanisms at the interface. In the case of n⁺ on p junctions, for example, if the lower doped p side is accumulated the surface junction will be pinched off, allowing an increased probability of surface leakage by trap tunneling, using interface traps. There are, of course, other mechanisms that complicate this picture, but to first order, passivation is achieved not by actually passivating the surface but by keeping carriers away from it. In some cases, as in, for example, DLHJ with similar composition and doping on each side of the junction, it will not be possible to optimize the interface charge so as to prevent carriers from reaching the interface on both sides of the junction at once. In this case, the separate contributing leakage mechanisms must be fixed. An effective passivation of the surface is also obtained if the interface is inaccessible in all cases due to a significant widening of the band gap at the HgCdTe surface. This may in principle be obtained with CdTe grown

on the HgCdTe, and the possibility is being investigated at SBRC. It remains to be seen whether the transition of the bandgap from HgCdTe to CdTe is monotonic across the grown metallurgical junction. It may narrow, due to cation loss at high-growth temperatures, and then widen. This would defeat the passivation and produce a buried leakage channel.

The interface properties that affect device properties are those of the final interface after all the processing necessary to produce a focal plane array (FPA) has been completed. We take this interface to be completely characterized when the surface band gap ($E_{g,s}$), surface fermi energy ($E_{f,s}$), net interface charge (Q_{net}) and the interface traps (density, D_{it} ; capture cross section, σ_{it} and response time τ_{it}) are specified. Some of these interface properties, such as $E_{g,s}$ and $E_{f,s}$ are cumulative or essentially completely determined on a microscopic level before the final interface is formed. The others, D_{it} and Q_{net} are not directly cumulative, and therefore cannot be evaluated before the interface is completed. These noncumulative properties can also be subsequently altered by chemical action, radiation damage, or other mechanisms which have access to the interface after it is formed. For example, water reversibly alters both D_{it} and Q_{net} by entering through the PHOTOX™ SiO₂ porosity.

Interface trap density, capture cross-section and response times are completely determined by the detailed bonding at the final interface and bear no direct correlation to interface trap structure at any intermediate stage. The final structure is, however, indirectly determined by previous surface conditions, namely the chemical constituents which are available for bonding with the depositing PHOTOX™ SiO₂ insulator. These previous surface conditions include a probably nonstoichiometric surface region with a thin Te-oxide layer. As discussed in previous reports, this oxide is reduced by the PHOTOX™ SiO₂ deposition so that the final interface region is composed of an intermediate layer of silicon, oxygen, and tellurium. It is the detailed bonding from the PHOTOX™ SiO₂ to the intermediate layer and this to the HgCdTe that determine D_{it} and Q_{net} . The chemical precursors of this interface is the topic being addressed by the oxidation studies done jointly between SBRC and the Stanford group and reported in Section II. The electronic structure of the actual interface is the topic of the interface study task at SBRC and reported in Section I.

Recent work on this program and by other groups indicate that $E_{g,s}$ and $E_{f,s}$ are significantly different than the bulk values. The transition to bulk values also may occur over distances that are electronically significant (10^2 to 10^3 \AA). These nonbulk values are caused by changes in stoichiometry or changes even to nonalloy compositions caused by cation removal during polish or etch steps required for device processing. The surface band gap, if the surface has a band gap, is for all practical purposes completely determined before the PHOTOX™ SiO_2 is deposited. At least, any deep tail is completely determined. The same alteration of cation concentration will affect $|N_D - N_A|$ and therefore $E_{f,s}$, and any deep tail it has, in the same way. In this case it is not only instructive but critical to determine both the surface values and their transition with depth to bulk values on the pre-PHOTOX™ SiO_2 surface. The PHOTOX™ SiO_2 reaction itself has been shown to be capable^{1,2} of reducing 15 to 20 Å of native oxide on the HgCdTe surface and possibly altering the very local ($\sim 5 \text{ \AA}$) surface composition. The reaction is expected to make only slight alterations in an already established $E_{g,s}$ and also $E_{f,s}$, although it is possible to generate high enough concentrations of local surface states to alter or pin $E_{f,s}$. "Local" means "within a few monolayers." The exact composition of the local surface has not been established. It is not known whether the surface has an alloy composition or even an intact Te lattice at the surface. These issues are the basis of the photoemission measurement being done at Stanford in collaboration with SBRC and are reported in Section III.

The deepest portion of a transition from surface to bulk values of electronic structure is most effectively probed with direct measurement of electronic structure such as trap levels. This is done with DLTS, capacitance-voltage and admittance measurement. The DLTS signal in an MIS device comes primarily from deep states in the depletion region, although interface traps may also be detected. The capacitance technique allows measurement of the doping profile across the depletion region, and measurement of true interface traps, as does admittance. Thus the "bulk" deep states can be separated from true interface traps, and doping and trap density profiles determined and compared to models of the transition from surface to bulk structure. Several bulk trap properties may vary as the surface is approached and therefore qualify as probes. These include activation energy, E_A (some traps follow the conduction band edge, some the valence, and others may remain at a fixed

percentage of E_g depending on whether it is an impurity on the cation or anion site or a native defect) capture cross section, σ , and concentration. Progress on this continuing effort was reported in Section I, Appendix A of the Third Interim Technical Report (previous).

Results of the measurement of $E_{f,s}$ relative to the valence band maximum (VBM) made to date, have shown two important results. First, regardless of the bulk carrier concentration, $E_{f,s}$ is 0.15 eV above VBM. This is on measurements of the etched pre-PHOTOX™ SiO_2 surface made at room temperature. The sample x value is 0.3 so that bulk E_g is 0.29 eV. Second, by taking the area under the Hg, Cd and Te core levels the surface is seen to be depleted in Cd. If we assume that the surface recrystallizes to utilize all the available cations, then the x value of the surface is seen to be about 0.2 ($E_{g,s} = 0.15$ eV at 300K), with an excess of unalloyed Te. Excess Te has also been indicated on these types of surfaces by ellipsometry done at SBRC.

The first result indicates that the free surface may pin $E_{f,s}$. Once the PHOTOX™ SiO_2 has been deposited, a very different situation may occur. In fact, since the amount of interface charge seen at PHOTOX™ $\text{SiO}_2/\text{HgCdTe}$ interfaces does depend on whether the semiconductor is n- or p-type, we do not expect interface pinning of $E_{f,s}$. Also, no large densities of interface traps in the region of 0.15 eV above the VBM have been detected by admittance or C-V. This value of $E_{f,s}$ is therefore, not the same as that governing the filling of interface traps at the passivated interface. What happens to $E_{f,s}$ as the PHOTOX™ SiO_2 reaction begins and proceeds will, however, be instructive. As is the case of III -V interfaces, the final interface values are likely to be obtained within a very few deposited monolayers of PHOTOX™ SiO_2 over the reduced oxide and may well be within the escape depth of XPS measurements.

The second result indicates a pronounced narrowing of E_g at the surface. This narrowing is undoubtedly due to the reformation or rebonding of the surface after the etch-induced cation loss and is not likely to be altered by PHOTOX™ SiO_2 deposition. The surface gap has not been directly measured by this technique since photoemission measures the kinetic energy of electrons excited from states in the material surface. At the conditions under which this experiment was done the conduction band is unoccupied or the density of states is so low that there are essentially no electrons to excite. Nevertheless, the indirect evidence for $E_{g,s}$ being smaller than E_g is strong. Bandgap

narrowing is exactly the opposite effect required to keep carriers away from the surface region, increasing the problem of passivation.

If the proportion of narrowing is similar at all x values, then the LWIR ($x \sim 0.2$) HgCdTe surface will be so depleted in cations that the resulting equivalent alloy will be metallic or semimetallic ($x < 0.17$), and hence could offer a direct conduction leakage path. The depth to which this effect occurs will be of critical importance here. The photoelectron spectrometry (PES) results on MWIR are applicable to the first 10 to 15Å of the surface. The point here is that LWIR material may respond to passivation processes to produce a fundamentally different result than does MWIR material, and LWIR should in fact be treated as a completely different material. These results are discussed at greater length in Section I.

Interfaces made on implanted MWIR HgCdTe also appear to be fundamentally different from those made on unimplanted material. These indications come from measurements of the current voltage characteristics of gated junctions made with B⁺ implants, as discussed in two previous reports, and from capacitance voltage measurements of MIS devices made on implanted surfaces. In both cases, no post-implant anneal was used, so that we are dealing with the implant-damaged lattice. Post-implant anneals have yet to be proven useful in HgCdTe. In the case of implantation into Si, the lattice is well enough behaved that actual remelting and subsequent recrystallization of an implanted surface results in a very closely controlled doping profile in a high quality lattice. This fortuitous result has made implants in Si the method of choice for high tolerance doping and allows very intricate device designs. This situation is in strong contrast to the case of implanted HgCdTe in which every form of post implant anneal so far examined has produced unacceptable levels of Hg loss (heat pulse, laser annealed, or SiO₂ capped thermal anneal) or has caused junction diffusion (isothermal Hg vapor anneal).

The as implanted surface, when passivated with PHOTOX™ SiO₂ shows a high density of deep traps in the implanted region as well as densities of interface traps so high (in excess of $1 \times 10^{12} \text{ cm}^{-2} \text{ eV}^{-1}$) that quasistatic capacitance voltage measurements are not possible. Channeling to avoid the major amount of lattice damage may produce acceptable interfaces once the random component near to the surface has been either eliminated or removed. In any event, passivating the surface of junction devices formed by nonchanneled or

random implants must be treated as a separate and more complicated problem from that of passivating grown heterojunctions in the same composition material. The continuing investigation of doping with channeled implants and characterization of the implanted interface with PHOTOX™ SiO₂ is discussed in Section II. The implants are done at Hughes Research Laboratories and characterized at SBRC.

The particular ease of cation removal in HgCdTe is directly responsible for the composition alterations seen after etches which determine $E_{g,s}$, $E_{f,s}$ and establish the chemical environment for oxidation reactions and interaction with the PHOTOX™ SiO₂ deposition process. The bonding mechanism which leads to the ease of cation removal has been investigated theoretically on this study. It has been determined that the ionic portion of the CdTe bond has weakened the HgTe bond and thus destabilized the lattice. The same bonding model has indicated that replacement of Cd by Zn will greatly reduce the tendency towards destabilization. The theoretical bonding model has also given understanding of the alloys' hardness. This effort is now focused on estimating the activation energy and energy levels (deep states) of cation vacancy point defects. This work is conducted at SRI International and reported in Section IV.

REFERENCES

1. Rhiger, D.R., and Kvaas, R.E., Second Interim Technical Report, Contract No. F33615-80-C-5084, "Exploratory Development on PV HgCdTe Surface Leakage", SBRC, 29 November 1982, Section 3.
2. Rhiger, D.R., and Kvaas, R.E., J. Vac Sci. Technol., 21, 448 (1982).

(This page left intentionally blank)

Section I
INTERFACE STUDYStorage Time at the HgCdTe-SiO₂ InterfaceJ.A. Wilson and V.A. Cotton
Santa Barbara Research Center, Goleta CA, 93117

ABSTRACT

The storage time was measured in MIS devices made with PHOTOX™ SiO₂ on n-type Hg_{1-x}Cd_xTe (x = 0.3). These storage times range from less than the measurement limit of 1.5 ms to, in one case, 1430 sec. Interface state density and structure as well as doping density of the bulk wafer varied only slightly from sample to sample, indicating that the wide variation of storage time was not due to interface states or residual active donor impurities. Behavior of the capacitance and conductance versus bias curves shows a dependence of actual storage time on gate bias in inversion and therefore a dependence with depth from the interface. Samples which show longer storage times reveal a lower concentration of locally effective bulk g-r centers. The lower concentration is attributed to lattice defects resulting from damage produced in device fabrication or residual defects from crystal growth.

INTRODUCTION

Semiconductor surfaces generally require some form of passivation so that bulk electronic properties dominate device performance instead of those properties due to the broken symmetries and defects associated with real surfaces. One of the most important effects that a poorly passivated surface or interface can manifest is to severely shorten the minority carrier lifetime. Shortened lifetime occurs by carrier recombination through deep midgap traps that can be located either in the bulk or at the surface.¹ In the case of the passivation of HgCdTe, there are enhanced opportunities for defect formation beyond those normally seen in simpler semiconductor systems such as elemental or binary compound materials. These opportunities occur because Hg is particularly weakly bound in the alloy, resulting in an extremely low resistance to defect formation.² Also since the material is a ternary alloy, defect formation can occur through distortion of the surface stoichiometry.³⁻⁷

We have measured the interface region minority carrier lifetime in HgCdTe

($x = 0.3$) wafers by measuring the inversion layer storage time in MIS devices.⁸ Bulk lifetimes are seen to vary over a wide range from wafer to wafer with very long lifetimes seen on a few samples. In the case of wafers with long lifetimes, regions below the interface with shorter lifetimes can be seen. The generation-recombination (g-r) sites active in causing this locally limited lifetime are seen to be deep bulk traps which are active below the interface. These traps are believed to be due to defects in the crystal structure produced either by the surface processing used in device fabrication or due to grown-in defects. Actual interface traps were not found to play the dominant role.

SAMPLE PREPARATION AND MEASUREMENT

The MIS devices used were made with 1500Å of PHOTOX™ SiO₂ deposited in a single layer on the surface of horizontal-zone melt-grown wafers of Hg_{0.7}Cd_{0.3}Te. Prior to insulator deposition, the wafers were polished and etched in Br₂ in dimethylformamide and Br₂ in ethylene glycol in separate steps. Each wafer had been annealed isothermally in Hg vapor to lower the native defect (cation vacancy) acceptor level below that of the level of residual impurities. Residual impurities are usually donors and result in an n-type wafer with a carrier concentration of about $1 \times 10^{14} \text{ cm}^{-3}$. A bi-layer gate was formed consisting of 400Å of Ti followed by 4000Å of Au thermally deposited through a shadow mask. The gate area is $2.04 \times 10^{-3} \text{ cm}^2$ resulting in devices with an insulator capacitance of about 60 pF.

These were mounted in 12-pin TO-8 headers and measured in dewars cooled by liquid nitrogen. Some samples were also measured using liquid freon 13, (145K) and argon (30K). The dewars are cold shielded so that the background seen by the detector is the same temperature as the detector.

Capacitance and conductance versus voltage were measured at frequencies between 1 MHz and 0.01 Hz (taken as effectively in equilibrium when the applied bias is changing from inversion toward accumulation only). Inversion layer storage time was measured by recording the capacitive transient response to a step change in gate bias with the device in inversion (Zerbst analysis).⁹

High-frequency capacitance (1 MHz) as well as the capacitive transient response were measured using a Sloan Model 410 capacitance meter. This instrument also supplies the voltage sweep used for measurements made at all

other frequencies, including quasistatic. Measurement of capacitance and conductance at these intermediate frequencies were made using a PAR 124 lock-in amplifier, while the quasistatic measurements were made using a PAR model 135 electrometer.

RESULTS

Storage time for ten devices was measured on four wafers cut from four sections of three ingots. These wafers were selected because above average electrical properties of photoconductive and MIS type devices had been fabricated on other wafers from these same sections. The devices reported here were consistent among themselves and with the best MIS devices made on HgCdTe in every property except for their storage times. Flatband bias was between 0 and -0.25V and hysteresis was about 0.2V, as measured at 77K. The midgap minimum value for the density of interface traps (D_{it}), and the average doping level in the depletion region, as measured by C-V analysis, are shown in Table 1. The detailed interface trap structures for these types of devices is presented in Reference 10. Storage time is approximately given by the minority carrier lifetime times the ratio of doping to the intrinsic carrier concentration.⁸ For $x = 0.3$ HgCdTe at 77K the intrinsic carrier concentration is 10^9 cm^{-3} . Thus for these samples reported here a storage time of 1.5 ms (measurement minimum) corresponds to a minority (hole) lifetime of 15 ns.

The data shown here clearly indicates that there is no significant correlation between storage time and either doping density or interface trap density. Since the level of n-type activity seen in these wafers is due to residual impurities incorporated in the ingot during growth, this lack of correlation also suggests that the shortened lifetime is not due to residual impurities. Thus storage time is limited primarily by some other property of the crystal, such as defect density, which is not measured by the techniques of this study.

High-frequency (1 MHz) measurements of an MIS device which has a measurably long storage time (greater than 1.5 ms with our setup) exhibit an effect in inversion referred to as vertical hysteresis.¹¹ This effect is caused by changing the gate bias at a rate that is faster than the rate at which minority carrier generation can effectively maintain equilibrium, but it is slower than the rate at which the more rapid minority carrier recombination can

Table 1. Comparison of Interface Trap Density, Doping Density and Storage Time for the Samples Studied

Part Number*	D_{it} ($eV^{-1}cm^{-2}$)	$N_d - N_a$ (cm^{-3})	Bias Averaged Storage Time
A	1×10^{11}	3×10^{14}	170 ms
B	1×10^{11}	3×10^{14}	112 ms
C	5×10^{11}	9.5×10^{13}	5 sec
D	5×10^{11}	9.5×10^{13}	4 sec
E	5×10^{11}	9.5×10^{13}	2 sec
F	3×10^{11}	1.2×10^{14}	2 ms
G	3×10^{11}	1.2×10^{14}	2 ms
H	3×10^{11}	1.2×10^{14}	3 ms
I	1×10^{11}	3×10^{14}	120 sec
J	3×10^{11}	3×10^{14}	1430 sec
K	2×10^{11}	3×10^{14}	600 sec
L	8×10^{11}	4×10^{14}	27 sec
M	4×10^{11}	4.4×10^{14}	17 sec

*Part Numbers:

- A: ZH-257-4ca can2 pin 4
- B: ZH-257-4ca can2 pin 2
- C: ZH-304-2h canC pin 9
- D: ZH-304-2h canC pin 3
- E: ZH-304-2h canC pin 10
- F: ZH-304-2h canA pin 11
- G: ZH-304-2h canA pin 10
- H: ZH-304-2h canA pin 5
- I: ZH-257-5ca can2B pin 11
- J: ZH-257-5ca can2B pin 2
- K: ZH-257-5ca can2B pin 4
- L: ZH-261-2cd can1 pin 7
- M: ZH-261-2cd can1 pin 6

occur. Thus, as the gate bias is swept toward increasing inversion too rapidly for minority carriers to be generated, they are supplied by a net minority carrier current into the HgCdTe surface. Under these conditions the measured nonequilibrium capacitance in inversion is lower than that which would be recorded under the equilibrium condition of the return sweep. This is illustrated in Figure 1 for four devices, made on a single wafer, which have very long storage times (tens of seconds or greater) compared to that seen routinely on HgCdTe. Capacitance voltage curves were measured using a gate bias ramp rate of 500 mV/s.

As the bias was swept from +2V, where the surface is in accumulation, to -10V, where the surface is strongly inverted, the capacitance follows the nonequilibrium curve of deep depletion (the depletion region is larger than its equilibrium maximum). This is in the range of 10 to 15 pF depending on the specific device. As the gate bias is swept back toward accumulation, the surface inversion layer returns to an equilibrium condition and the capacitance value recorded is that of the inversion layer in parallel with the depletion layer at its maximum width, typically 20 pF.

For some of these devices, the capacitance recorded for the nonequilibrium conditions during the sweep toward increasing inversion is not a constant value. This is particularly pronounced for device number 4, which shows an increase in capacitance between -6 and -9V. At these gate biases minority carriers are being supplied to the depletion layer more rapidly than at neighboring biases.

Contraction of the vertical hysteresis indicates a shorter storage time and therefore minority carrier lifetime. Lifetime can be limited by either surface or bulk traps which are located near midgap and at a distance from the surface where the band bending places the midgap trap at the fermi energy. This condition is met during depletion, for interface traps, but not during inversion and suggests a limit to minority carrier storage time set by traps spatially distributed below the interface. For devices which show this structure in inversion we are depth profiling a nonuniform minority carrier lifetime.

Recorded values of the conductance as a function of gate bias show peaks at the same biases where storage time limiting peaks are seen in capacitance voltage curves. The correlation of these peaks is illustrated in Figure 2.

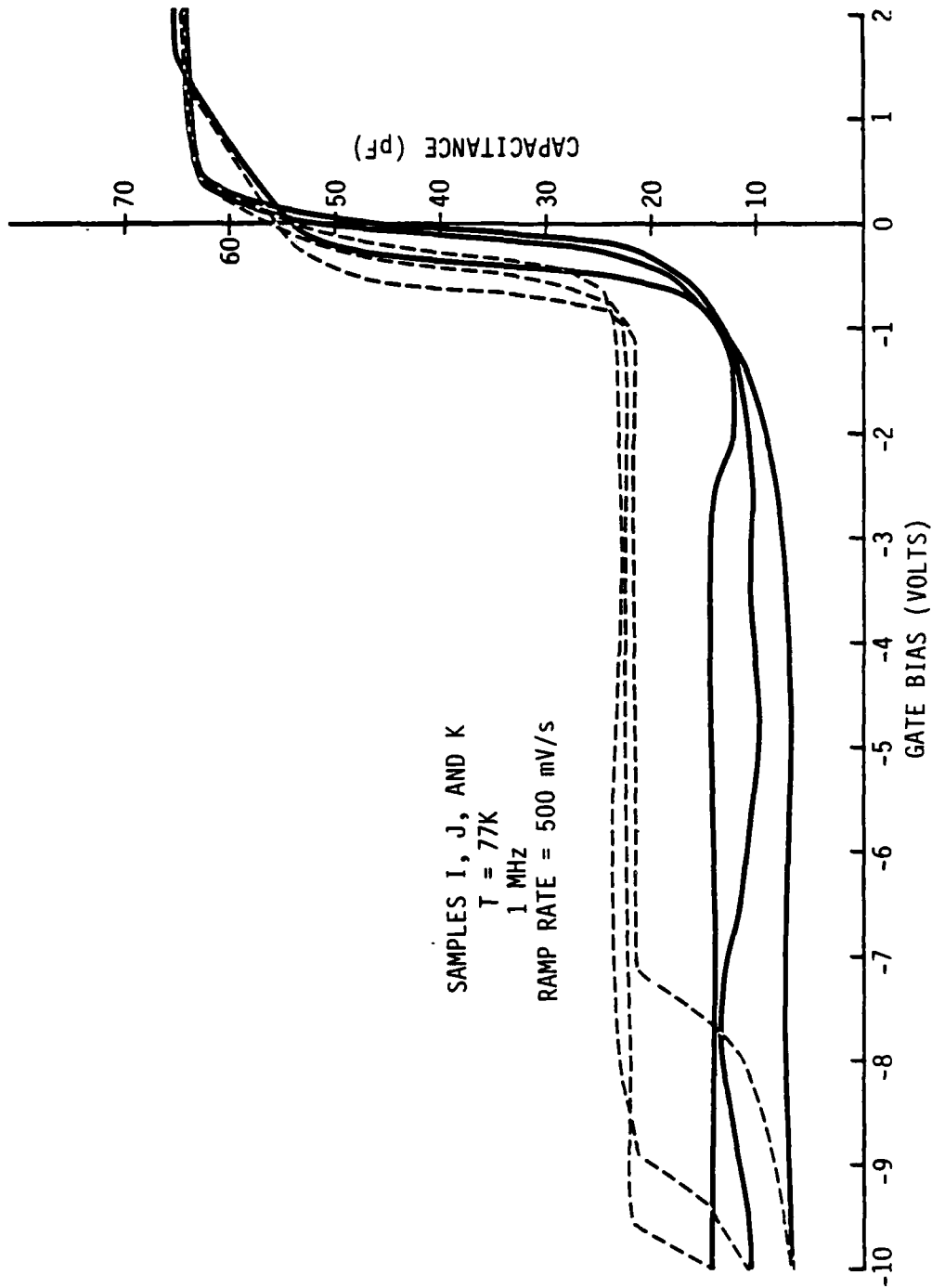


Figure 1. High-frequency Capacitance Voltage Curves for Four MIS Devices on the Same Wafer Showing the Vertical Hysteresis Effect Associated With Long Storage Time

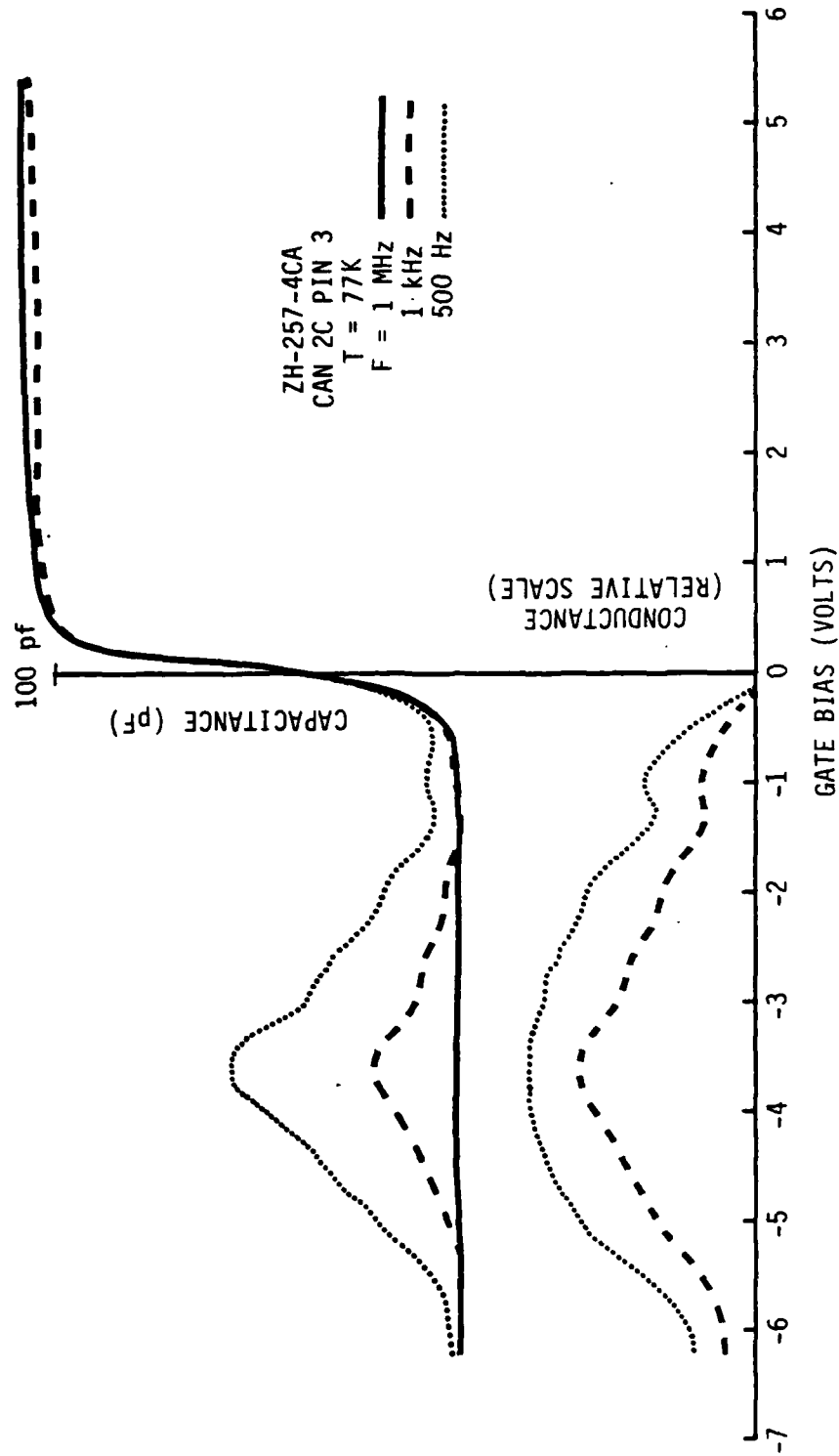


Figure 2. Capacitance Voltage and Conductance Voltage Curves for a Device with a Strong Bias-dependent Storage Time Showing Nearly Identical Bias-dependent Structure

Again, if the g-r centers responsible for limiting the lifetime were interface traps, then the loss peaks observed in conductance curves would be seen at biases where the surface was depleted with the fermi level about midgap at the interface. Since the conductance curves follow the capacitance curves in inversion, this confirms that the g-r site responsible for limiting the storage time is in fact a deep midgap trap located in the bulk of the HgCdTe at a depth where the local midgap point crosses over the fermi energy.

In some of the samples examined, the lifetime is clearly bulk limited but no structure is seen at any bias in inversion because of a very high concentration of uniformly distributed g-r centers. Figure 3 shows capacitance-voltage curves for such a device, taken at several frequencies from 1 MHz to 500 Hz. The measured storage time is less than 1.5 ms (the effective measurement limit of our setup) with no vertical hysteresis seen. Hence, this specific device is not listed in Tables 1 or 2. The form of the curve shows true high frequency behavior at 1 MHz, but begins to respond in inversion at frequencies below 100 KHz. Its crossover frequency, at which the inversion capacitance is halfway between the high frequency and quasistatic values, is seen to be 500 Hz. The minority carrier lifetime in this device is short enough that it is capable of following the bias at frequencies of a few hundred Hz. The transition between high-frequency and quasistatic behavior is monotonic in frequency, as commonly seen for other semiconductors such as Si or GaAs. This transition represents a case of uniformly short bulk-limited lifetime.

Figure 2 shows a capacitance curve for a device with a much longer storage time (300 ms). The curve is recorded at 100 Hz, well below the crossover frequency of the device in Figure 3, which had no measurable storage time. Crossover frequency for the device of Figure 4 is measured at 10 Hz. Except for the region between -1.5 and -3V the curve shows high frequency behavior with no ability of the inversion layer to follow the applied 100 Hz signal. There is, however, a rise at these biases due to minority carrier generation which occurs when the surface region can be expected to be in inversion. For the samples surveyed in this study, this form of bias-dependent storage time with a single peak or two at the beginning of inversion is typical. No structure was seen at all in cases in which the bulk storage time was so short to begin with. In some cases, in which the storage time is long, the structure

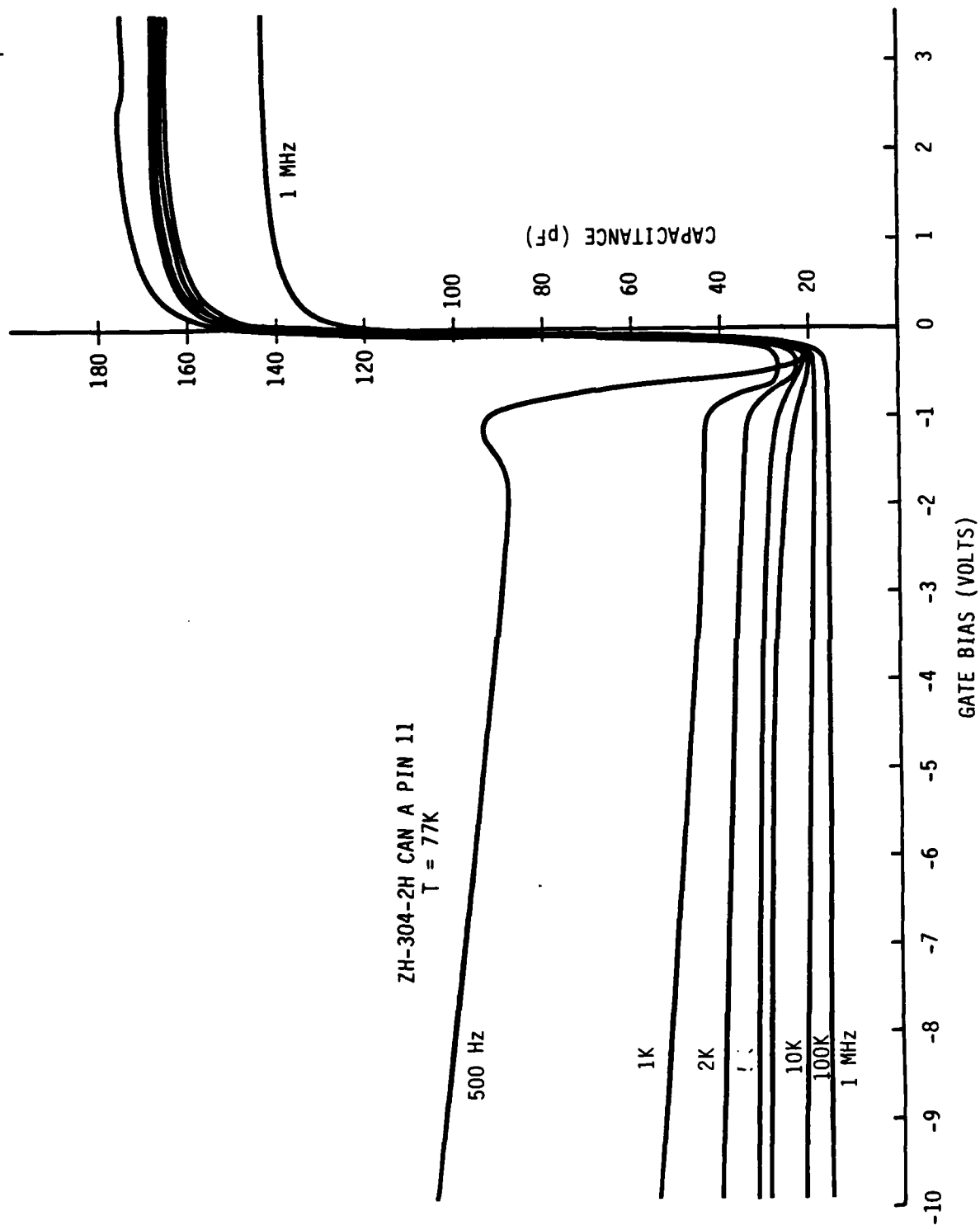


Figure 3. Capacitance Voltage Carrier for an MIS Device with no Measurable Storage Time (<1.5 ms) Showing the Beginning of the Transition from High-frequency Type Behavior to Quasistatic. The Crossover Frequency is 500 Hz.

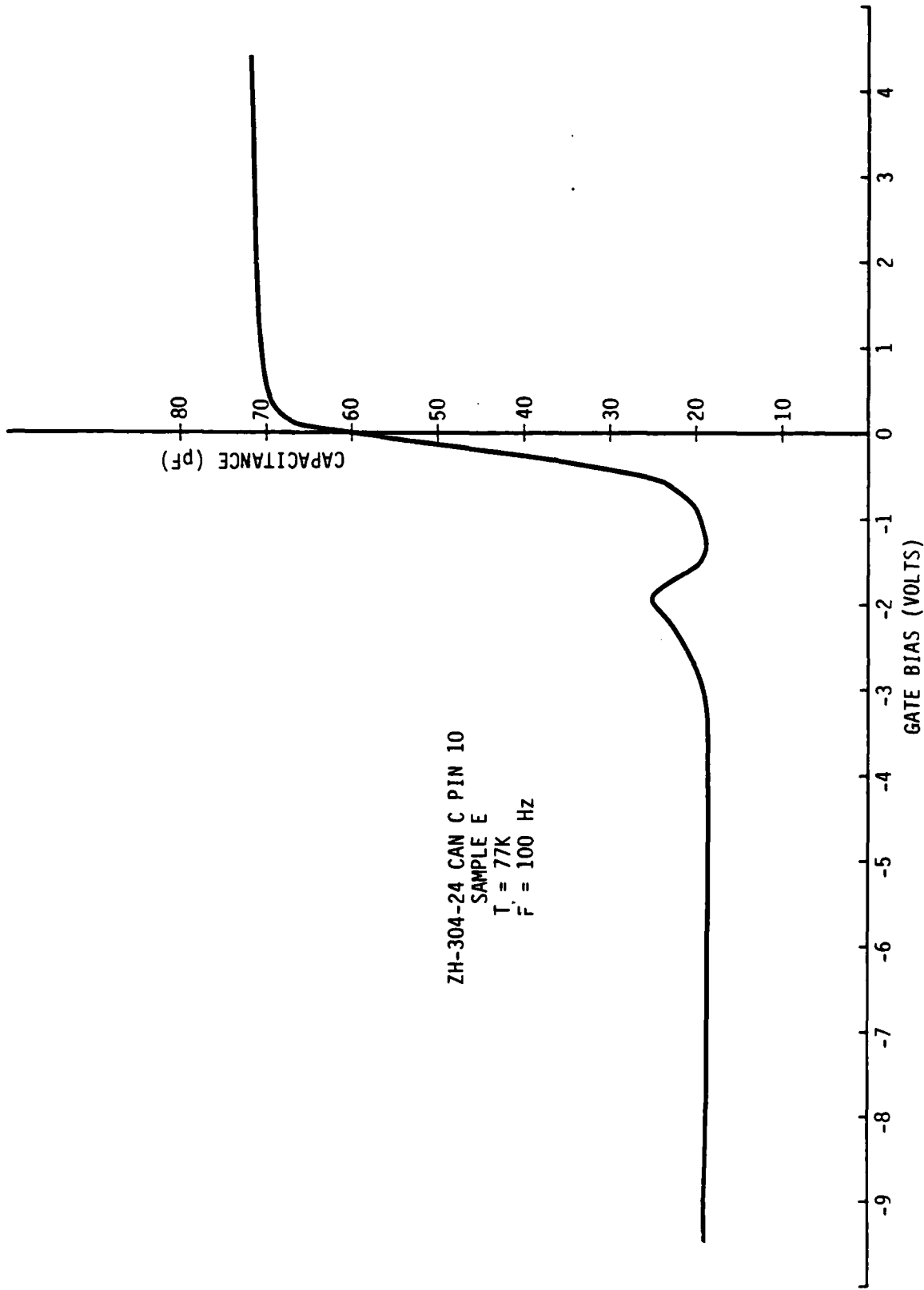


Figure 4. Capacitance Voltage Curve Recorded at 100 Hz for an MIS Device with a 300 ms Storage Time. The Rise at -2V Shows a Locally Shortened Storage Time. Crossover Frequency is 500 Hz.

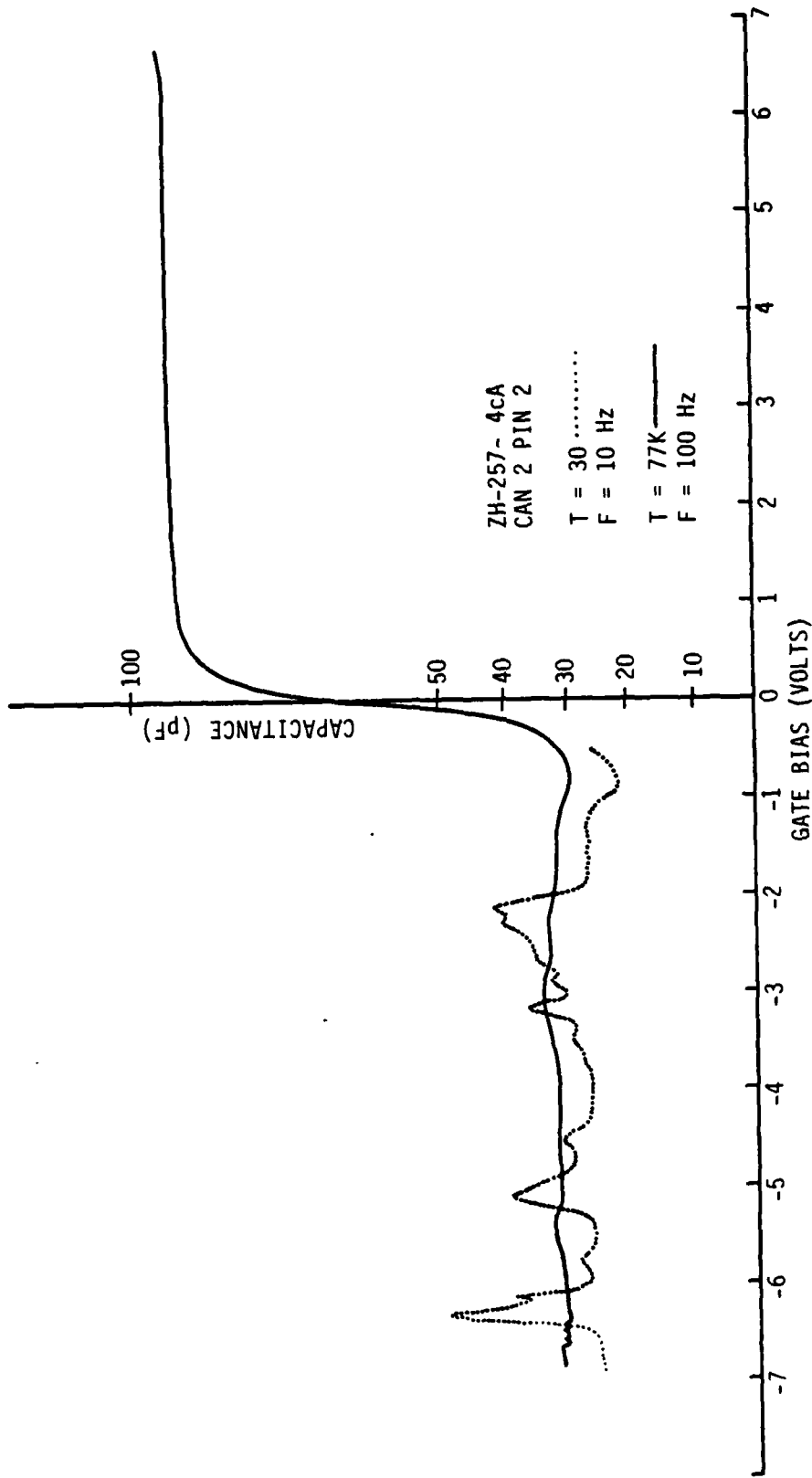


Figure 5. Capacitance Voltage Curves Taken at 100 Hz at 77K and at 10 Hz at 30K for a Device with a Storage Time of About 10 ms at 77K and About 500 μ sec.

is quite detailed, as shown in Figure 5. Figure 5 shows C-V curves of the same device taken at 77 and 30K, at the lowest frequency at which the curve shows predominantly high frequency behavior. Again, at some reverse biases, the inversion layer capacitance is beginning to follow the applied signal, indicating a bias-dependent source of minority carriers. In this case the structure is present from the onset of inversion at -1 to -7V. Several peaks which become quite sharp and reveal a wealth of structure when recorded at 30K are suggested in the 77K curve. The discrete distribution of bulk g-r centers seen in these samples is most likely a very low density of the same centers which uniformly shorten the lifetime everywhere in the sample of Figure 3. The sample of Figure 4 also shows the deepest penetration of discrete sites. The structure ends at about -7V and the inversion layer capacitance is flat and featureless at more negative biases. Crossover frequency of this portion of the C-V curve was well below 1 Hz and not readily measured with our setup.

Quantitative measurement of storage time versus gate bias for Samples A through H are shown in Table 2.

Variations in measured storage times displayed in Table 2 of less than a factor of two are probably not significant for this data and can be taken as essentially equal. The variations of concern are those of an order of magnitude or more. Samples I through M were lost during DLTS measurements after an average storage time was recorded but before detailed bias dependence was recorded. Examination of the behavior of the vertical hysteresis seen in these samples as shown in Figure 1, for I, J and K and in Figure 6 for L and M indicates a behavior consistent with the other samples reported in Table 2.

Table 2. Storage Time as a Function of Reverse Gate Bias
for Samples A Through H

Bias Interval	Sample							
	A ms	B ms	C sec	D sec	E sec	F ms	G ms	H ms
0,-1	256	244	0.6	0.4	0.5	3	3	8
-1,-2	7.8	14	0.4	0.6	0.04	4	4	25
-2,-3	5.3	5	5	4	4	2	2	3
-3,-4	5.3	3						
-4,-5	22	14	5	4	2	2	2	2
-5,-6	360							
-6,-7	450	11	5	4	2	2	2	2
-7,-8	300							
-8,-9	128	218	not measured			2	2	2
-9,-10	125							
-10,-11	125	300	not measured -----					
-11,-12	100							

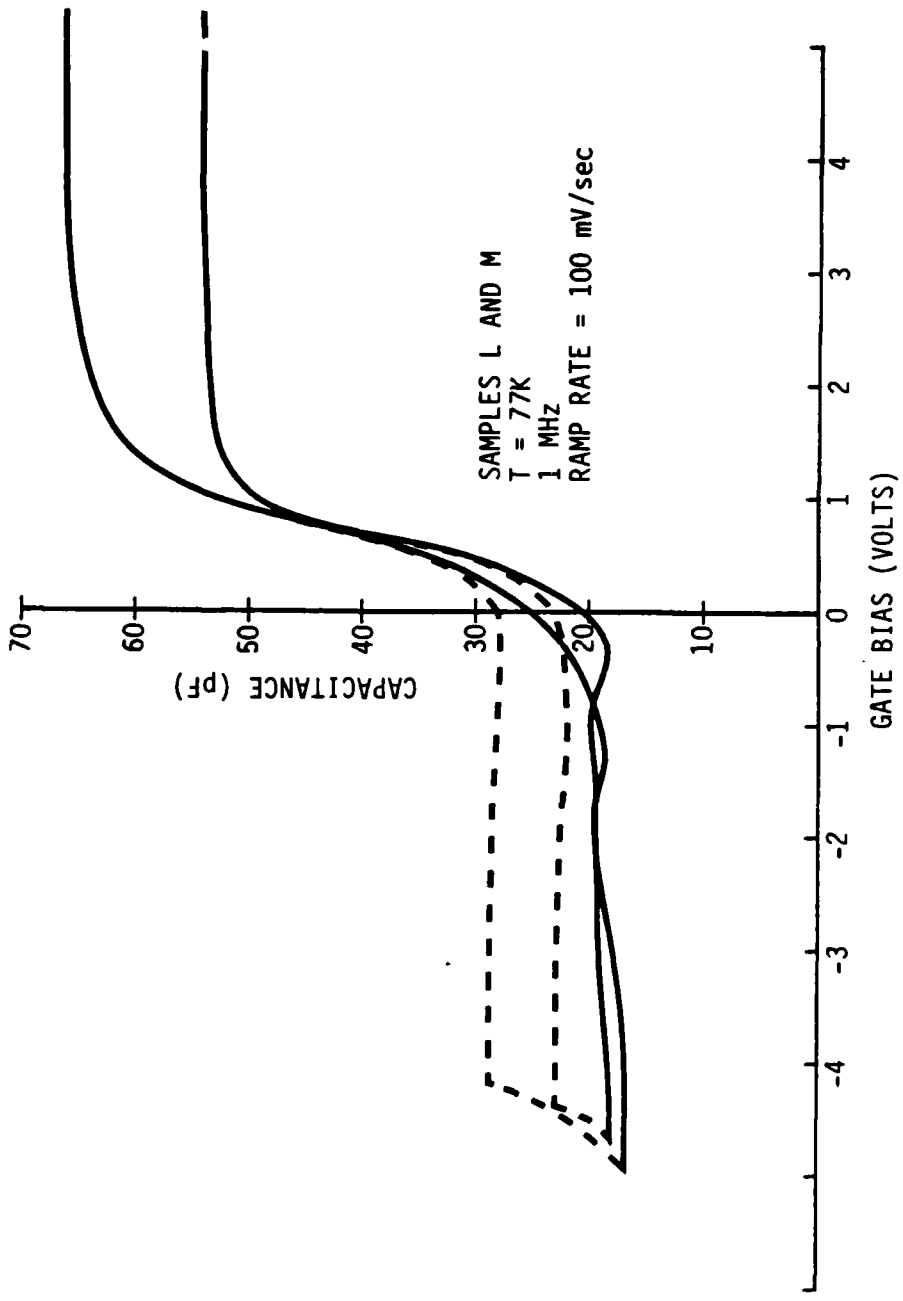


Figure 6. High Frequency C-V Curves for Samples L and M Showing Bias-Dependent Vertical Hysteresis in Inversion.

CONCLUSION

Storage times measured for these bulk-grown wafers ranged from a few milliseconds up to 10^3 sec. We have found no evidence of MIS storage time, and therefore, minority carrier lifetime, limited by interface traps. In the longer storage time wafers a dependence of measured storage time on gate bias in inversion was seen, indicating that in these samples, storage time is non-uniformly distributed in depth below the interface. This distribution is due to nonuniformly distributed midgap traps acting as effective g-r centers. These g-r centers vary either their population or their effectiveness as lifetime limiters with depth. This latter variation can occur due to local changes in band structure which cause a certain trap to be closer to midgap at some depths than at others. Either population or effectiveness variations can occur as a result of damage to the HgCdTe lattice. Though the depths probed here are limited to no more than 2 μm , the occurrence of these centers does appear to be biased toward the interface, suggesting very deep damage due to surface processing as a cause.

The samples presented here are cases in which a strong bias dependence to the storage time is seen. There are also cases in which samples exhibit weak or no measurable bias dependence. In the samples surveyed the incidence of bias dependent storage time was greater than half. Lack of structure is taken to indicate uniformly bulk-limited lifetimes. Presence of structure may indicate an additional source of lifetime-limiting defects.

Cases in which the storage time varies strongly with depth are cases in which the average storage times are intermediate between immeasurably short values (less than 1.5 ms) and the very long times of 10^2 to 10^3 sec occasionally seen. This intermediate case corresponds to the situation in which the g-r centers that dominate in short lifetime samples are at a low enough concentration to act as locally discrete regions, while at lower concentrations, are nearly absent.

ACKNOWLEDGEMENTS

We gratefully acknowledge the technical assistance of J.F. Santarosa and M.E. Boyd in recording the capacitance data, and to T.N. Casselman, A. Sher and D.R. Rhiger for many helpful discussions. This work was sponsored by DARPA under contract number MDA-903-83-C-0108. The sponsor is R.A. Reynolds and the technical monitor is J. Murphy of DARPA/DSO.

List of References

1. E.H. Nicollian and J.R. Brews, MOS Physics and Technology (John Wiley & Sons, New York, 1982) p. 110
2. A. Sher, A.B. Chen, W.E. Spicer and C.K. Shih J. Vac. Sci. Technol. A3 (1), 105 (1985)
3. G.P. Carey, C.S. Stahle, J.A. Silberman, W.E. Spicer, J.A. Wilson and V.A. Cotton submitted to Appl. Phys. Lett.
4. D.R. Rhiger and R.E. Kvaas, J. Vac. Sci. Technol. 21 (1), 168, (1982)
5. J.A. Wilson and V.A. Cotton, J. Vac Sci. Technol. A-1 (3), 1719 (1983)
6. P.M. Raccah, V. Lee, J.A. Silberman, W.E. Spicer and J.A. Wilson Appl. Phys. Lett. 42 (4), 374 (1983)
7. P.M. Raccah, J.W. Garland, Z. Zhang, V. Lee, DA Zhong Xue, L.L. Abels, S. Ugur and W. Wilinsky, Phy. Rev. Lett. 53, 20, 1958 (1984)
8. E.H. Nicollian p. 139
9. M. Zerbst, Z. Angew. Phys., 22, 30 (1966)
10. G.H. Tsau, A Sher, M. Madou, J.A. Wilson, V.A. Cotton, and C.E. Jones To be Published in J. Appl. Phys.
11. E.H. Nicollian and J.R. Brews p. 170

Section II
 CHANNELED IMPLANTS

CARRIER TRAPPING CENTERS IN RANDOMLY IMPLANTED HgCdTe

V.A. Cotton and J.A. Wilson

Santa Barbara Research Center
 75 Coromar Drive
 Goleta, CA 93117

ABSTRACT

Trap levels associated with random (nonchanneled) ion implantation in $\text{Hg}_{1-x}\text{Cd}_x\text{Te}$ ($x \approx 0.3$) have been characterized for the first time using deep level transient spectroscopy (DLTS), secondary ion mass spectroscopy (SIMS), and high frequency (1 MHz) capacitance voltage (C-V) techniques. A deep level trap with an activation energy (E_t) of 0.20 eV and capture cross section (σ_n) of $9.2 \times 10^{-20} \text{ cm}^{-2}$ has been seen in samples implanted with 200 keV chlorine. The trap concentration with depth, from DLTS profiling, scales linearly with ion concentration as measured by SIMS. The resulting donor concentration measured by C-V is increased over the ion concentration by a factor of about 100. Another state is seen at 0.053 eV, which is thought to be associated with interface traps. These results indicate that separate mechanisms producing the deep trap level and the donor activity are caused by lattice distortion and atomic displacement due to the implant process.

INTRODUCTION

Ion implantation is a commonly used method for forming p-n junctions in a variety of semiconductors and is particularly successful in Si. In $\text{Hg}_{1-x}\text{Cd}_x\text{Te}$ the damage associated with this process is known to create high levels of n-type electrical activity¹ which completely dominate any activity due to the ion species. Detailed investigation of the trapping levels which result from this damage has not received significant attention in spite of the widespread use of this process.

In this work the deep states which result from implantation of chlorine into $\text{Hg}_{0.7}\text{Cd}_{0.3}\text{Te}$ are investigated. The final atomic profile for the doses and energies used was obtained using SIMS. Doping and deep-trap profiles were measured in metal-insulator-semiconductor (MIS) devices using C-V and DLTS. These devices were made using Photox[™] SiO_2 as the dielectric and a bilayer of Au on Ti as the gate. Two prominent trapping levels were found and characterized providing activation energy, capture cross section, and depth distribution information. Quantitative comparisons were made between trap concentration, donor concentration and implant species profile.

SAMPLE PREPARATION

Wafers of $\text{Hg}_{0.7}\text{Cd}_{0.3}\text{Te}$ were cut from ingots grown by the horizontal zone melt technique. Slices are cut parallel to the long axis of the boule resulting in wafers of random orientation. Doping densities, due to background impurities, of $N_D = 3 \times 10^{15} \text{ cm}^{-3}$ were obtained by isothermal annealing in Hg vapor. Samples were then polished to a smooth finish using a chemomechanical polish. Chlorine was implanted at 200 keV to a dose of $5 \times 10^{11} \text{ cm}^{-2}$. Since the material is unoriented, this results in a random implant thought to be dominated by nuclear stopping.² To date, no successful postimplant anneal has been developed for this material, though many different technologies have been evaluated. The electrical activity due to damage and due to any activated chlorine (which would be n-type by occupation of a Te site) are not easily separated. Each implanted wafer was divided into several sections, each of which was etched to a separate depth prior to fabrication of the MIS device. This step etch was done using Br_2 in ethylene glycol (Br/EG) with photoresist protecting already-etched sections. The depths used were chosen to bracket the peak ion concentration as measured by SIMS on a separate wafer. In cases where nonidentical doses were used, SIMS profile concentrations were assumed to scale linearly with dose. C-V measurement of the average doping density at 77K in the depletion region for these devices provided quantitative doping profiles.

DLTS was then used on the same device to measure activation energies, capture cross sections, and variation of trap concentration with depth. The DLTS uses an ac signal of 10 MHz superimposed on a square wave bias pulse which alternately fills and empties traps, resulting in an emission rate, e ,

give by $e = 1/\tau$ where $\tau = (t_1 - t_2)/\ln(t_1 - t_2)$, in which t_1 and t_2 are the time points at which the capacitance transient is sampled following the end of the fill pulse. Arrhenius plots of $1000/T$ versus e have a slope which is then the activation energy, E_A .³ Selecting measurement parameters which reveal the trap of interest and gradually shortening the fill pulse time results in fewer traps responding at a rate dependent upon the capture cross section. Thus, examination of the dependence of trap fill time on signal amplitude allows us to determine a value for the capture cross section.⁴

RESULTS

SIMS profiles showed the expected Gaussian dependence of the atomic profile with depth as predicted by LSS theory.⁵ These calculations have been performed for various elements implanted into CdTe⁶ and can be approximately scaled for HgCdTe by assuming a binary system of ATe where the mass of A is the average of Hg and Cd.

C-V measurements show an increased donor level, N_D , which follows the atomic profile but with a concentration a factor of 100 higher. Comparison of C-V and SIMS results are shown in Figure 1. Quasi-static C-V measurements were unobtainable however, since the resultant signal showed significant drift and made data acquisition impossible due to the exceptionally high density of interface traps in implanted HgCdTe.

Two peaks are seen in the DLTS spectra shown in Figure 2. The most prominent peak in the 200K range showed very little shift with temperature indicating an unusually high activation energy of $E_{DLTS} = 2.76$ eV. This value represents the combined effects of trap activation energy, E_t , and barrier effects measured as a capture cross section activation energy, E_σ . Separation of these values gave a true trap activation energy of $E_t = 0.20 \pm 0.03$ eV ($E_g = 0.27$ eV at 200K), a barrier potential of $E_\sigma = 2.56$ eV and a capture cross section $\sigma_n = 9.2 \times 10^{-20}$ cm². Since the MIS capacitor as the measurement device in these experiments is a majority carrier device only majority carrier traps, electrons in this case, are detected. The uncertainty in E_t is due to the required subtraction of two large numbers to yield this small one as well as the resolution limit of the small peak shifts seen as the temperature is changed. The capture cross section value indicates a weakly repulsive trap. Measurement of trap concentration on the same devices as those for which N_D

was determined, show that the trap is directly proportional to doping density, with a scale factor of 20 as indicated in Figure 3. The trap concentration then also scales linearly with implant species with a scale factor of 5 as shown in Figure 1.

The second peak seen in this spectral represents a state with $E_t = 0.053 \pm 0.01$ eV and $\sigma_n = 2 \times 10^{-18}$ cm². This is quite similar to the low concentration state seen in unimplanted material⁷ by Cotton et al, with $E_t = 0.079$ eV and $\sigma_n = 1.2 \times 10^{-18}$ cm² but is higher in concentration. Neither of the prominent bulk traps seen in unimplanted n-type HgCdTe at 0.12 eV and 0.172 eV were seen in this material.

CONCLUSIONS

These results combine to give an emerging picture of the implanted HgCdTe surface region. Implant damage related traps at 0.20 and 0.053 eV appear to be replacing native defect-type traps. The dominant majority trap at 0.20 eV is near midgap and is thus likely to have a serious impact on limiting minority carrier lifetime and hence adversely affect operation of devices made in this manner. Also, the large barrier to electron capture will be attractive to holes, limiting minority carrier lifetime. The similarity of the 0.053 eV trap found here and the 0.079 eV trap in unimplanted material as well as the increase in concentration in the implanted case indicate that this may be a measure of interface trap density in this region increasing surface leakage currents. This is partially substantiated by the drift seen in quasistatic measurements.

There are two important correlations in this data: (1) the 0.20 eV trap concentration scales linearly with implant species concentration with a scale factor of 5 and (2) donor concentration also scales linearly with implant species but with a level 100 times higher. This infers that the trap level is due to a mechanism that corresponds with the implant damage, but one which is as yet unidentified while increased donor activity is created by lattice distortion due to propagated energy loss as the ion is slowed down in the crystal.

REFERENCES

1. J. Baars, A. Hurrie, W. Rothemund, C.R. Fritzsche, and T. Jakobus, J. Appl. Phys., 53(3), March 1982, p 1461
2. T.W. Sigmon, Interim Report No. 1, Contract No. 945190-B5
3. D.V. Lang, Journal of Applied Physics, Vol. 45, No. 7, 1974, p 3023
4. D.L. Polla and C.E. Jones, J. Appl. Phys., Vol. 52, No. 8, August 1981, p 5126
5. J. Lindhard and M. Scharff, Phys. Rev., Vol. 124, No. 1, 128 (1961)
6. J.F. Gibbons, W.S. Johnson, S.W. Mylroia, Projected Range Statistics, Halsted Press, 1975
7. V.A. Cotton, J.A. Wilson, and C.E. Jones, to be published, J. of Appl. Phys., August 1985

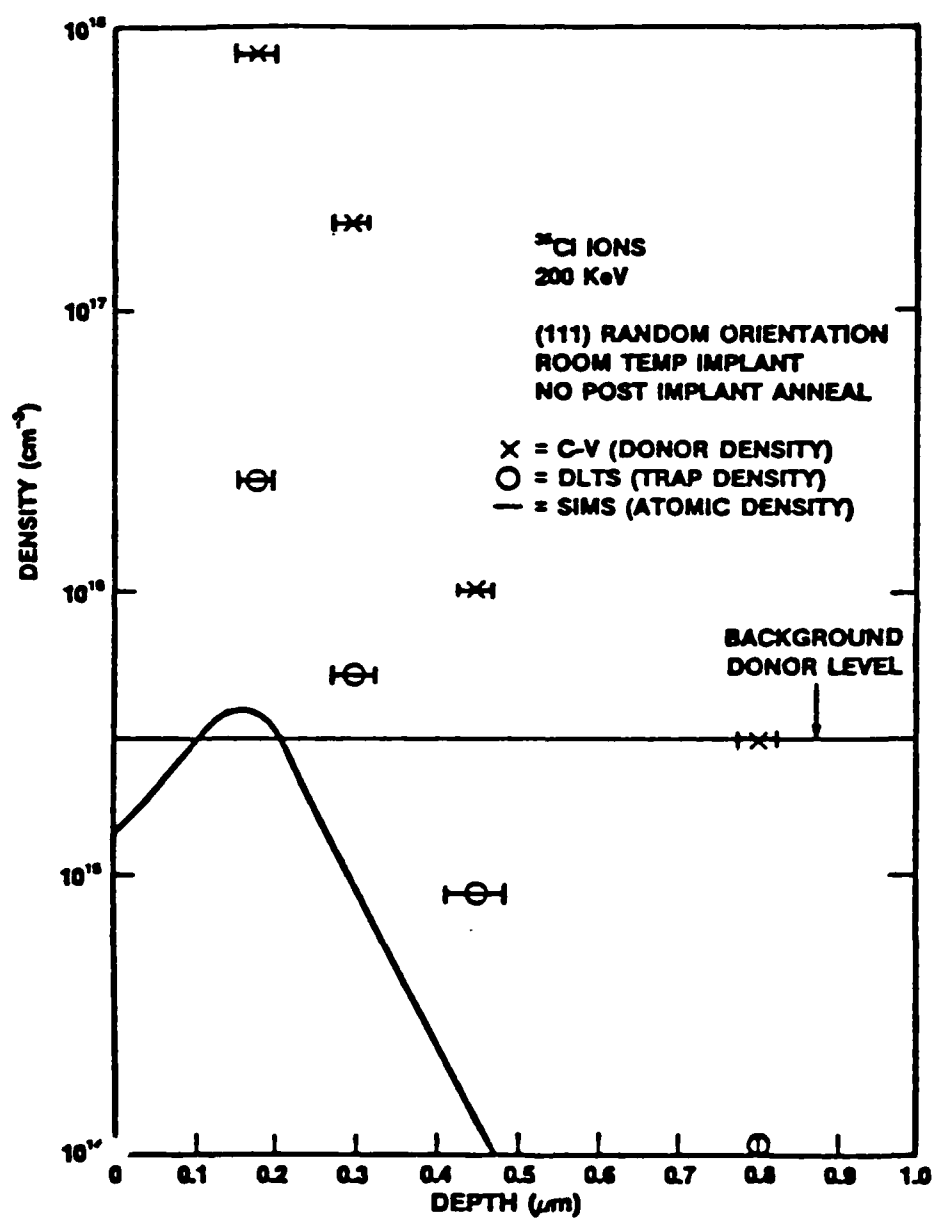


Figure 1. Comparison of Donor Activity (C-V) and Atomic Profile (SIMS)

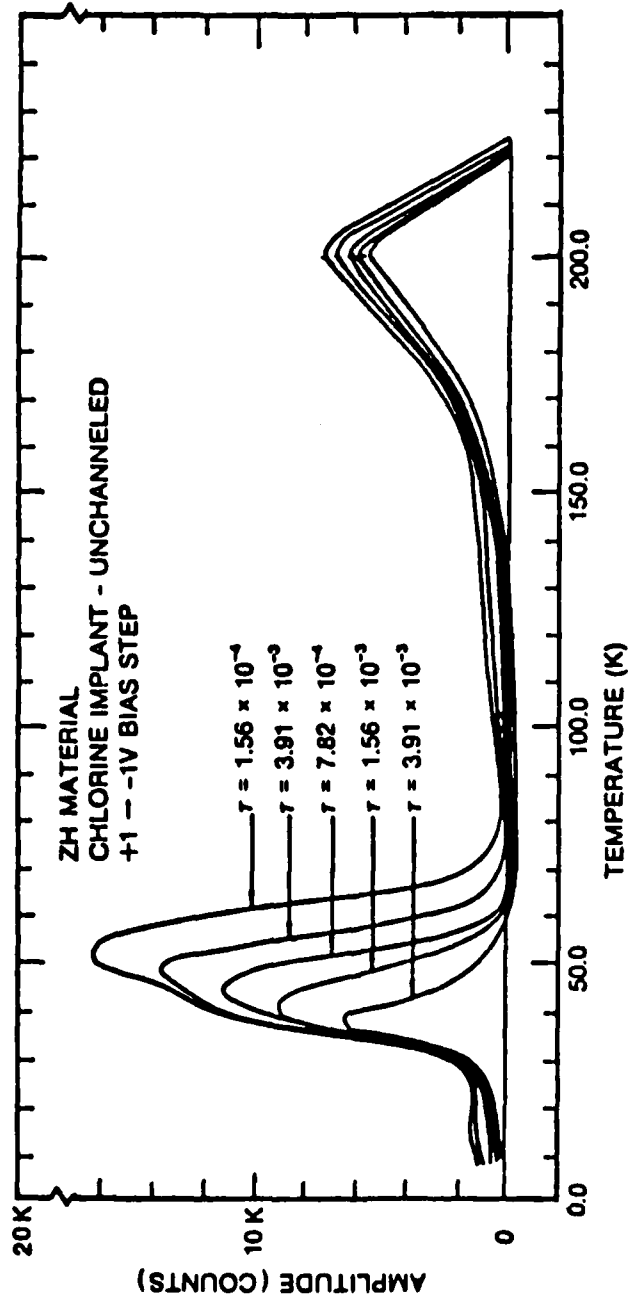


Figure 2. DLTS Spectra for Chlorine-Implanted HgCdTe MIS Device

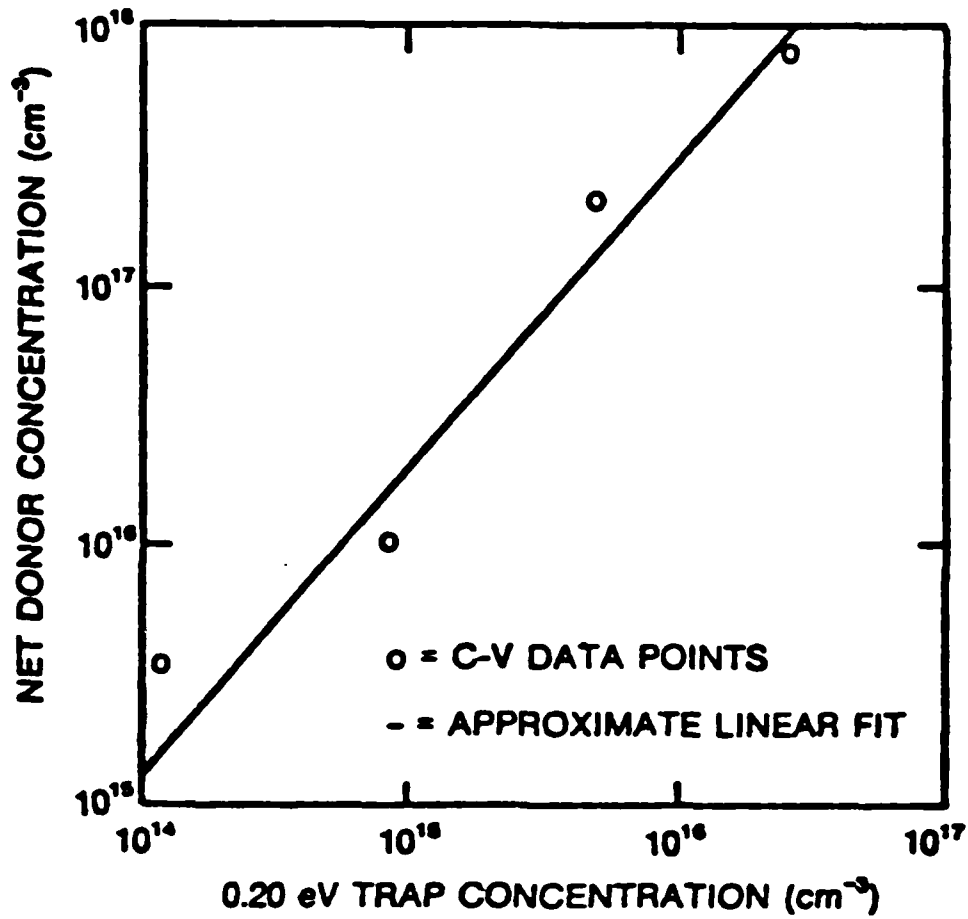


Figure 3. Concentration of the 0.20 eV Trap in Chlorine-Implanted Samples Follows Nearly Linearly the Change in Donor Concentration due to Implant Damage. Trap Concentration From DLTS, Doping Density from 1 MHz C-V.

Section III SURFACE STUDY

INTRODUCTION

The thermodynamic kinetic complexity of the $\text{Hg}_{1-x}\text{Cd}_x\text{Te}$ alloy is manifested in several aspects of materials growth, processing, and passivation. How these procedures affect the electronic structure of this II-VI semiconductor system is of extreme fundamental as well as practical importance. The successful manufacture of HgCdTe devices relies on the critical understanding of many of the subtle interactions that occur within HgCdTe upon the growth of epitaxial interfaces, the deposition of thin passivating or metal films, and the etching chemistry during surface preparation. In particular, the production of electrically active point or line defects and the altered stoichiometry and atomic structure of the alloy resulting from these procedures are of extreme interest.

The initial stages of native oxide formation on atomically clean HgCdTe gives insight into the kinetic barriers that occur at the native oxide/HgCdTe interface. Section II presents new information in our continuing study of this process. It is shown that the reaction occurring at the surface is not directly photon assisted. In order to extend these oxidation studies from our cleaved or "model" surfaces to those surfaces of practical importance that have undergone some surface preparation, one must first characterize these etched and cleaned surfaces. The initial characterization of these technologically important interfaces using photoemission spectroscopy (PES) is presented in Section III of this report.

The preferential removal of the metal atom Hg from the alloy is achieved by irradiating the surface with an electron beam. The ability to control the electron beam parameters precisely allows one to surgically remove Hg from the lattice. Section IV presents our initial work at characterizing the surface after well controlled removal of Hg.

Metal contacts are also of extreme importance for HgCdTe devices. Employing thermodynamic guidelines, we picked Ag as a nonreactive candidate metal and Al as a reactive candidate metal. An initial study of the reaction chemistry between these metals and HgCdTe at the interface is described in Section V.

(This page left intentionally blank)

Investigations into the nature of excited oxygen

J.A.Silberman

Introduction

Our earliest work on the interaction of atomically clean cleaved surfaces of $\text{Hg}_{1-x}\text{Cd}_x\text{Te}$ with molecular oxygen in the gas phase demonstrated the low reactivity of this system at room temperature: exposure to 1 atmosphere of O_2 for 16 hours resulted in no detectible oxygen on the surface,¹ limiting the initial sticking coefficient to less than 10^{-13} . Such a low sticking coefficient for molecular oxygen is also observed on CdTe and other II-VI compounds² and reflects the trend of reduced reactivity with increasing polarity of the semiconductor bond.^{3,4} As has been observed in the oxidation of GaAs,⁵ the uptake can be greatly stimulated by operating an ion gauge in the oxygen ambient during the exposure. In the case of $\text{Hg}_{1-x}\text{Cd}_x\text{Te}$, activation of the oxidation process by an operating ion gauge or even a hot filament in direct line-of-sight with the sample increases the sticking coefficient by at least 9 orders of magnitude. The question of what the mechanism behind the dramatic stimulation in uptake might be is immediately raised. Whether the activation is due to generation of ionic or excited neutral species, catalytic generation at the filament surface of oxygen containing molecules such as H_2O or CO_2 from O_2 and components of the background gas, or merely an effect of the radiation produce by the incandescent filament are hypotheses which must be explored. These questions, in addition to being of intrinsic interest, are relevant to passivation interfaces because the interaction of the clean surface with activated oxygen may prove to be a model for oxidation by atomic oxygen (such as may occur in the photox reactor) or the air oxidation of the surface, which presumably is promoted by water vapor or CO or other oxygen bearing molecules. This information is also of importance in completing the description begun in work studying the effects of activated oxygen exposure on HgCdTe surfaces.^{6,7}

Work to date

The experimental data presented here indicates that it is a flux of particles rather than photons which is responsible for the enhanced uptake due to the hot filament. Work prior to this established that these particles are highly excited and neutral rather than charged.

The degree of excitation of the oxidizing particles is indirectly revealed by the observation that the uptake of oxygen is enhanced only so long as the filament is in direct line-of-sight of the sample surface⁸; an experimental geometry in which a particle's path must be deflected by striking the stainless steel walls of the vacuum vessel in order for the atom or molecule to travel from the filament to the sample surface results in apparently complete deexcitation of the species and no discernible uptake. The ease with which the excitation is quenched by collision (or recombination or reaction at the wall) and the concomitant requirement of line-of-sight exposure indicates a high degree of excitation and sets apart the process active in the stimulated oxidation of $\text{Hg}_{1-x}\text{Cd}_x\text{Te}$ from that observed on GaAs,⁵ where metastable singlet molecular oxygen, which is active even when produced by a gauge out of line-of sight of the sample, is proposed to be the activated species. It should be noted that singlet oxygen can exist in a very long lived metastable state having an excitation energy of about 1 eV or in a shorter lived (but perhaps sufficiently long for the present experiments) more excited state with about 1.6 eV excitation energy. It may be only the latter state which has sufficient energy to overcome the activation barrier in the present work.

To establish that a neutral particle rather than an ion is involved in the activated uptake, the oxidation of the surface was measured with the sample biased either positive or negative with respect to the filament. Using ultraviolet photoemission spectroscopy to monitor the O 2p emission produced in the valence band region by adsorbed oxygen as well as x-ray photoemission spectroscopy to characterize the extent of oxidation as revealed by the distinct signatures of oxidized and unoxidized Te, no dependence of the uptake on sample bias was observed.

A neutral excited species rules out ions and electrons, but doesn't preclude the possibility that the uptake is stimulated by thermal or electronic effects due to the absorption of the radiation from the hot filament. The experiment described below was designed to examine this possibility.

Experimental

A cleaved (110) surface of $\text{Hg}_{0.8}\text{Cd}_{0.2}\text{Te}$ was exposed to oxygen (10^{-4} Torr for 1000 sec) with the surface in line-of-sight of a hot filament in two different configurations: either with a LiF window separating the volume containing the filament from that in which the sample sat (both volumes contained oxygen and were, in fact, connected by a pipe allowing non-line-of-sight transport of species from the filament to the sample and equalizing the pressure in the two volumes), or the direct path between sample and

exciting filament was free of the LiF window. The sample-filament distance was maintained constant in each case to eliminate the natural attenuation of particle flux with distance from the excitation source. With the window in place, the radiation from the filament was transmitted and incident on the sample, but activated particles were blocked; with the window removed, both photons and particles were allowed a direct path to the surface. The cleaved surface was exposed twice with the window in place, then twice more to equal doses with the window removed.

The LiF window is transparent in the visible and ultraviolet up to approximately 11.8 eV. Because the absorption edge of the $x=0.2$ sample lies near $7.5 \mu\text{m}$ at room temperature, infrared emission from the filament may also be absorbed, contributing to heating as well as electron-hole pair formation. The IR transmission of the window used, shown in Figure 1, was measured by SBRC to be greater than 50% above $8 \mu\text{m}$, reaching roughly 90% at $5.5 \mu\text{m}$. Thus little of the spectrum which might excite the HgCdTe or even the oxygen molecules is blocked by the window used.

Photoemission spectroscopy using a He discharge (21.2 and 40.8 eV) or Mg anode (1253.6 eV) was used to characterize the clean surface and monitor the effects of oxygen exposure.

Results and discussion

Spectra of the clean surface, the surface exposed with the direct path for activated oxygen blocked by the window, and the surface subsequently exposed to oxygen with the window removed so as to permit straight line travel to the surface for oxygen excited by the filament are compared in Figure 2. This data was recorded for $h\nu = 40.8 \text{ eV}$ but shows emission from 38 to 42 eV in kinetic energy due to a small component of 48.4 eV light (He III). Emission from O 2p derived states in the valence band is visible at 37 eV in only the two spectra recorded following exposure to oxygen *without* the LiF window; the spectra for the surface exposed to the radiation from the filament by no line-of-sight oxygen are indistinguishable from that of the clean surface curve in this region.

The result that no oxidation occurs when the radiation and oxygen ambient are present but the line-of-sight path for excited atoms or molecules is removed demonstrates that an excited species rather than thermal or photoexcited effects is responsible for the activated uptake. Based on our previous work this particle must also be neutral.

Yet another possible explanation for the activated species is the possibility that the high temperature filament catalyzes reactions between O_2 and molecules in the

background gas to generate excited molecules of oxygen containing species such as CO_2 or H_2O . These synthesized molecules would have to gain activity due to excitation since the sample would not be expected to show such a strong dependence on the line-of-sight nature of the exposure. An experiment to probe this possibility by the application of mass spectroscopy to the flux of particles leaving the filament is planned for future work.

References

1. P. Morgen, J.A. Silberman, I. Lindau, W.E. Spicer, and J.A. Wilson, *J. Elect. Mater.* 11, 597 (1982).
2. Atsuko Ebina, Kiyomitsu Asano, and Tadashi Takahashi, *Phys. Rev. B* 22, 1980 (1980).
3. Peter Mark and William F. Creighton, *Appl. Phys. Lett.* 27, 400 (1975).
4. R.S. Bauer, *J. Vac. Sci. Technol.* 14, 899 (1977).
5. P. Pianetta, I. Lindau, C.M. Garner, and W.E. Spicer, *Phys. Rev. B* 18, 2792 (1978).
6. J.A. Silberman, D. Laser, I. Lindau, W.E. Spicer, and J.A. Wilson, *J. Vac. Sci. Technol. A* 1, 1706 (1983).
7. J.A. Silberman, D. Laser, I. Lindau, W.E. Spicer, and J.A. Wilson, *J. Vac. Sci. Technol. A* 3, 222 (1985).
8. HgCdTe Surface Study Program Semiannual Technical Report, March 1, 1982.

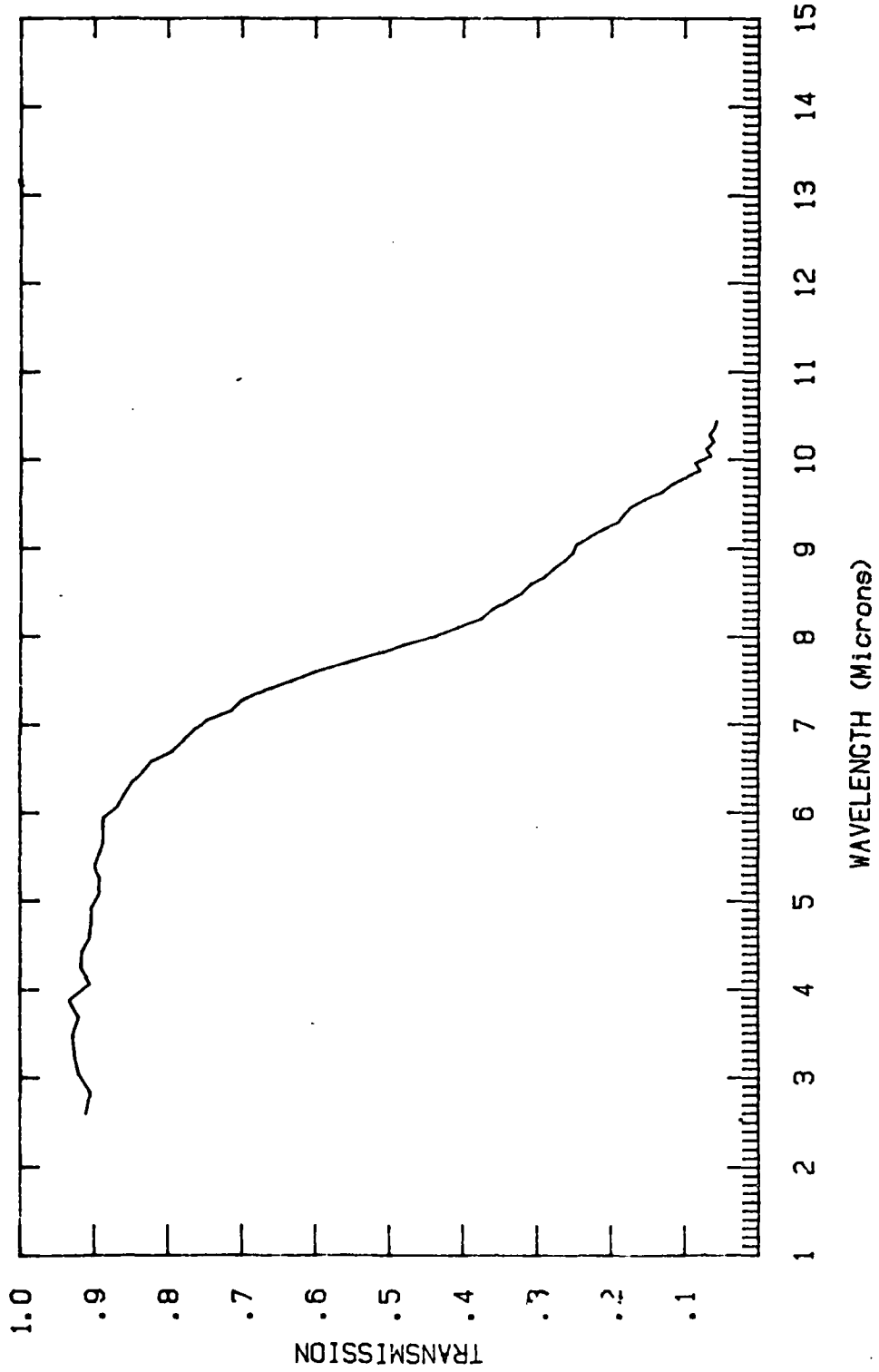
Figure captions

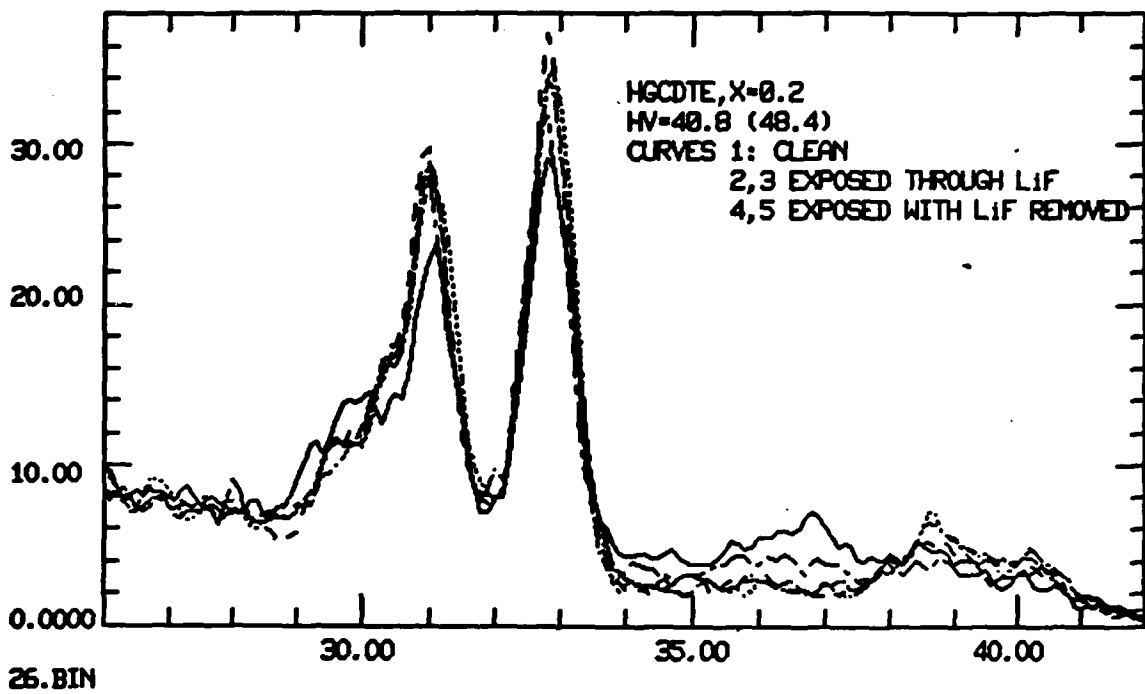
1. Infrared transmission of LiF window used in investigation of photon induced effects in the activated oxidation of HgCdTe. Measurements performed at SBRC.
2. Comparison of valence band spectra from the clean surface, the surface exposed twice to oxygen with a LiF window blocking the direct path to the surface of molecules excited at the filament but passing radiation, and of the same surface subsequently exposed twice to oxygen where a line-of-sight path for the particles existed.

Stanford Filter

TEMP: 300 K SLIT: 0.5 mm

12/5/64





(This page left intentionally blank)

Photoemission Studies of Technologically Important Surfaces of HgCdTe

Glen P. Carey, Carl S. Stahle, and Joel A. Silberman

I. INTRODUCTION

One of the major applications of HgCdTe today is to build metal-insulating-semiconductor electronic device structures which are used to construct charge coupled devices (CCD) which are then integrated into focal plane arrays for IR imaging systems. One of the key problems in the fabrication of these HgCdTe electronic devices is that of surface passivation¹. Passivation is needed to reduce surface leakage currents and to maintain electrical and chemical stability. The difficulty in passivating HgCdTe is related to the activity of the surface which leads to an important HgCdTe modification at the surface and interaction between the passivant and HgCdTe. Work by Silberman et. al.² in this group has focused on the interaction between activated oxygen and HgCdTe. These studies are performed in a UHV environment on atomically clean surfaces, hence the reaction chemistry of the surface can be monitored in a well controlled way. This model surface provides information into the baseline thermodynamic and reaction kinetics occurring at the surface. These studies can then be extended to surfaces cleaned by chemical procedures. But, the nature of these technologically important surfaces must be well understood before a full understanding of the passivant/ HgCdTe reaction chemistry can be obtained.

The surface activity which leads to difficulty in passivating HgCdTe also causes this alloy to be very sensitive to chemical and physical treatments. Various surface treatments on HgCdTe and experiments to analyze the effects of those surface treatments have been performed in the recent past. All of the experiments have demonstrated that the surface stoichiometry may be altered. With surface preparation

techniques that involve etching with solvent diluted Bromine etchants, Aspnes et. al. (spectroscopic ellipsometry)³, A. Lastras-Martinez et. al. (electrolyte electroreflectance)⁴, Rhiger et. al. (XPS)⁵, and Wilson et. al. (AES, Spectroscopic ellipsometry)⁶ have measured excess Te on the surface. Rhiger et. al. concluded that the near surface region is Te or Hg enriched depending on the etch method with a thin layer (~ 20 Å) of TeO₂ on the surface. Aspnes et. al., however, has concluded that there was a 7 Å thick layer of amorphous metallic Te on the surface which oxidized to form TeO₂ upon exposure to air. Rhiger et. al. and Lastras-Martinez et. al. further suggested that there was a depletion of Cd and thus a change in the composition near the surface while Aspnes et. al. suggested that the stoichiometry of the HgCdTe was preserved beneath the thin amorphous Te layer. Ozone ash etching has also been employed to clean the HgCdTe surface before passivation. Ozone, O₃, is reacted with surface hydrocarbons, and the reacted compounds are volatilized upon exposure to ultraviolet radiation. Wilson reported that HgCdTe surfaces cleaned with this process gave devices with much better electrical characteristics which may be due to a cleaner surface (i.e. less surface contaminants)⁷. From the brief summary above, it is clear that various surface treatments can alter the surface stoichiometry but that more investigations are needed in order to understand the details and nature of the effects of the surface treatments on HgCdTe.

In our experiments, HgCdTe alloys were grown under different conditions and subject to different cleaning procedures. One of the objectives of the work was to observe the valence band structure and to locate the Fermi level ($E_{f,s}$) at the surface. Another objective was to examine any changes in surface stoichiometry. A third objective was to monitor the cleanliness of the surface, i.e. presence of carbon and/or oxygen, and the effect of *in situ* ultraviolet exposure upon cleaning the sample surface. A final objective was to correlate this work with previous work in the literature.

II. EXPERIMENTAL PROCEDURES

The HgCdTe materials that were examined in the VG ESCALAB machine were grown by several different methods and given varying surface treatments. The materials studied had been grown by solid state recrystallization (SSR), horizontal zone melt (HZ), liquid phase epitaxy (LPE), and vapor phase epitaxy (VPE). The surface preparation techniques employed were the standard process "A" which was a chemo-mechanical polish with bromine in dimethylformamide (DMF)⁷ followed by a solvent clean and a 1/16 % bromine in ethylene glycol (1/16 % Br in EG) spray etch and process "B" which was an ozone ash etch followed by a 1/16 % Br in EG spray etch. Each technique is preceded by a solvent rinse. Variations of these two etching techniques were also employed. All of these processes were performed in an inert N₂ atmosphere. The samples were sealed in a N₂ package for delivery to Stanford from Santa Barbara Research Center (SBRC) and then mounted and transferred to the VG ESCALAB system using a N₂ filled glove bag. The samples were transferred to the UHV chamber with techniques employed to minimize exposure to ambient.

XPS spectra were obtained with the Stanford VG ESCALAB system with the twin anode nonmonochromatic source using Mg K α (1253.6 eV) at 15kV and 10mA. The pass energy of the hemispherical energy analyzer (HEA) was set to 50 eV for the wide scans and 20 eV for the narrow scans. UPS spectra were collected for the He I (21.2 eV) and He II (40.8 eV) lines by operating the helium lamp at low pressures ($\sim 2 \times 10^{-2}$ mbar) in order to enhance the He II line emission. The pass energy of the energy analyzer was set to 5 eV for the He I spectra and 20 eV for the He II spectra.

A Hg lamp was used for the ultraviolet exposure of two of the samples. The samples were exposed in incremental exposure times up to several minutes after all the initial XPS and UPS data had been taken. Measurements were made to see if this UV radiation produced any cleaning effect on the surface.

III. RESULTS

A cumulative total of 20 samples have been investigated thus far in this ongoing study of technologically important surfaces. This report focuses on five samples in particular due to a more detailed analysis that was performed on the spectra of these samples. These samples include: two SSR samples (samples 1 and 2, $x=0.3$ bulk, oriented (111)), a VPE sample (sample 3, (111)), a LPE sample (sample 4, (111)), and a HZ sample (sample 5, $x=0.3$ bulk, random orientation). Only surface stoichiometry and Fermi level will be reported for the rest of the SSR, HZ and LPE samples studied.

Typical valence band spectra obtained with the He II UPS line are shown in Figures 1a-e. There are several distinguishing features represented in these spectra. The most prominent peaks correspond to the Hg 5d lines, and the intensities of these peaks vary among the samples. Interesting features occur at lower binding energies (from -0 - 7eV). At kinetic energies of ~38 and ~40 eV, emission occurs from the Hg 5d peaks excited by the He III (48.4 eV) line. Figures 1a,d show increased emission from the 37 eV kinetic region which indicates the presence of oxygen 2p emission⁸. There exists a prominent shoulder in the vicinity of 35 eV kinetic energy which varies in intensity and width from sample to sample. This feature is lowest in intensity for the vapor phase epitaxial sample shown in Figure 1c.

The surface Fermi level position above the VBM was determined for each sample. The location of the Fermi level position for the instrument was facilitated by using a Ag standard since this level is constant for the system. Using the He I line to excite electrons from the valence band of the Ag, the VBM was assigned the energy value at which the photoelectron emission approached 0 count rate (Fig.2). This energy value was found to be 20.95eV kinetic energy. To determine the Fermi level in the He II spectrum, 19.6 eV (HeII-HeI) was added to give a Fermi level of 40.55eV. The VBM for the HgTeCd was assigned a value of 7.9eV above the Hg5d_{5/2} core peak. This value was obtained by Silberman in UPS angle resolved photoemission studies of HgTeCd⁹ The

values of ($E_{f,s}$ -VMB) obtained from samples 1-5 are compiled in Table I. Values for all of the samples studied are summarized in Table II. This table includes the surface etching technique and resulting surface stoichiometry and Fermi level for the SSR, HZ, and LPE samples studied.

The surface stoichiometry for each sample was obtained using XPS analysis. Figure 3 shows the wide survey scans for samples 1-5. Analysis of the peak energies indicates that the major constituents at the surface are Hg, Cd, Te, C, and O. The C and O are contaminants which are probably due to the surface preparation. The energies of the Hg, Cd, and Te peaks are located at positions which indicate that these constituents are bonded together to form HgTeCd. There are no prominent elemental peaks in this spectrum. The calculated surface compositions of Hg, Cd, and Te for samples 1-5 are shown in Table III. These values are shown for all the samples in Table II. The values were calculated using the relation

$$C_x = \frac{A_x/S_x}{\sum A_i/S_i} * 100$$

where C_x is the concentration of component x (x = Hg, Cd, or Te) in atomic percent, A_x is the area under peak x , and S_x is the atomic sensitivity factor of the peak that we are analyzing. The S_x 's for the peaks analyzed are: 3.1 for the Hg $4f_{7/2}$, 2.55 for the Cd $3d_{5/2}$, and 4.0 for the Te $3d_{5/2}$. These factors arise from the fact that the HEA has a transmission efficiency that is a function of energy. The values listed above and used in our analysis were obtained from the Phi Handbook¹⁰. These values are for a different type of analyzer than the HEA. Standards must be run in the VG ESCALAB to determine the S_x 's for this HEA in order to provide more accurate compositional analysis on this instrument.

In determining the percent compositions at the surface, only the Hg, Cd, and Te were considered. To calculate the surface x value for each sample of $\text{Hg}_{1-x}\text{Cd}_x\text{Te}$, the formula unit was written as $(\text{Hg}_{1-z}\text{Cd}_z)_{1-y}\text{Te}_y$ since the surface cation/anion ratio was not equal to unity. Then x is given by

$$x = \frac{(1-y)z}{y}$$

where y = percent Te, and $z = \% \text{Cd} / (\% \text{Cd} + \% \text{Hg})$.

The narrow scans of the Te 3d's reveal that samples 1 and 4 show a significant presence of TeO_2 while samples 2 and 5 exhibit no oxide. Since Te bonded in TeO_2 has a valence of +4, there exists a chemical shift of this Te peak from the substrate value ($\text{Te}^{2+} E_b = 572.7 \text{ eV}$) to the Te^{+4} ($E_b = 576.3$) value in the oxide.⁵ Sample 5 shows asymmetric broadening about the Te bulk peak suggesting the presence of Te(O) ($E_b = 573 \text{ eV}$).⁵

Qualitative observations of the contaminant concentrations at the surface and the presence of TeO_2 for samples 1-5 are shown in Table IV. As can be seen in this table, samples 3, 4, and 5 have more carbon than sample 2. No narrow C or O scans were made for sample 1. The epi-samples (3, 4) had more oxygen on their surfaces than the other samples, but sample 3 was the only one of these two to exhibit significant TeO_2 .

IV. DISCUSSION

A comparison between our He II UPS spectra with cleaved and oxidized spectra (Fig. 5)¹¹ of HgCdTe reveals significant differences. The cleaved or atomically clean spectrum and the oxidized spectrum have much sharper features. The Hg 5d core lines have greater intensity and the Cd 4d core levels are evident in the cleaved and oxidized spectra. Our samples exhibited a large shoulder in the region of 35 eV kinetic energy (-5 eV binding energy) while this feature is not present on the cleaved or oxidized spectra. Sample 3, however, exhibits sharper features which more closely approach those of the cleaved sample. Thus, our samples were not atomically clean. The presence of carbon and oxygen in the XPS wide (Fig. 3) and narrow (table IV) scans confirms this observation. Samples 1 and 3, which had the presence of TeO_2 on the

surface as revealed from the XPS measurements, have a greater signal intensity around 37 eV kinetic energy (-3.5 eV binding energy) which corresponds to the oxygen 2p emission in Figures 5,8.

The photoemission spectrum for amorphous Te (Fig. 6)¹² shows significant valence band features near - 5 eV binding energy which corresponds to 35.5 eV kinetic energy in our spectra. Since our spectra have significant valence band features around 35 eV, amorphous Te may be present on the surface of our samples which would agree with the results of Aspnes et. al.³ One conclusion to be drawn to this point is that the kinetic energy region between 34 and 37 eV in the UPS spectra could be a mixture of emission from amorphous Te, carbon, and oxygen.

The surface Fermi level ($E_{f,s}$) lies approximately 0.2 eV above the VBM (Tables I, II) which is the nominal bandgap of these materials and indicates that the sample surfaces were *n*-type. This is very interesting in light of the fact that some of this material exhibited bulk *p*-type behavior. $E_{f,s}$ for sample 3, however, lies 0.3 eV above the VBM. This sample may have had a larger energy bandgap than the other samples (we haven't yet obtained the *x*-value for this sample), or else the material was degenerate *n*-type. We did not observe emission of electrons near the conduction band minimum which would give information on degenerate behavior, but this is not surprising since the density of states is very small near this point. The oxidized samples (1 and 3) had $E_{f,s}$ closest to the VBM which may be due to the effect of oxygen on the surface of these samples (eg. surface states). Sample 3, which had the lowest shoulder intensity around 35 eV, had $E_{f,s}$ furthest from the VBM which may indicate the effect of surface contaminants and amorphous Te .

Comparison of our UPS He I spectrum (Fig. 7) for sample 3 with that of an oxidized cleaved sample (Fig. 8)¹¹ shows sharp differences. Since our He II spectra show large Hg 5d electron emission, the difference between the He I spectra cannot be explained on the account of our sample being "dirty" since the same Hg 5d peaks should

also show up in the He I spectrum. One explanation for this difference is that the HEA may have difficulty detecting low kinetic energy electrons. The spectrum in Figure 8 was obtained with a double pass CMA.

Table III illustrates the stoichiometry changes which may be present near the surface of samples 1-5. Samples 2-5 show significant Te enrichment and Cd deficiency at the surface in agreement with the work of the previous authors cited.³⁻⁶ The Cd deficiency was determined by comparing the calculated x-values with the nominal x-value of 0.3. An x-value less than 0.3 was interpreted as a Cd deficiency. Note that samples 1 and 2 were grown the same way and cleaned with the same surface preparation but have strikingly different XPS peak intensities. Sample 1 agrees approximately with the nominal x-value and even shows a slight Cd enrichment. The difference between the results of sample 1 and 2 could be explained by the fact that different (111) faces were studied, either the Cd or Te terminated face. This is possible because HgCdTe crystallizes in the zinc-blende structure which is acentrosymmetric and thus the (111) faces are different. For all of the rest of the samples studied, the surface is depleted of Cd independent of the material growth technique or surface preparation. Table II summarizes these results.

The oxide (TeO_2) formation on the surface of samples 1-5 is summarized in Table IV. If the samples were somehow exposed to an ambient containing oxygen, all of the samples should have had the same exposure since they were prepared and mounted under similar conditions. Since the samples show various degrees of surface oxidation, one conclusion is that there are differences in the reactivity and kinetics of the various sample surfaces. It is not clear from our data if this is due to differences in material growth or surface preparations. The amount of TeO_2 formed on our three oxidized samples (samples 1,3,4) is much less than for samples left out in air.^{5,13}

Finally, the samples were exposed to ultraviolet light to investigate the feasibility of this technique for cleaning sample surfaces. Figures 1d and 1e show the

results of our efforts. Sample 5 (Fig. 1e), which was not oxidized, appeared to be cleaned to some extent. The Hg 5d lines increased in intensity and the large and broad shoulder decreased significantly in intensity. From XPS analysis, the Te intensity increased. All of these results suggest that surface contaminants such as carbon and oxygen were removed but not Te. Hence, the UPS shoulder does not have a large contribution from amorphous Te which had been suggested earlier. However, sample 4 (Fig. 1d), which contained significant TeO₂ on the surface and had similar amounts of carbon as sample 5, exhibited no change in the UPS spectrum which suggests that the surface contaminants were bound tighter to the surface.

V. SUMMARY

Several conclusions can be drawn at this point in our continuing study of HgCdTe surfaces that are prepared for subsequent processing. The etching and cleaning techniques clearly alter the surface. The three main conclusions concerning the change of the surface are:

- 1) Independent of material growth technique of surface preparation, the valence band electronic structure of the resulting surfaces are altered from that of atomically clean surfaces, with increased emission probably due to O and C contamination and/or oxidized TeO₂ or elemental Te.
- 2) All of the samples studied exhibited *n-type* behavior subsequent to the surface preparations.
- 3) All but one of the samples was Cd deficient after surface preparation. One explanation of sample 1's Cd increase could be that different (111) faces were studied, either the Cd or Te terminated face.

Although these experiments have shed some light on the effects of surface preparation on HgCdTe, there is still a lot of uncertainty and many questions need to be answered. Different surface preparations on identical samples could provide more insight. The results from exposure to ultraviolet light suggest a possible method for

cleaning surface contaminants such as carbon and oxygen. The quantitative analysis can be greatly improved upon calibration of the XPS sensitivity factors with analysis of an atomically clean sample such as a cleaved sample.

REFERENCES

- ¹W.F.H. Mickelthwaite, *Semiconductors and Semimetals*, vol. 18, Academic Press, 1981
- ²see section 2, this report
- ³D.E. Aspnes and H. Arwin, *J. Vac. Sci. Technol.*, A 2(3) 1309 (1984)
- ⁴A. Lastras-Martinez, U. Lee, J. Zehnder, and P.M. Raccach, *J. Vac. Sci. Technol.*, 21(1) 157 (1982)
- ⁵D.R. Rhiger and R.E. Kvass, *J. Vac. Sci. Technol.*, 21(1) 168 (1982)
- ⁶J.A. Wilson and V.A. Cotton, *J. Vac. Sci. Technol.*, A 1(3) 1719 (1983)
- ⁷J.A. Wilson (Santa Barbara Research Center), private communication
- ⁸J.A. Silberman, unpublished work
- ⁹J.A. Silberman, private communication
- ¹⁰Phi Handbook of X ray Photoelectron Spectroscopy, 1979
- ¹¹J.A. Silberman, P. Morgen, I. Lindau, W.E. Spicer, and J. A. Wilson, *J. Vac. Sci. Technol.*, 21(1) 154 (1982)
- ¹²N. J. Shevchik, M. Cardona, and J. Tejada, *Phys. Rev. B*, 8 (6) 2833 (1973)
- ¹³J. F. Wager, D. R. Rhiger, *J. Vac. Technol.*, A 3(1) 212 (1985)

TABLE I : Position of surface Fermi level ($E_{f,s}$) relative to the valence band maximum (VBM).

SAMPLE	SAMPLE PROCESS #	CLEANING PROCEDURE	Hg 5d ^{5/2} (eV)	VBM (eV)	$E_{f,s}$ - VBM (eV)
1	RSC-209-1-13	A	32.47	40.37	0.18
2	RCS-209-1-20	A	32.45	40.35	0.20
3	VTIE-28C	B	32.35	40.25	0.30
4	F6067	B	32.50	40.40	0.15
5	ZH-258-2D	B	32.45	40.35	0.20

$E_{f,s}$: SURFACE FERMIL LEVEL= 40.55 (from Ag standard)

VBM: VALENCE BAND MAXIMUM

TABLE II: SUMMARY OF SURFACE STOICHIOMETRY AND FERMI LEVEL FOR THE SSR, HZ, AND LPE MATERIAL

SAMPLE	GROWTH TECHNIQUE	ETCHING TECHNIQUE	SURFACE x-VALUE	$E_{f,s}$ -VBM (eV)
II 241 A	SSR	lap ¹ & 1/16 spray ²	0.185	0.15
II 241 B		1/16 spray	0.219	0.15
III 241 A		lap & 1/16 spray	0.25	0.20
III 241 B		1/16 spray	0.23	0.25
IV A 209-1-13 (SAMPLE 1)		lap & 1/16 spray	0.32	0.18
IV A 209-1-20 (SAMPLE 2)		lap & 1/16 spray	0.22	0.20
II ZH-247 A	ZH	lap & 1/16 spray	0.18	0.15
II ZH-247B		1/16 spray	0.20	0.15
III 247 3C		lap & 1/16 spray	0.23	0.15
III 247 3D		1/16 spray	0.23	0.15
IV 258-2D (SAMPLE 5)		UV-O ₃ ³ & 1/16 spray	0.19	0.20
II LPE 148 A	LPE	lap & 1/16 spray	0.16	0.15
II LPE 148 B		1/16 spray	0.20	0.15
III LPE 148 A		UV-O ₃ & 1/16 spray	0.22	0.15
III LPE 148 B		1/16 spray	0.23	0.15
IV F6067		UV-O ₃ & 1/16 spray	0.22	0.15

¹lap: 2% bromine in DMF ...p

²1/16 spray: 1/16 % bromine in EG spray etch

³UV-O₃: Ozone oxidation ash etch

TABLE III: Surface stoichiometry

SAMPLE	SAMPLE PROCESS #	CLEANING PROCEDURE	NOMINAL X VALUE	Hg4f _{7/2} %	Cd3d _{5/2} %	Te3d _{5/2} %	SURFACE X VALUE
1	RCS-209-1-13	A	0.3	32.9	16.3	50.9	0.32
2	RCS-209-1-20	A	0.3	29.5	12.7	57.7	0.22
3	VTIE-28C	B	--	33.5	12.5	54.0	0.23
4	F6067	B	--	35.9	11.5	52.6	0.22
5	ZH-258-2D	B	0.3	31.6	10.8	57.6	0.19

TABLE IV: Presence of C, O, TeO₂ on sample surface

SAMPLE	SAMPLE PROCESS	C 1s AREA	O 1s AREA	Te oxide (Å) AREA
1	RCS-209-1-13	--	--	significant
2	RCS-209-1-20	x ¹	y	negligible
3	VTIE-28C	2x	2y	significant
4	F6067	2x	2y	slight
5	ZH-258-2D	2x	y	negligible

¹Area under the peak is denoted x. Therefore, 2x denotes twice this peak area.

FIGURE CAPTIONS

- FIGURE 1** UPS (He^{II}) valence band spectrum of (see text) a) sample 1, b) sample 2 c) sample 3, d) sample 4 showing VB before UV exposure (black) and after 12 min. UV exposure (blue) , and e) sample 5 showing before (upper) and after 7 min.(lower) UV exposure.
- FIGURE 2** UPS (He^{II}) valence band spectrum of Ag standard.
- FIGURE 3** Wide XPS scan for samples 1-5
- FIGURE 4** Narrow XPS scan showing Te3d lines for samples 1-5. Samples 1 and 3 show presence of TeO_2 .
- FIGURE 5** UPS (He^{II}) valence band spectra taken from an atomically clean (110) HgCdTe surface and with subsequent oxidations.
- FIGURE 6** X-ray photoemission data from amorphous and trigonal Te.
- FIGURE 7** UPS (He^{I}) valence band spectrum from sample 3 taken on VG ESCALAB.
- FIGURE 8** Typical UPS (He^{I}) valence band spectrum of oxidized cleaved $\text{Hg}_{0.69}\text{Cd}_{0.31}\text{Te}$ taken with double pass CMA in SPICERLAB.

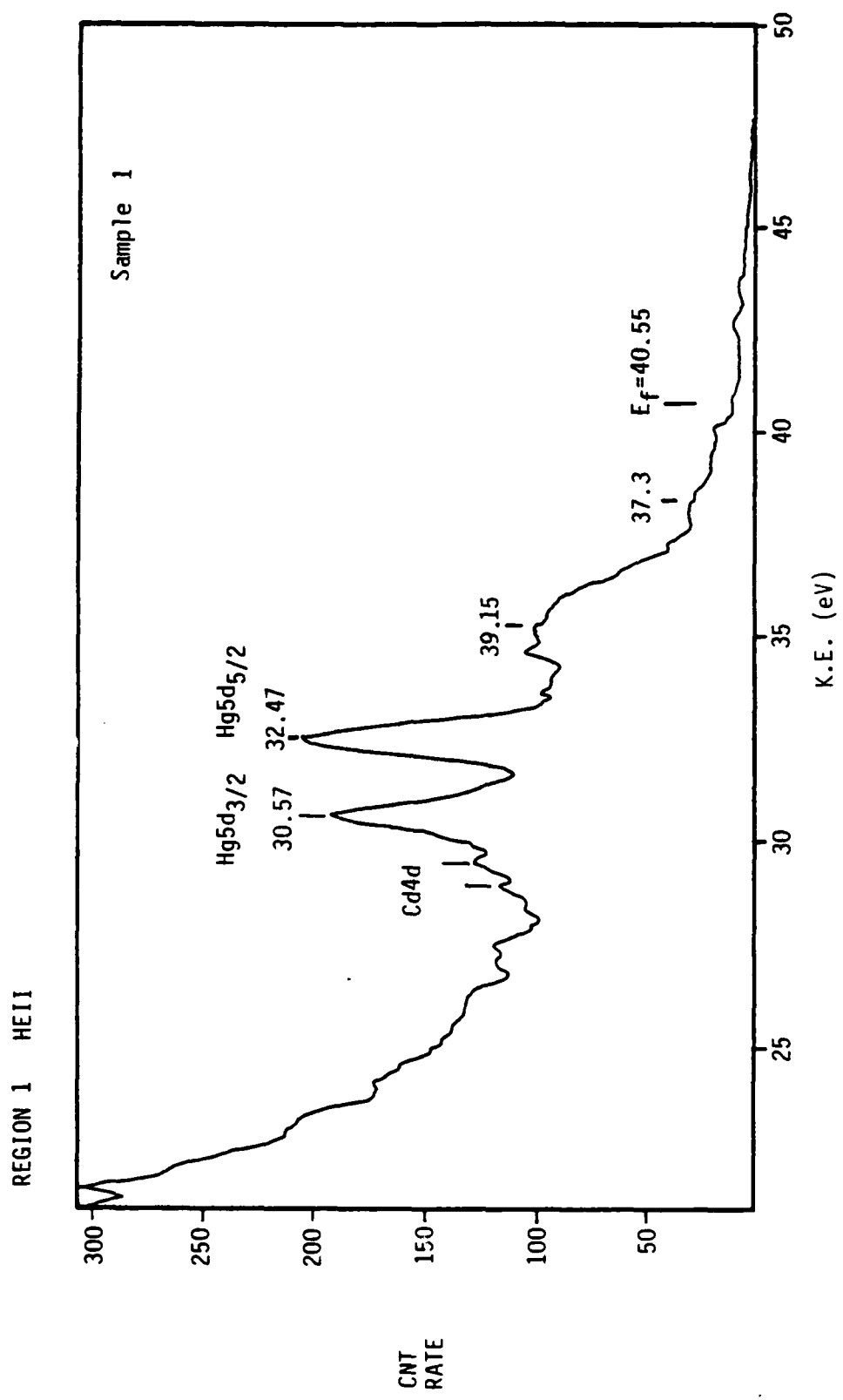


Figure 1a.

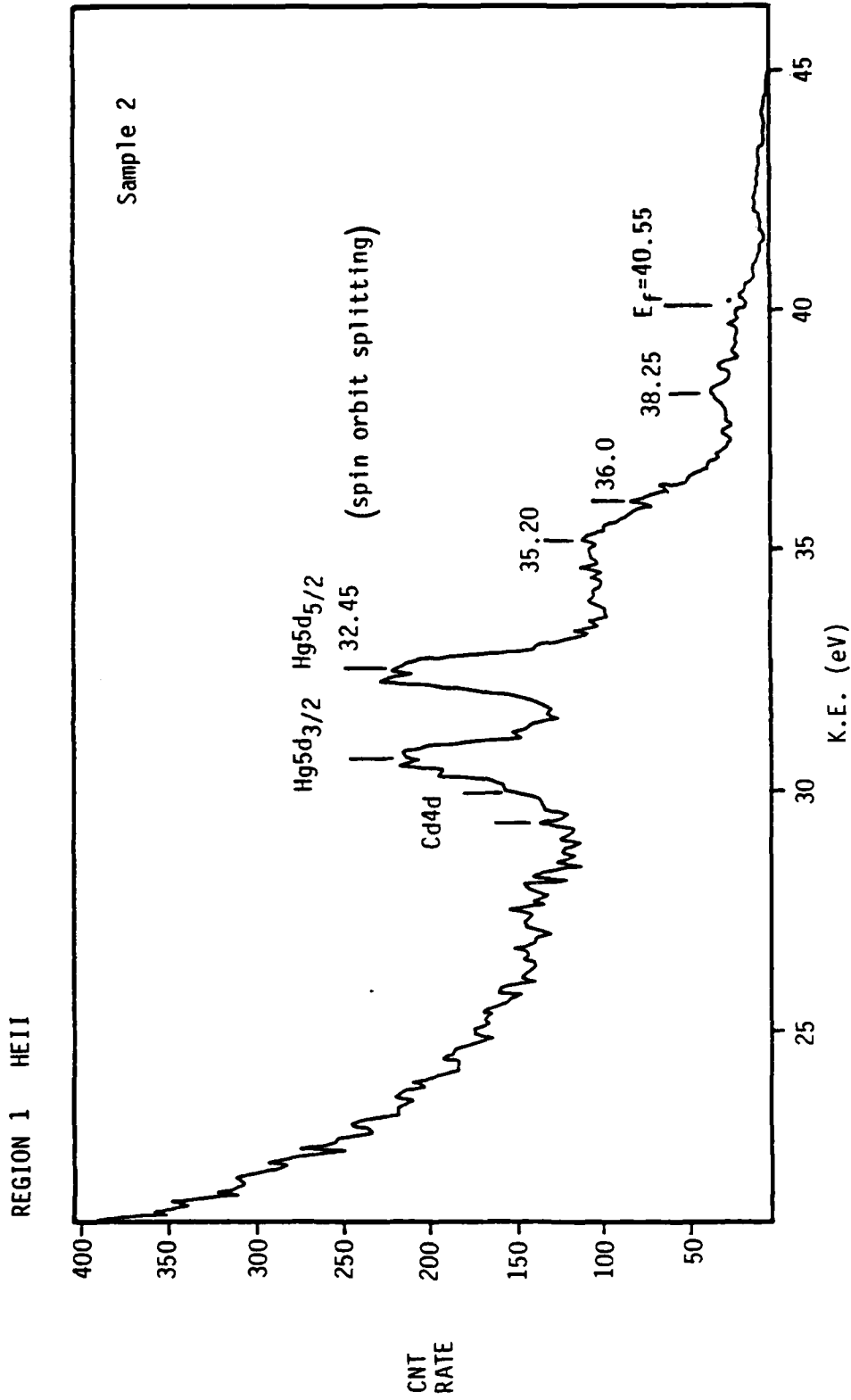


Figure 1b.

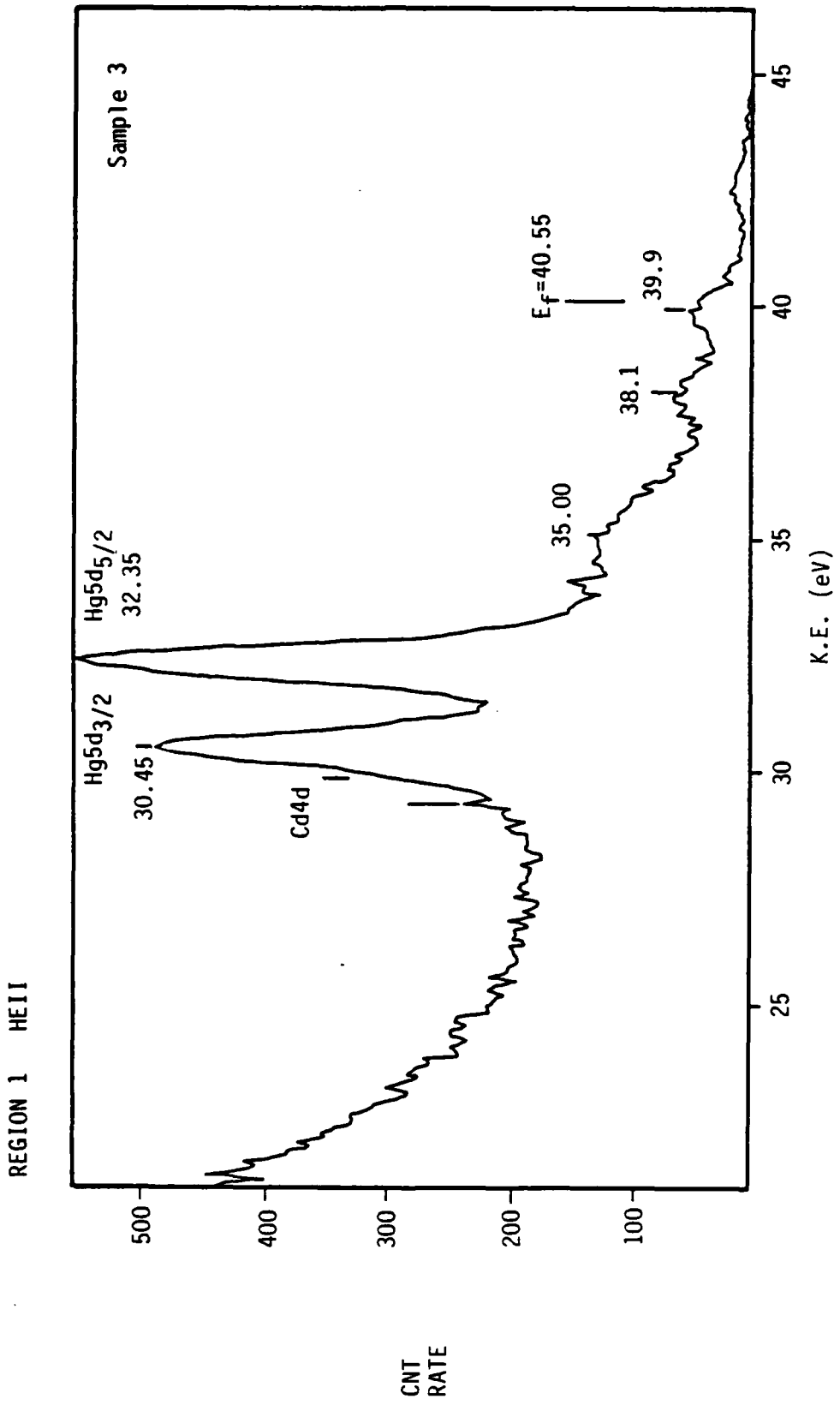


Figure 1c.

REGION 1 HEII

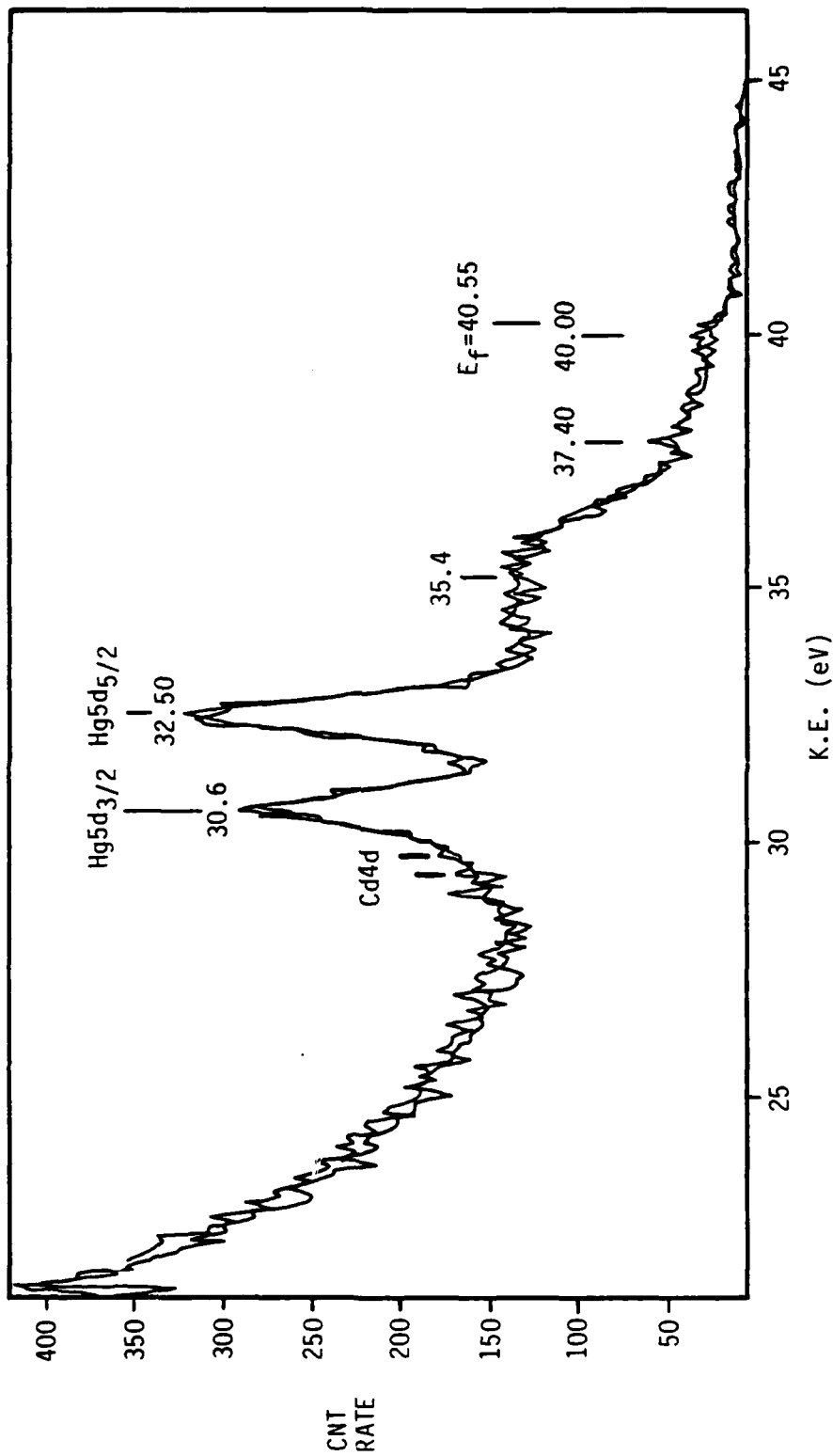


Figure 1d.

REGION 1 HELL

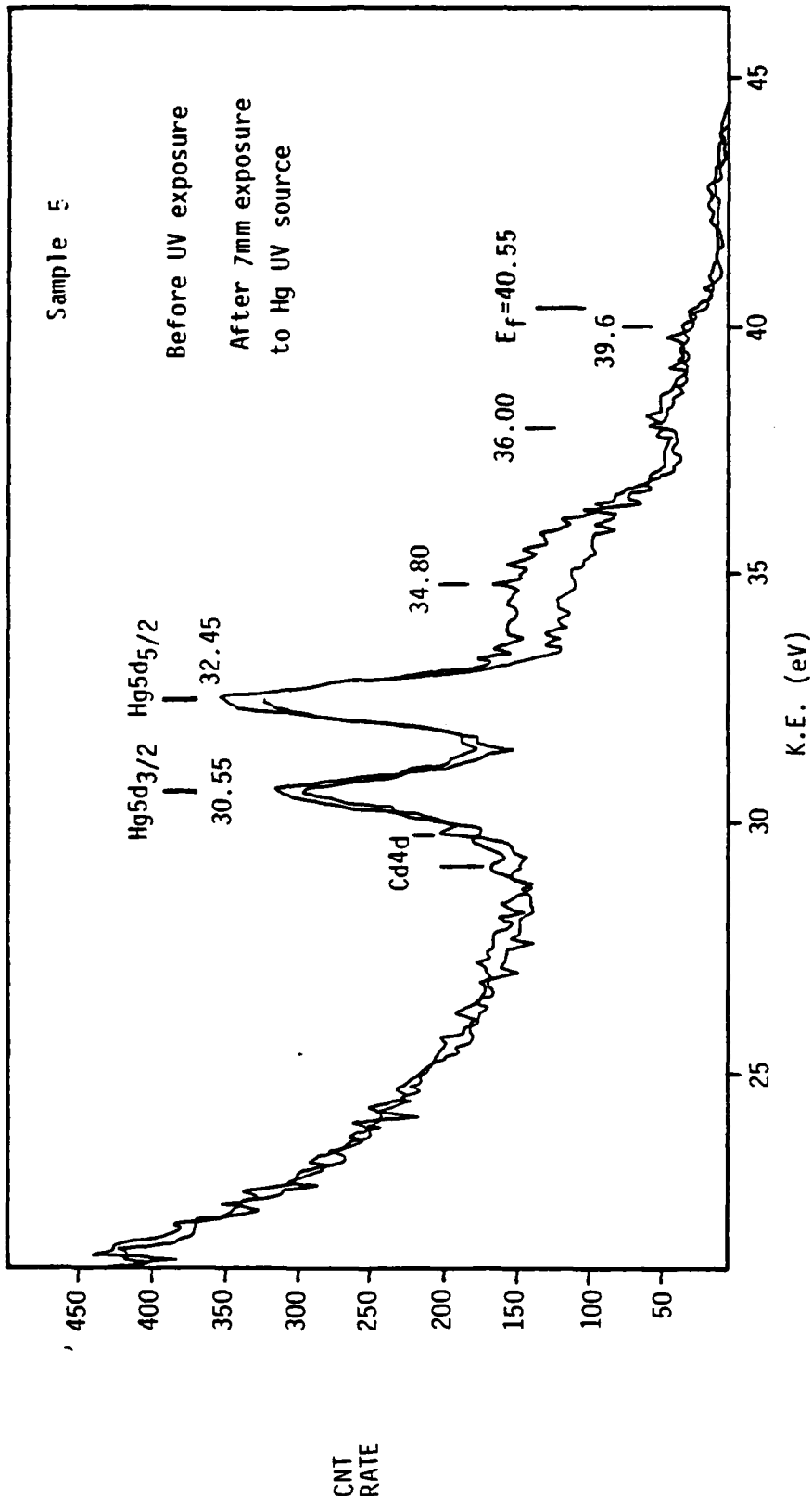


Figure 1e.

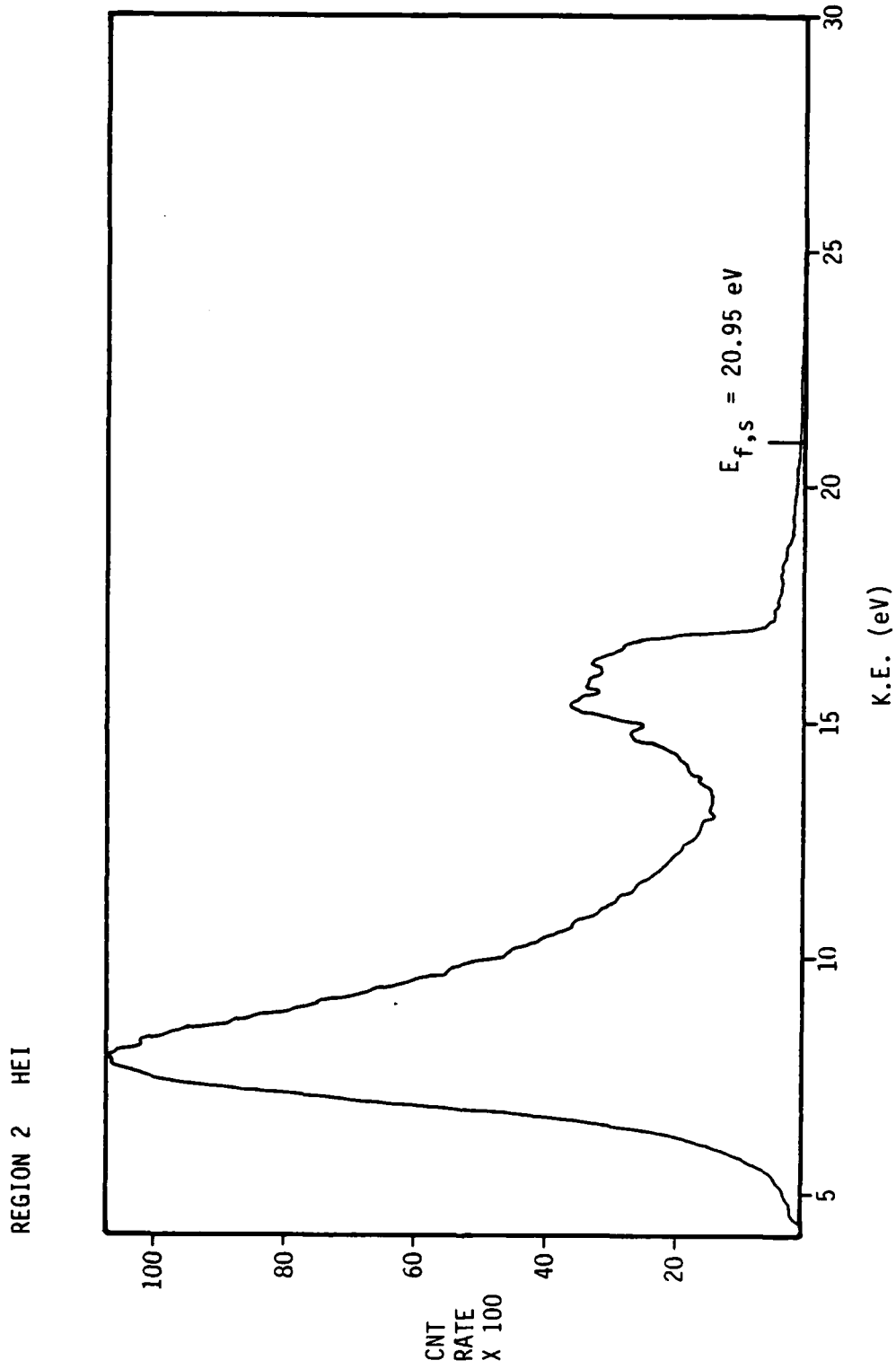


Figure 2.

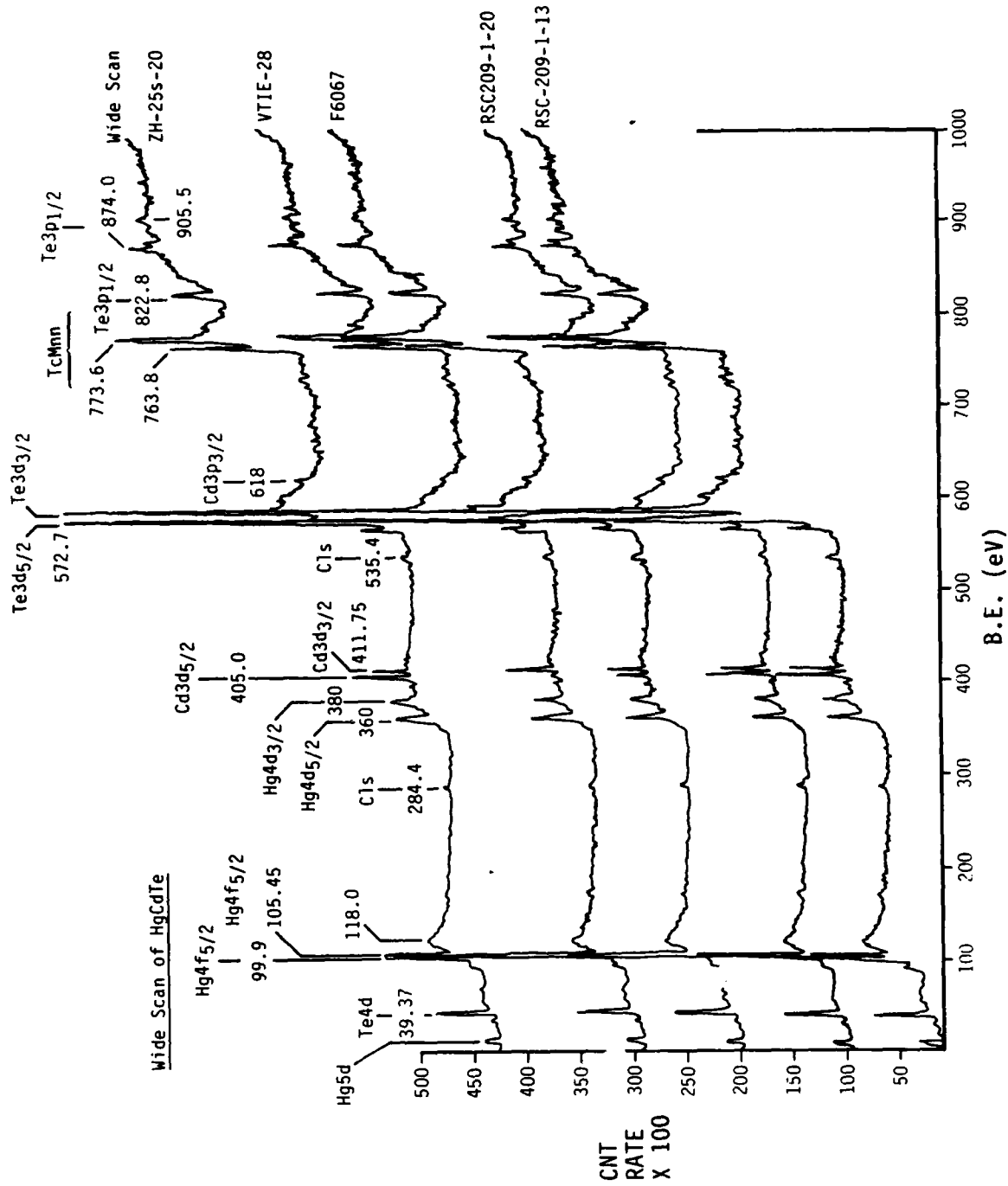
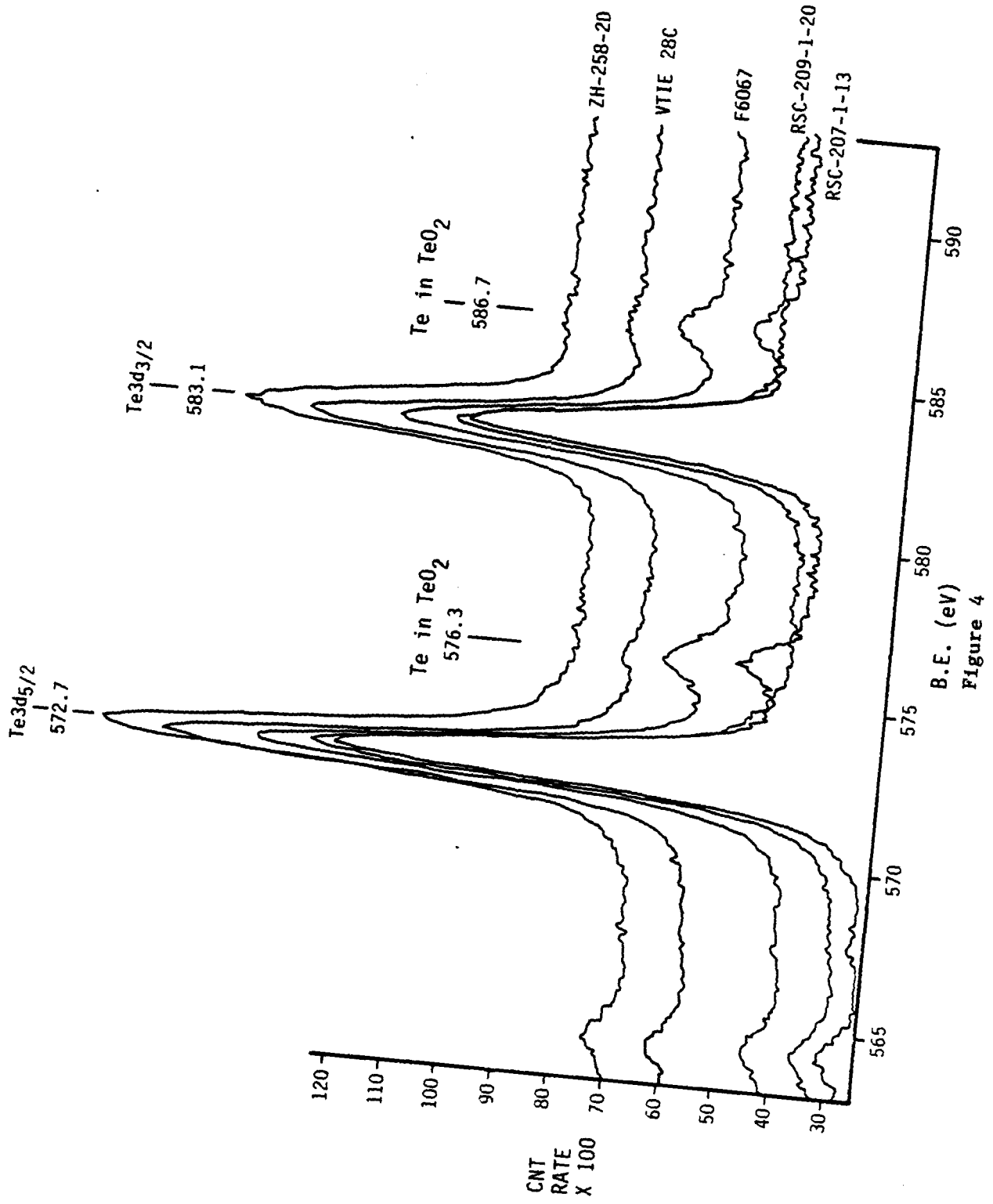


Figure 3



B.E. (eV)
Figure 4

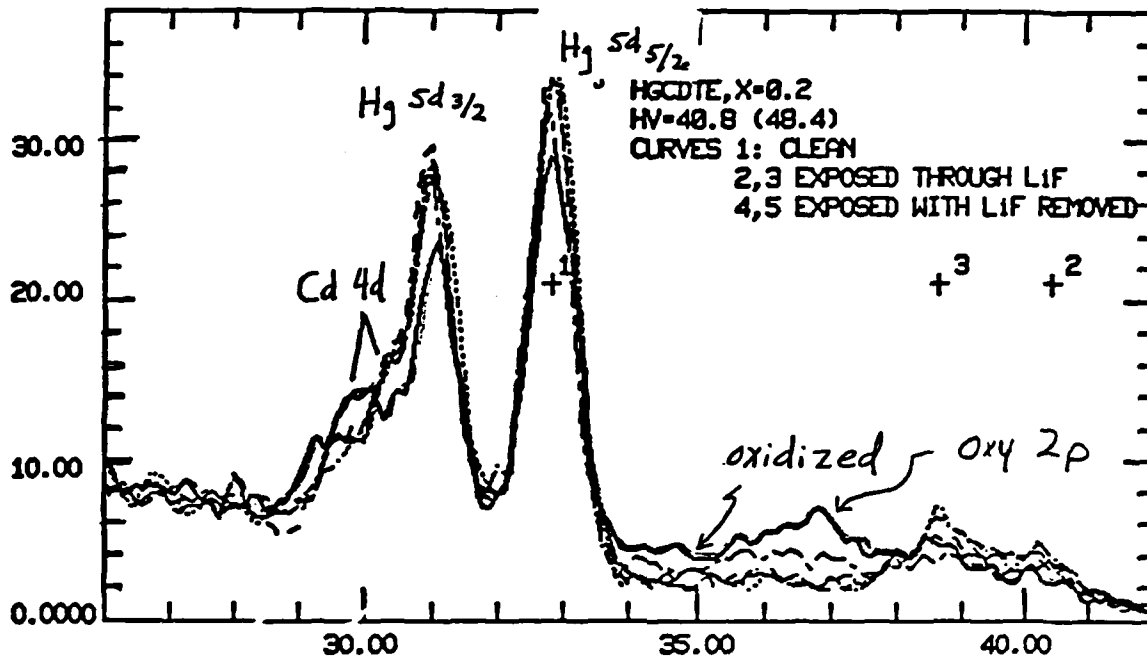


Figure 5

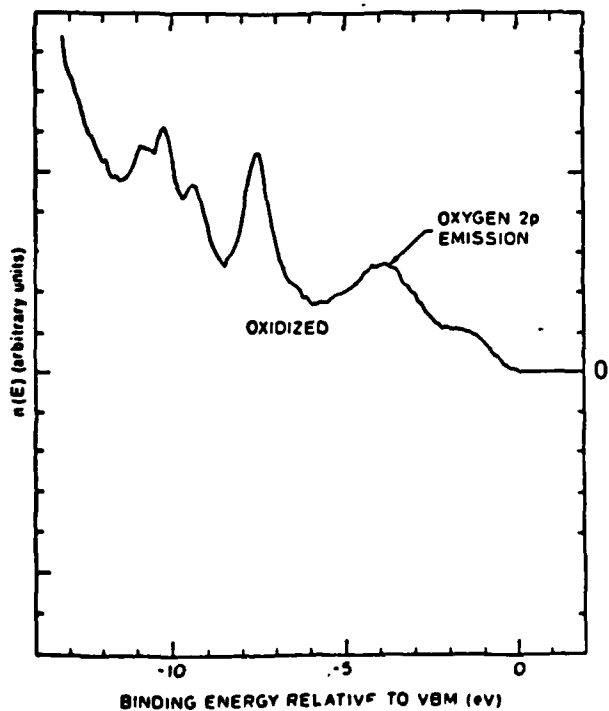


Figure 8

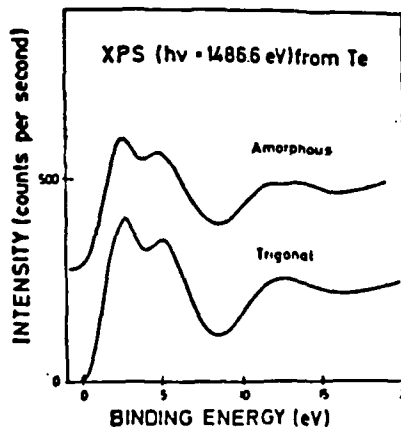


Figure 6

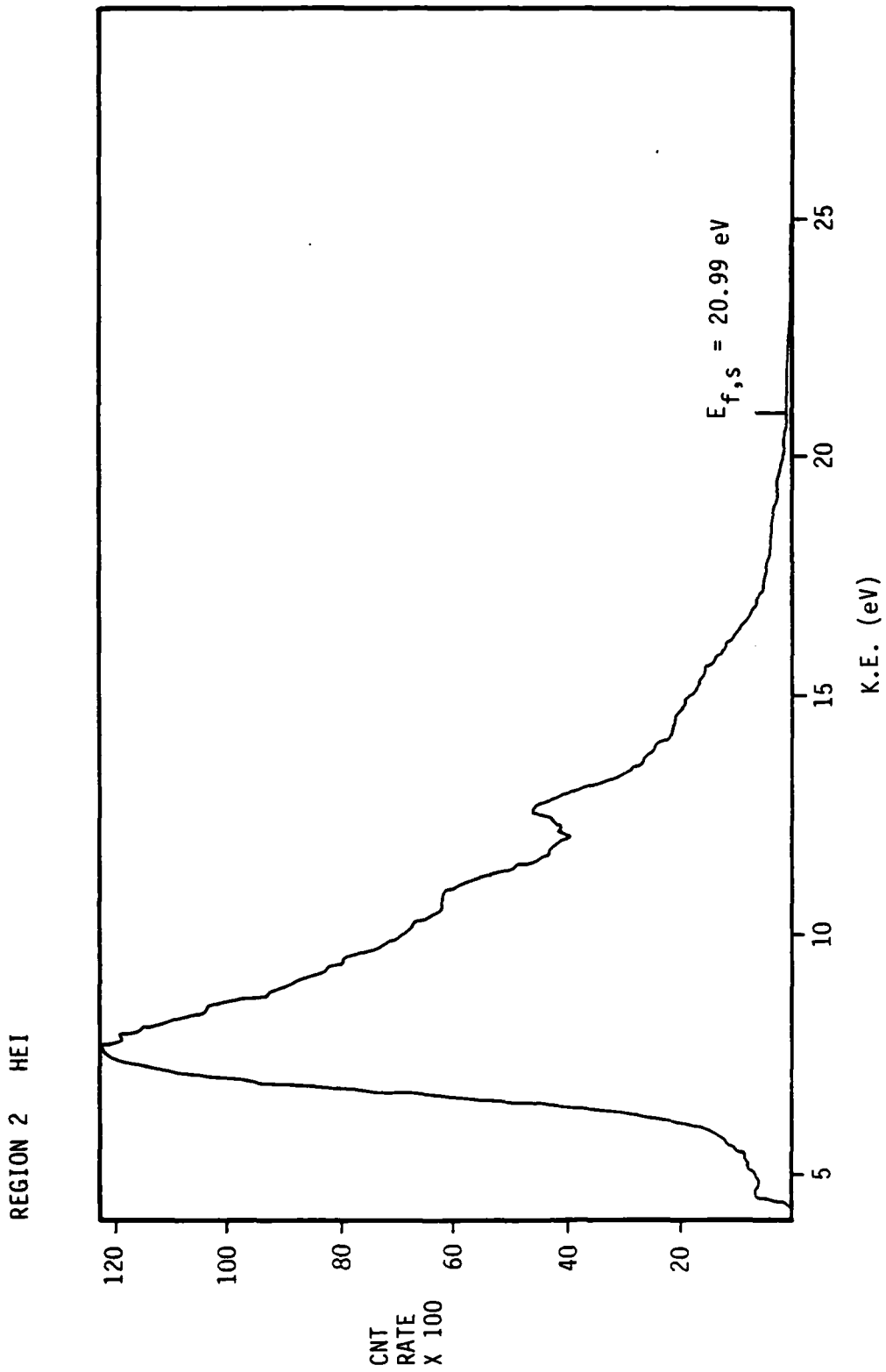


Figure 7.

ELECTRON BEAM INDUCED Hg DESORPTION STUDY ON $Hg_{1-x}Cd_xTe$

C. K. Shih and W. E. Spicer

I. Introduction

A detailed study of the electron beam induced Hg desorption on $Hg_{1-x}Cd_xTe$ has been carried out. This study enables us to gain insight into the surface bonding properties of $Hg_{1-x}Cd_xTe$ and provide some guidelines for using the characterization methods which utilize an electron beam as a probing source.

In general, the electron beam induced Hg desorption may originate from several different processes:

(1) electronic excitation of surface atoms leading to the process called electron stimulated desorption (ESD) [1,2,3],

(2) electron excitation of sub-surface atoms leading to the processes as ionization, defect production, bond breaking and diffusion,

(3) heating which may cause annealing, volatilization etc. at the surface.

Due to the thermal instability [4,5] and the low thermal conductivity (0.02 to 0.07 W/cm°C) of this material, the heating effect is especially important and needs to be investigated in detail. In appendix A, we model the heating effect of the material upon irradiation by an electron beam and show how the beam parameters can affect the heating effect. Possible processes will be discussed and the resulting surface composition after Hg depletion will also be presented. The resulting surface electronic structure will be emphasized in the coming quarterly report.

II. Experimental

$Hg_{1-x}Cd_xTe$ crystals with $x = 0.233$ were introduced through a transferring system into a UHV system which was equipped with cooling and heating capabilities. The sample was cleaved to produce an atomically clean (110)

surface. Electron beam induced Hg desorption was first studied by fixing the electron beam parameters and varying the substrate temperature. Because Auger electrons are emitted from the sample during irradiation by the rastering electron beam, Auger electron spectroscopy (AES) was used to monitor the surface composition during electron beam exposure. A fresh cleave surface was then produced and the electron beam was rastered over the whole surface. LEED, UPS and XPS were performed after the electron beam damage. Varying the detection angle of the analyser changes the surface sensitivity of XPS; and thus information of Hg concentration as function of depth up to 20 Å was obtained.

III. Results and Discussion

Figure 1 shows the Auger signals of Hg and Te as a function of electron beam irradiation time at different substrate temperatures. The beam parameters are: $E_0 = 3 \text{ KV}$, $I_0 = 40 \text{ } \mu\text{A}$, area = 1 mm x 0.7 mm, and $d_0 \approx 100 \text{ } \mu\text{m}$, where E_0 is the electron beam energy, I_0 is the beam current and d_0 is the electron beam diameter. With these beam parameters, the calculation shows the dynamical heating effect of a thermal spike at a given location with 13 μsec duration and amplitude, $T_{\text{max}} - T_{\text{sub}}$, estimated between 150°C - 300°C. The uncertainty is due to the uncertainty of the thermal conductivity. In Figure 1 one can find that Hg depletion is suppressed with cooling of the substrate. Combining this result with the calculation of the heating effect suggests that the electron beam heating plays the dominant role in the electron beam induced Hg desorption. One also finds the saturation of Hg signal after 60% depletion, and the accompanying increase of the Te signal by $\sim 20\%$. A possible explanation for this result is that only the top few (5 to 6) monolayers are depleted of Hg and the crystal collapsed with excess Te on the surface.

We found no detectable Hg deficiency after 3 hours of electron beam damage with beam parameters of: $E_0 = 2\text{kV}$, $I_0 = 10 \mu\text{A}$, area = 5 mm x 5.5 mm and $d_0 = 250 \mu\text{m}$. With I_0 raised to 33 μA (other parameters fixed) we obtained ~ 22% of Hg depletion on the surface after 60 minutes. The fact that the electron dose for both cases are similar suggests that the ESD mechanism [1,2,3] is not applicable. However, the calculation shows that the heating effect is negligible for the low beam current case ($I_0 = 10 \mu\text{A}$) and the higher beam current case ($I_0 = 33 \mu\text{A}$) case yields a mild heating effect (thermal spike with ~ 50°C amplitude and 6.7 μsec duration) which again suggests the importance of heating in the electron beam induced Hg desorption of $\text{Hg}_{1-x}\text{Cd}_x\text{Te}$.

Figure 2 shows the ratio of Hg4f/Te3d peak intensities normalized to that of the cleaved surface as a function of effective escape depth. A simplified deconvolution (appendix B) of the curve yields the information of Hg concentration as a function of depth. It shows that only the top few monolayer are depleted of Hg which is consistent with the data in Figure 1.

IV. Summary

Electron beam heating effect plays a major role in the electron beam induced Hg desorption (we don't exclude the possibility that electronic excitation may be incorporated in the bond-breaking process). This is probably due to the volatility of the Hg atoms. Hg depletion is saturated after a few monolayers are depleted of Hg, leaving the surface with excess Te. The surface Te layer may act as an activation barrier for the outdiffusion of the Hg atoms from the sub-surface to the surface.

APPENDIX A

ELECTRON BEAM HEATING EFFECT

The power deposited in a solid sample by an electron beam can cause heating of the sample. The differential equation of the heat conduction is

$$\partial T / \partial t = Q / C_p - \nabla \alpha \nabla T \quad (1)$$

where T = temperature

t = time

Q = power deposited per unit volume

C_p = heat capacity per unit volume

α = thermal diffusivity.

For a given position, the first term on the right hand side of the equation is related to the energy flow from the electron beam and the second term is related to the net flow from the temperature gradient.

Steady State: According to Pittway [6], the steady state temperature rise is directly proportional to the beam power ($I_p \times E_p$) and inversely proportional to both the thermal conductivity and the beam diameter. At the center of the beam the surface temperature rise is given by [7]:

$$T_m - T_s = P / (2\sqrt{2\pi} K_s r_b) \quad (2)$$

where: T_m = temperature at the center of the beam which is maximum

T_s = substrate temperature

P = power of the electron beam

K_s = thermal conductivity

r_b = beam diameter

For materials like $Hg_{1-x}Cd_xTe$, where the thermal conductivity is a function of temperature, K_s is the effective thermal conductivity which lies

between the maximum value and minimum value. For our purpose, let's assume K_g is a constant.

Transient Behavior: To know the transient heating effect at the center of the beam one needs to solve equation (1) $\partial T/\partial t = Q/C_p - \nabla \alpha \nabla T$. To a good approximation, on the surface the term $\nabla \alpha \nabla T$ is proportional to the difference between the surface temperature and the substrate temperature, $\nabla \alpha \nabla T \approx \beta(T-T_s)$. Then equation (1) becomes

$$\partial T/\partial t = Q/C_p - \beta(T-T_s) \quad (3)$$

At steady state $\partial T/\partial t = 0$

$$Q/C_p = \beta(T_m - T_s) \quad (4)$$

Thus the equation becomes

$$\partial T/\partial t = Q/C_p [1 - (T - T_s)/(T_m - T_s)] \quad (5)$$

The solution is

$$T(t) - T_s = (T_m - T_s)(1 - e^{-t/\tau}) \quad (6)$$

Where $\tau = C_p(T_m - T_s)/Q$ and Q can be approximate as $Q \approx P / \pi r_b^2 R_g$ (R_g is the range of incident electrons in the solid target).

Dynamical Heating effect of a rastering electron beam: We have obtained the heating effect at the center of an electron beam for the steady state and transient situations. We can then apply this knowledge to the heating effect of a rastering electron beam.

For a given position when the electron beam on a pass through, the temperature rises up and then falls down. The rising and falling time is characterized by τ and the duration time t_0 is determined by the spot size and the rastering area (see Fig 3). When the scanning line spacing is smaller than the spot size, similar thermal spike occurs when the next scanning line passes through.

APPENDIX B

Let us define

$S(l)$ = the normalized signal detected as a function of escape depth,

$f(x)$ = the normalized concentration as a function of depth.

where $0 < f(x) < 1$.

$$\text{then } S(l) = \frac{\int_0^{\infty} f(x)e^{-x/l} dx}{\int_0^{\infty} e^{-x/l} dx} = \frac{\int_0^{\infty} f(x)e^{-x/l} dx}{1}$$

In principle one can deduce $f(x)$ from $s(l)$ which requires a lot of data points of $S(l)$ up to a very large l and is usually not obtainable. However, we can use the approximation (I called it layer approximation):

$$S(l_n) = \frac{\sum_{i=1}^n f(l_i) \Delta l_i}{l_n} \quad \text{where } \Delta l_i = l_i - l_{i-1}$$

$$\text{then } F(l_n) = \frac{S(l_n)l_n - S(l_{n-1})l_{n-1}}{\Delta l_n}$$

References

1. T. E. Madey and J. T. Yates, Jr., Electron Stimulated desorption as a Tool for Studies of Chemisorption: A Review, *J. Vac. Sci. Technol.* 8 (1971) 525.
2. D. Menzl, Desorption methods in: *Topics in Applied Physics*, ed. R. Gromer, Vol. 4 (Springer-Verlag, Berlin, 1975) p. 10.
3. M. L. Knotek and P. J. Feibelman, Ion Desorption by Core-hole Auger Decay, *Phys. Rev. Lett.* 40 (1978) 964.
4. R. F. C. Farrow, G. R. Jones, G. M. Williams, P. W. Sullivan, W. J. O. Boyle, and J. T. M. Witherspoon, *J. Phys. D* 12, 417 (1979).
5. K. C. Dimiduk, W. G. Opyd, J. F. Gibbons, T. W. Sigmon, T. J. Magee, R. D. Ormond, *J. Vac. Sci. Technol.* A 1 (3) 1661.
6. L. G. Pittaway, The Temperature Distributions in this Foil and Semi-Infinite Targets Bombarded by Electron Beam, *Br. J. Appl. Phys.* 15 (1964) 967.
7. Ali A. Iranmanesh and R. F. W. Pease, Temperature Profiles in Solid Targets Irradiated with Finely Focused Beams, *J. Vac. Sci. Technol.* B 1 (1), 91 (1983).

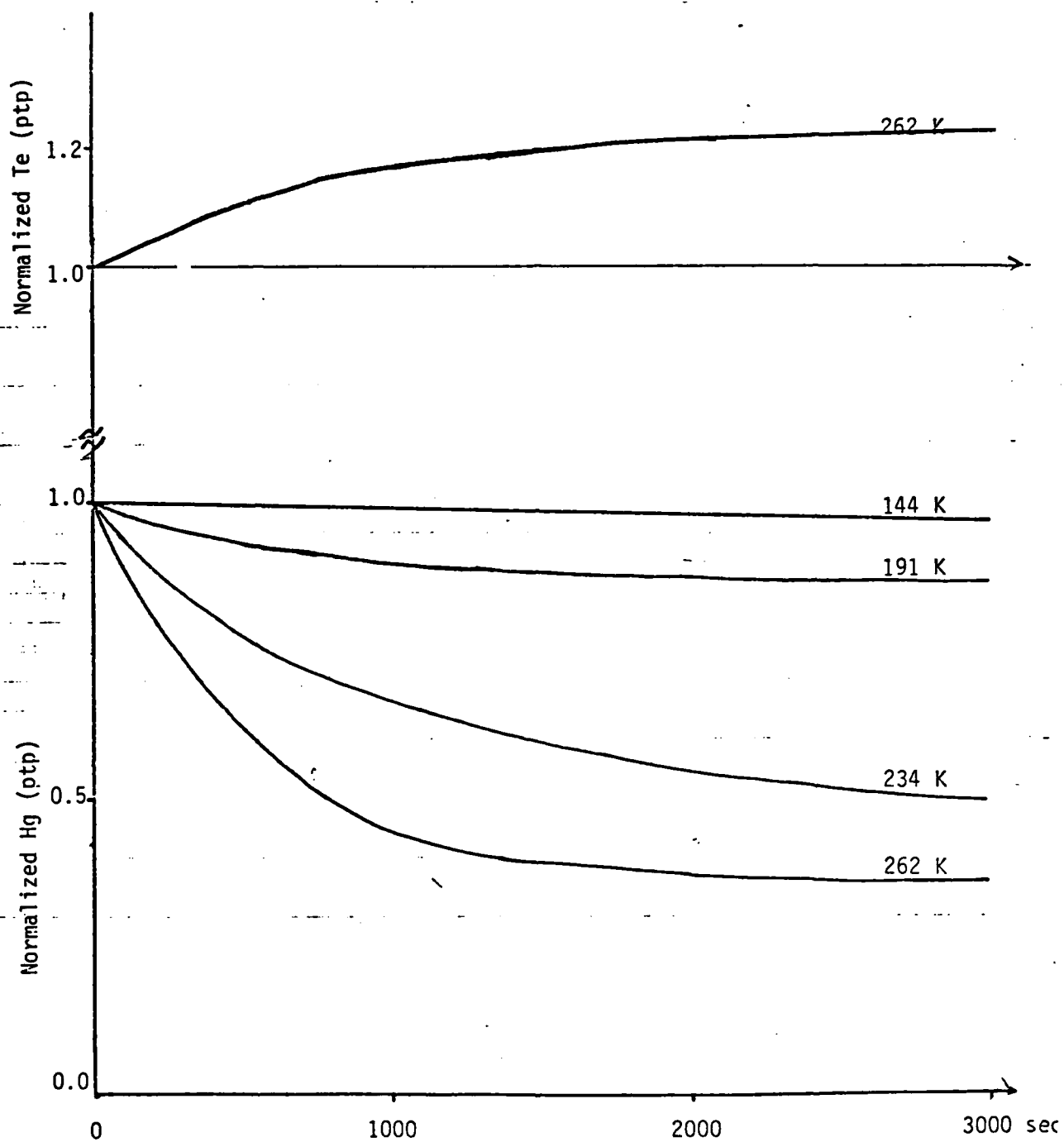


Fig.1 Auger signals of Hg and Te as a function of electron beam irradiation time.

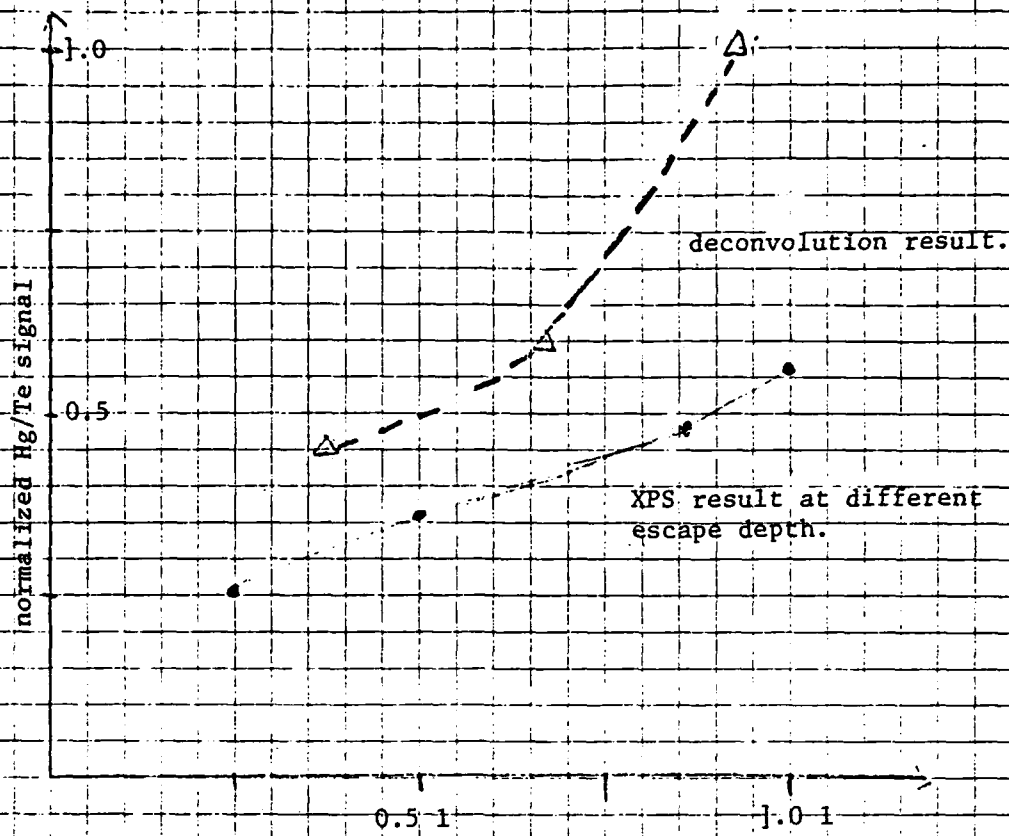


Fig. 2 XPS result of Hg 4f/Te 3d signal, normalized to that of cleaved surface. l =the escape depth of Hg 4f electrons which is approximately 20 Å

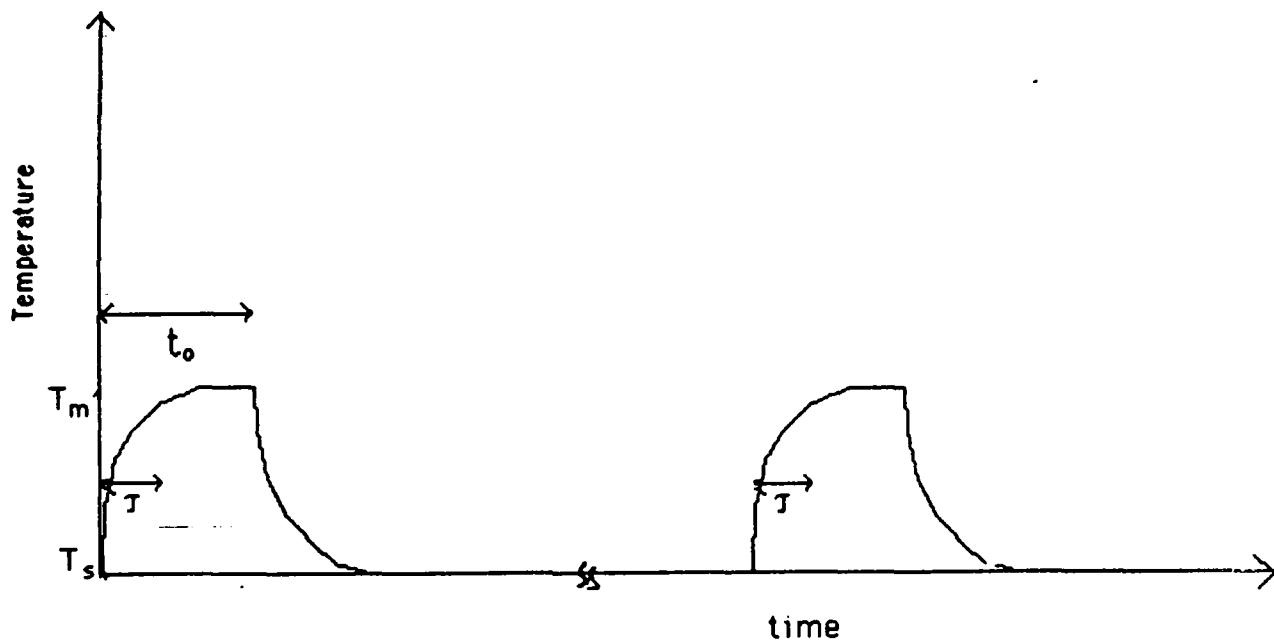


Fig. 3 Dynamical heating effect of a rastering electron beam where τ is the heating response time and t_0 is the duration time that an electron beam stay on a fixed position.

Metals on $\text{Hg}_{1-x}\text{Cd}_x\text{Te}$

D. J. Friedman

Introduction

In the past six months we have continued an investigation into the interaction of UHV-deposited metals with $\text{Hg}_{1-x}\text{Cd}_x\text{Te}$. The overall goal has been to understand the details of the interface: the chemical, physical (band bending) and stoichiometric effects on the metal and on the semiconductor substrate.

To approach this problem we have chosen to study metals which should represent both extremes of the reactivity spectrum. From heat-of-formation considerations, we picked silver for the representative nonreactive metal, and aluminum for the reactive case.

Results and Discussion:

1. Aluminum

As expected, the aluminum showed evidence of strong reaction with the $\text{Hg}_{1-x}\text{Cd}_x\text{Te}$ surface. The binding energy and lineshape of the Al 2p core level as a function of Al coverage showed an evolution from a reacted phase at low coverages into an unreacted peak at higher coverages (greater than about six Å). Furthermore, the Al 2p was discernible at coverages on the order of a tenth of a monolayer, suggesting that the aluminum sticks very strongly to the surface, neither flying off nor diffusing. The Hg, Cd and Te core levels showed significant binding energy shifts in the early stages of Al deposition, indicative of chemical reaction between the Al and the semiconductor.

Perhaps the most dramatic effect of the Al deposition was the depletion of

Hg from the $\text{Hg}_{1-x}\text{Cd}_x\text{Te}$ surface. The intensity of the Hg 4f core level decreases with increasing Al coverage much faster than the Te or Cd core levels attenuate, and indeed far too fast to be an escape depth effect. The Hg 5d level observed by UPS in a highly surface-sensitive regime attenuates even faster than the less surface-sensitive XPS Hg 4f signal, confirming that the depletion is strongest right at the interface. The character of this depletion has some interesting structure. Fig. 1 shows the logarithm of the Hg 4f intensity vs. Al coverage. The depletion rate can be seen to decrease at about 2 Å Al coverage. This change may mark the start of depletion of a second Hg layer, the completion of formation of an AlTe film, or possibly still other effects.

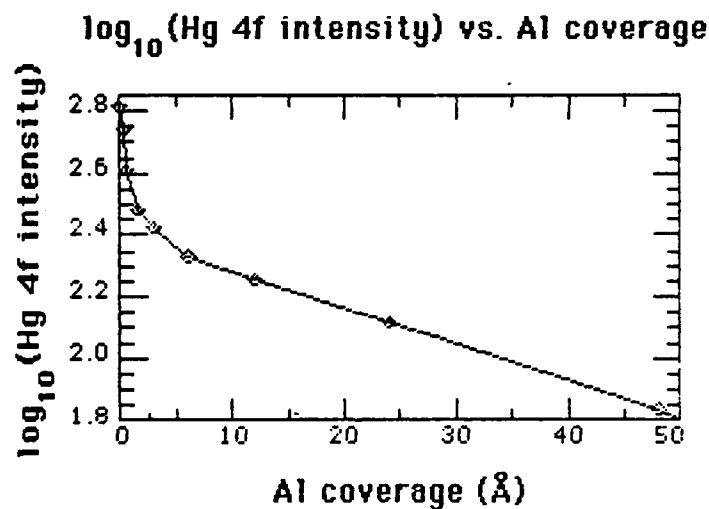


Figure 1

2. Silver

As expected, and in contradistinction to the case of Al, Ag shows weak chemical reaction with the $\text{Hg}_{1-x}\text{Cd}_x\text{Te}$ surface. No reacted phase of Ag was

ever visible; the only binding-energy evidence for any chemical effects was small Hg, Cd, and Te core level shifts. Another, less predictable, difference from the Al case was the behavior of the Ag on the surface at low coverages. The Ag was invisible by XPS and barely visible by UPS until about 2 Å was deposited. This would be consistent with islanding of the Ag on the semiconductor surface, or with a low sticking coefficient. However, since the Ag signal was stronger when viewed with greater surface sensitivity (UPS vs. XPS), diffusion into the bulk is unlikely.

More evidence for Ag islanding is provided by the behavior of the various core levels at high coverage. In this regime the Ag intensity still increases in an almost linear fashion, whereas for laminar coverage with a reasonable value for the electron escape depth the Ag signal would be seen to level off exponentially. Also, the Hg, Cd and Te core levels attenuate too slowly for the Ag coverage to be laminar.

In the case of Ag no obvious Hg depletion was seen. The reduction in the Hg intensity is believed to be due to attenuation by Ag. This is not surprising since the depletion seen in the case of Al is presumably driven by the chemical reaction with the $\text{Hg}_{1-x}\text{Cd}_x\text{Te}$. Fig. 2 shows the attenuation of the Hg 4f core level intensity as a function of coverage for Ag and Al. The extreme rapidity of the attenuation for the Al case is apparent.

Summary

As expected, the Al/ $\text{Hg}_{1-x}\text{Cd}_x\text{Te}$ interface is strongly reactive. There is a depletion of Hg from the surface of the semiconductor. The Ag/ $\text{Hg}_{1-x}\text{Cd}_x\text{Te}$ interface, on other hand, shows little evidence for chemical reaction. There is also little if any Hg depletion. However, the Ag does not go on in a simple,

laminar manner; rather, it appears to form islands at low coverages.

Hg 4f intensity vs. Al and Ag coverage

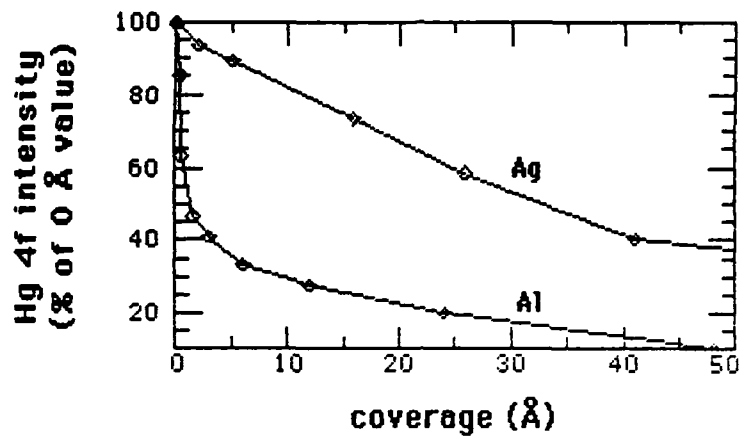


Figure 2

Section IV
ALLOY BONDING

Sensitivity of defect energy levels to host band structures

And impurity potentials in CdTe

A.-B. Chen,* Physics Department
Auburn University, Alabama 36849

A. Sher, SRI International
333 Ravenswood Avenue
Menlo Park, California 94025

The sensitivity of defect energy levels in semiconductors to the host band structures and impurity potentials has been studied for approximately 30 impurities in CdTe using four different band structure models. The discrepancies in the defect levels between two different sets of band structures and impurity potentials are found to range from less than 0.1 eV to the whole band gap (1.6 eV). The band-structure effects are analyzed here in terms of detailed partial densities of states. Examples of contradictory predictions from different band structures are illustrated, and ways to improve the theory are suggested.

I. INTRODUCTION

In several of our recent papers,¹⁻⁷ we have applied a method to calculate the band structure of semiconductors that is both efficient and accurate. Because the procedure involves casting the basis functions into orthonormal local orbitals (OLO),⁶ our method has the advantages common to empirical tight binding (ETB) calculations,⁸⁻¹⁰ except that the Hamiltonian matrix elements to all ranges are retained. The inclusion of these higher coefficients makes it possible to produce excellent band structures including conduction bands and effective masses. The method also yields wave functions for optical property calculations.⁷ Moreover, its OLO description also permits its extension, through the coherent-potential approximation, to alloys.²⁻⁵

The recent attention focused on defects in semiconductors motivated us to apply our method to this problem. The theories of defects have ranged from very sophisticated self-consistent density functional theory (SCDF)¹¹⁻¹³ to simple ETB calculations. It is generally recognized that SCDF is accurate in defects for the ground-state properties as it is for pure semiconductors, but less certain in assigning excited energy levels. ETB, because it can produce results for many systems in one study, claims to predict the trends of deep levels¹⁰ even if the accuracy for a given impurity may be poor. However, this contention remains to be verified.

To assess this concern, we ask the the question, "How sensitive are defect levels to host band structures and impurity potentials?" To this end, we have adopted the simple yet nontrivial defect model, that of site-diagonal substitutional defects often used in ETB studies. CdTe was selected in this study because its band structure has been examined in great detail by us, and there are three published band structure models⁸⁻¹⁰ that we could generate easily for comparison. There is also a considerable body of experimental data on deep states in this system.¹⁴⁻¹⁷

II. CALCULATIONAL PROCEDURE

In the simple site-diagonal substitutional defect model, the impurity energy levels E are determined by the equation

$$1 - v_{\alpha} g_{\alpha}(E) = 0 \quad , \quad (1)$$

where α designates the symmetry of a local state, e.g. Γ_6 , Γ_7 , and Γ_8 on an atomic site in the zinc-blende structure, and g_{α} is the real part of the diagonal matrix element of the host-crystal Green function. g_{α} can be calculated from the partial density of states (PDOS) by

$$g(E) = \int \rho_{\alpha}(\epsilon) / (E - \epsilon) d\epsilon \quad . \quad (2)$$

The PDOS is given by

$$\rho_{\alpha}(\epsilon) = \sum_{nk} |a_n^{\alpha}(k)|^2 \delta[\epsilon - \epsilon_n(k)] \quad , \quad (3)$$

where $\epsilon_n(k)$ are band energies and $a_n^{\alpha}(k)$ are the probability amplitudes of the band state in the Bloch basis constructed from the OLO labeled by α . The Brillouin-zone integration in Eq.(3) is calculated using an accurate ray scheme.¹⁸

Because a principal concern of this paper is the sensitivity of impurity levels to the host band structures, we should emphasize the difference between our method and ETB. Our method consists of four steps:

- (1) We start with four Gaussian orbitals per atom and empirical pseudo-potentials,¹⁹ and compute the Hamiltonian matrix $H(k)$ and overlap matrix $S(k)$ as was done by Kane²⁰ and Chadi.²¹
- (2) The Gaussian orbitals are transformed into OLO,⁶ so $H(k)$ is transformed into $H_0(k)$ and S into the identity matrix. The band structures calculated from $H_0(k)$ are accurate to 5 percent as compared to more sophisticated method using the same potential.¹
- (3) A spin-orbit Hamiltonian in the OLO basis⁴ is incorporated to deal with this interaction.
- (4) To compensate for the effects of truncated basis and nonlocal potentials, a perturbation Hamiltonian H_1 is added. H_1 has the same form as a truncated ETB Hamiltonian. The parameters in H_1 are adjusted to fine tune the important band energies and effective masses.¹⁻⁴

AD-R166 793

HGCDTE SURFACE AND DEFECT STUDY PROGRAM(U) SANTA
BARBARA RESEARCH CENTER GOLETA CALIF J A WILSON ET AL.
JAN 85 SBRC-52871 NDA903-83-C-0108

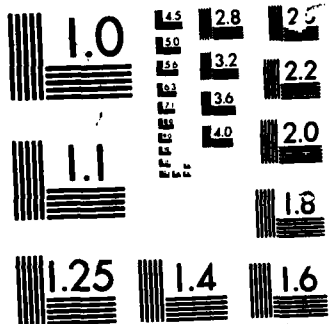
2/2

UNCLASSIFIED

F/G 20/12

NL





MICROCOPY

CHART

Although both ETB and our methods are empirical, there are two major differences:

- (1) While most ETB retains the H matrix elements only to the first- or second-neighbor shell, ours extend to all ranges, so the high Fourier components needed to produce the sharp band curvatures are properly given.
- (2) Our method can directly generate wave functions for calculation of other properties.

Thus, while our method yields more accurate band structures, it retains much of the advantage of ETB, namely the computational speed and a simple direct-space description of the Hamiltonian.

III. BAND STRUCTURES AND PARTIAL DENSITIES OF STATES

Figure 1 depicts the four band structures to be considered for CdTe. Our result is in panel a; panels b⁸ and c⁹ are two ETB band structures with the Hamiltonian matrix elements truncated at second neighbors. (Because different parameters were selected, these two band structures are not identical.) Panel d¹⁰ results from the use of five basis orbitals per atom; the extra one is an excited s-state. All these band structures are adjusted to have the proper fundamental band gap of 1.6 eV. The principal differences one sees on first inspection are in the band curvatures, especially the conduction bands. The effective mass at the bottom of the conduction band in panel a is 0.1 times the free-electron mass, in agreement with experiment,¹⁷ while in other panels it is more than twice as large.

Figure 2 shows the densities of states (DOS) for each of the band structures in Fig. 1. While the valence bands at least exhibit general common features, the conduction bands are almost unrecognizable as representing the same compound. In panel c and d, for example, there is a second band gap above the fundamental gap. Also note that there are two extra narrow peaks associated with the two extra excited s-orbitals (one for Cd and the other for Te) included in the calculation.

To analyze the band effects on defect levels (see Eqs. 1 and 2), the DOS is further decomposed into partial densities of states (PDOS) for $\Gamma_6(s)$, $\Gamma_7(p^{1/2})$, and $\Gamma_8(p^{3/2})$ states on the Cd and Te sites, as shown in Figs. 3, 4, 5, and 6. The Γ_8 PDOS are not shown, because they are nearly the same as Γ_7 with only a slight upward energy shift. These PDOS show how the "atomic" levels evolve into band states. These curves contain useful information about many properties, e.g. the relation between the crystal bonding and atomic energies, and how potential disorder in alloys affects different parts of the bands,²⁻⁵ in addition to defect levels studied here.

The $\Gamma_6(\text{Cd})$ PDOS shown in Fig. 3 split between the conduction and valence bands. It is generally assumed that the cation s-states in III-V and II-VI compounds evolve into the conduction bands, while the anion p-states make up most of the major valence bands just below the gap. Thus it is perhaps a surprise to see a prominent peak derived from the cation s-states at the bottom of the major valence-band structure. However, this is a general feature for all sp^3 -based compound semiconductors. These are the states responsible for the first observed

breakdown of the virtual-crystal approximation for a semiconductor alloy: $\text{Hg}_{1-x}\text{Cd}_x\text{Te}$ (which is caused by the large s-energy shift between the Cd and Hg sites).^{4,5,22}

A more detailed examination draws attention to some important differences among the four panels in Fig. 3: The valence-band peak in panel c is about 2 eV higher than the rest and is also high compared to experiment.²² Our conduction band PDOS in panel a is broader than the others. The ratio of the integrated PDOS in the conduction bands to that in the valence bands in our model is larger than those in other panels. Also our PDOS just below the valence-band edge is obviously smaller than that found in other models.

Figure 4 shows that the Cd p-states are concentrated in the conduction-band states. This is particularly true in panel a, where their contribution to the valence-band states shrinks almost to nothing. In other panels, there are still sizable (~20 percent) valence-band states. In contrast, all four panels in Fig. 5 show that the Te s-states are confined to the deep valence band states, as generally recognized. Finally, Fig. 6 shows that the Te p-states dominate the upper valence-band states. Panel a has much less valence-band content than the other three panels. As we will see, these differences can result in quantitatively or even qualitatively different predictions about the deep levels.

IV. IMPURITY LEVEL DETERMINATION

A convenient way to study the impurity energy levels using Eq. (1) is to rewrite it as $v_\alpha = 1/g_\alpha(E)$ and plot E as a function of v . Once this E - v curve is deduced for each α , the deep levels E_α for a given impurity can be read off the curve by drawing a vertical line at the appropriate value of v_α for the impurity. We set the zero of energy at the top of the valence bands. Because the gap is 1.6 eV, we will focus on levels in the energy range from -0.5 to 2.0 eV.

Calculations have been performed for all neutral impurities listed in Table I. Because we do not believe that there exists a uniformly accepted table for v we have adopted a table that we used for structural studies.^{23,24} Table I lists the term values, which we obtained from total energy differences between atomic configurations calculated using the norm-conserved pseudo-potentials²⁵ and self-consistent charge density functional theory, with the first ionization energies adjusted to be the experimental values.²⁶ These term values are found to yield consistently better structural properties²³ in Harrison's theory^{27,28} than those based on Mann's values²⁹ adopted by Harrison.²⁸ The impurity potential parameters will then be taken as the difference of the term values between the impurity atom and Cd (or Te). To study the sensitivity of E_α to v_α , we shift v_α by ± 0.5 eV and compute the corresponding changes in the energy levels.

Figures 7-10 display the E - v curves for several α . Each figure has four curves, corresponding to the four panels of PDOS in each of Figs. 3-6. The functional behavior of these curves can be understood

qualitatively using Eq. (2) and Figs. 3-6. If E lies in the gap, the contribution from conduction bands is negative, but positive from the valence bands. The closer the PDOS to the E in question, the larger will be its influence. Applying this argument to the $\Gamma_6(\text{Cd})$ representation, we see that the curves in Fig. 7 are negative in the gap region, because the PDOS in Fig. 3 near the bottom of the conduction bands are much larger than those near the valence-band top. Thus, on the Cd site, only impurities with an s -energy below the Cd s -level (-8.99 eV) will produce a Γ_6 level in the gap. However, we note that in Fig. 7, $g_\alpha(E) = 0$ for Model b and c just below the valence band edge, because of cancellation between the conduction and valence band contributions. At this E value, the E - v curve switches from $v = -\infty$ to $v = \infty$ (not shown); an ideal vacancy level (corresponding to $v_\alpha = \infty$) is located at this E . A similar consideration, but with the conduction and valence bands interchanged, leads to an understanding of the curves in Fig. 10. Using the same principle, we can easily understand why all curves in Fig. 9 for the $\Gamma_6(\text{Te})$ representation are positive, but the reasons for the large displacements between these curves are not easy to deduce. In Fig. 8, the curve labeled a is distinctively different from other curves, because the PDOS in panel a in Fig. 6 is completely dominated by the conduction band, but for the other panels the PDOS just below the valence band edge are as large as those just above the conduction band edge. This produces a very sharp negative E - v curve for a, but split behavior for b, c, and d.

These E-v curves provide a clear picture of how different host band structures may affect the deep levels. Numerical values for the impurity levels can be obtained from these figures by drawing vertical lines at the appropriate impurity potentials (i.e. differences between the term values listed in Table I), as has been shown for several representative impurities. To provide a more quantitative comparison, Table II lists some calculated impurity levels E_{α} and the corresponding changes ΔE_{α} due to 1-eV change in v_{α} .

V. RESULTS AND CONCLUSION

To summarize we recall that band Models b and c are the same second-neighbor ETB with two different sets of parameters, and Model d is a first-neighbor ETB with one extra s-orbital per atom. Our model (Model a) has the form of ETB but is derived in a very different manner, and includes all the long-range interactions. Therefore, we expect that the results from Models b and c will be close, Model d will have larger discrepancies from b and c than that between b and c, and Model a will differ even more. This is evident from Figs. 7 through 10 and Table 2. We found the energies for the $\Gamma_6(\text{Cd})$, $\Gamma_7(\text{Te})$, and $\Gamma_8(\text{Te})$ states produced by Models b and c agree within 0.1 eV. For the other states, i.e. $\Gamma_6(\text{Te})$, $\Gamma_7(\text{Cd})$, $\Gamma_8(\text{Cd})$, the energies from b and c are qualitatively similar, but the difference can be as large as 0.4 eV. The largest discrepancy between Model d and b (or c) is more than 0.5 eV, and that between a and other models is more than 1 eV. The largest difference

comes from the p-levels on a Cd site. For example, the filled p-level of C on a Cd site in Model a is a resonance state just below the valence band edge, but is a donor state in the other models. Similarly, Model a puts the neutral Te anti-site defect p-levels at about 1/3 and 2/3 of the gap [$E(\Gamma_7) = 0.48$ eV and $E(\Gamma_8) = 0.95$ eV], while other models assign them as resonance states inside the conduction bands. We also note that the discrepancies between different models are not uniform, but vary with v_α . Consider $\Gamma_6(\text{Cd})$ for example. All four models yield the same ordering and about the same energies for the group III impurities Al, In, and Ga. However, as v becomes more negative, the splitting between the curves increases, so the discrepancies become larger (~1 eV difference between Models a and d for I impurity). Similarly, for the $\Gamma_7(\text{Te})$ states, all four models put the Sn impurity energies close to valence band edge, but the agreement deteriorates as v_α increases.

Regarding the sensitivity of energy levels to impurity potentials, Table II shows that a 1-eV shift in v_α produces a change in E_α ranging from less than 0.1 eV to 0.65 eV. Very little is known about the size or trends in errors introduced in v_α from the use of atomic term values. However, we know that the discrepancy of v_α between two different tables of atomic term values can be larger than 2 eV. This discrepancy translates into an uncertainty of less than 0.1 to more than 1 eV in the impurity energy levels, which is comparable to that due to different host band structures.

Putting this large uncertainty in the deep levels against a band gap of 1.6 eV, we are left with great doubts about the predictability of this oversimplified theory. Unfortunately, the experimental means available for identifying micro-defects in semiconductors are still very limited, and the ab-initio band theory is still not capable of accurately predicting the energy levels. Thus, there is a great temptation to use simple theories like the one carried out here to help with the identifications. To illustrate this point, consider the following examples: Table II shows that Li on a Te site has an s-level of 0.14 eV in Model a, so one may be tempted to relate it to the acceptor state identified experimentally.¹⁴ However, this is not the hydrogenic acceptor state on a Cd site, as one might anticipate. One might also want to assign the 1/3 and 2/3 gap states for the Te anti-site p-levels on the Cd site found from Model a as those seen in experiments.^{15,16} Because of the large uncertainty in the calculation, these results should be regarded as suspicious surprises, rather than theoretical confirmations.

The results presented here should not discourage continued research on the ETB approach, but improvement is clearly needed. Work ranging from universal^{23,27,30} to specific^{24,31,32} structural studies to our band calculations and alloy studies¹⁻⁷ indicates that the ETB type of theory is practical for both bonding properties and electronic structures. The reason that ETB works well for some properties, e.g.

photoemission spectra and bonding properties, but not for impurity levels, is that the former depend only on the gross total density of states, while the latter have been shown to be sensitive to the details of the partial densities of states.

To establish the credibility of ETB in defect studies, one needs to look at the problem more seriously. The most difficult and yet important task is to develop a better way for determining the Hamiltonian matrix elements. Hass et al.⁸ and Harrison^{27,28} have suggested using the atomic term values as the diagonal matrix elements. Our work¹⁻⁴ has suggested using a universal long-range interaction to improve the accuracy of the conduction bands. Several studies^{1,27,28,33} have also pointed out scaling rules of the matrix elements. A combination of these ideas may lead to an acceptable model. Secondly, both the bonding and deep level states of impurities should be studied at the same time, in order to provide correlated information for defect identification. Finally, more realistic models should be examined. Besides the substitutional site-diagonal defects, one should consider the possibility of interstitial, paired, and even more complex defects. One also needs to deal with long-range impurity potentials, possible charge shifts, and lattice distortions. Progress in all these areas can be expected, if the calculation is constantly correlated with experiments and available ab-initio theory.



SANTA BARBARA RESEARCH CENTER
A Subsidiary

ACKNOWLEDGEMENT

This work was partially supported by AFOSR Contract F49620-81-K0012 and Grant AFOSR-84-0282.

REFERENCES

*Visiting professor at Stanford Univ.

1. A.-B. Chen and A. Sher, Phys. Rev. B, 22, 3886 (1980).
2. A.-B. Chen and A. Sher, Phys. Rev. B, 23, 5645 (1981).
3. A.-B. Chen and A. Sher, Phys. Rev. B, 23, 5360 (1981).
4. A.-B. Chen and A. Sher, J. Vac. Sci. Technol. 121, 138 (1982).
5. W.E. Spicer, J.A. Silberman, J. Morgan, J. Lindau, J.A. Wilson, A.-B. Chen, and A. Sher, Phys. Rev. Lett. 149, 948 (1982).
6. A.-B. Chen and A. Sher, Phys. Rev. B, 26, 6603 (1982).
7. A.-B. Chen, S. Phokaichaipatana, and A. Sher, Phys. Rev. B, 23, 5360 (1981).
8. K.C. Hass, H. Ehrenreich, and B. Velický, Phys. Rev. B, 27, 5360 (1983).
9. C.A. Swarts, M.S. Daw, and T.C. McGill, J. Vac. Sci. Technol. 121, 199 (1982).
10. A. Kobayashi, O.F. Sankey, and J.D. Dow, Phys. Rev. B, 25, 6367 (1982).
11. J. Bernholc, N.O. Lipari, and S.T. Pantelides, Phys. Rev. B, 21, 3545 (1980).

12. G.A. Baraff, E.O. Kane, and M. Schluter, Phys. Rev. B, 21, 5662 (1980).
13. G.B. Bachelet, M. Schluter, and G.A. Baraff, Phys. Rev. B, 27, 2545 (1983).
14. K. Zanio, "Cadmium Telluride," in Semiconductors and Semimetals, 13 (1978).
15. C.E. Jones, V. Nair, J. Lundquist, and D.L. Polla, J. Vac. Sci. Technol., 21, 187 (1982).
16. R.T. Collins and T.C. McGill, J. Vac. Sci. Technol., A1, 1633 (1983).
17. K.K. Kanazawa and F.C. Brown, Phys. Rev. 135, A1757 (1964).
18. A.-B. Chen, Phys. Rev. B16, 3291 (1977).
19. D.J. Chadi, J.P. Walter, and M.L. Cohen, Phys. Rev. B, 5, 3058 (1972).
20. E.O. Kane, Phys. Rev. B, 13, 3478 (1976).
21. D.J. Chadi, Phys. Rev. B, 16, 3572 (1977).
22. J.A. Silberman, P. Morgan, W.E. Spicer, and J.A. Wilson, J. Vac. Sci. Technol., 21, 142 (1982).
23. A.-B. Chen and A. Sher, "Bonding Theory of Semiconductor Alloys," Microscience, 3, "Materials for Microelectronics," A Multiclient publication of SRI International, Menlo Park, California (1984).

24. A. Sher and A.-B. Chen, and W.E. Spicer, Thirteen International Conference on Defects in Semiconductors, August 12-17, 1984, Coronado, California p. 43.
25. G.B. Bachelet, D. Hamman, and M. Schulter, Phys. Rev. B, 26, 4199 (1982).
26. C. Kittel, Introduction to Solid State Physics, 5th Edition (John Wiley and Sons, Inc., New York, London, Sidney, and Toronto, 1976), p. 75, Table 2.
27. W.A. Harrison, Electronic Structure and Properties of Solids (W.H. Freeman and Co., San Francisco, 1980).
28. W.A. Harrison, Microscience, Vol. 3 (a multiclient publication SRI International, Menlo Park, California (1983), p. 35.
29. J.B. Mann, "Atomic Structure Calculations, 1: Hartree-Fock Energy Results for Elements Hydrogen to Lawrencium," (Clearinghouse for Tech. Information, Springfield, Virginia, 1967).
30. D.G. Pettifor and R. Podloucky, Phys. Rev. Lett. 53, 826 (1984).
31. D.C. Allan and E.J. Mele, Phys. Rev. Lett., 53, 826 (1984).
32. D.J. Chadi, Phys. Rev. Lett., 52, 1911 (1984).
33. O.K. Andersen, W. Klase, and M. Nohl, Phys. Rev. B, 17, 1209 (1978).

FIGURE CAPTIONS

- Fig. 1 Four-band structures of CdTe used for comparative studies (a) present work, (b) Ref. 8, (c) Ref. 9, (d) Ref. 10.
- Fig. 2 Densities of states calculated from the four band structures in Fig. 1.
- Fig. 3 The Cd Γ_6 partial densities of states.
- Fig. 4 The Cd Γ_7 partial densities of states.
- Fig. 5 The Te Γ_6 partial densities of states.
- Fig. 6 The Te Γ_7 partial densities of states.
- Fig. 7 The E-v curves for the Γ_6 states on a Cd site.
- Fig. 8 The E-v curves for the Γ_7 states on a Cd site.
- Fig. 9 The E-v curves for the Γ_6 states on a Te site.
- Fig. 10 The E-v curves for the Γ_7 states on a Te site.

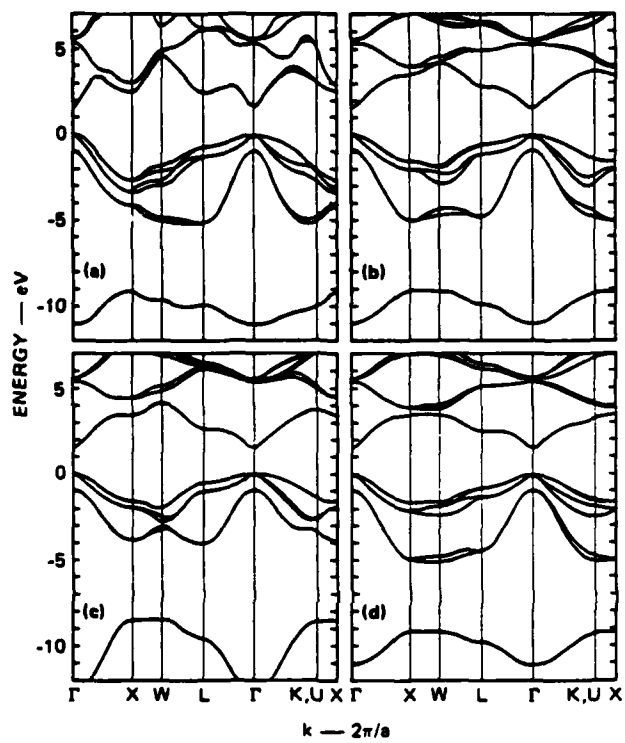


Figure 1

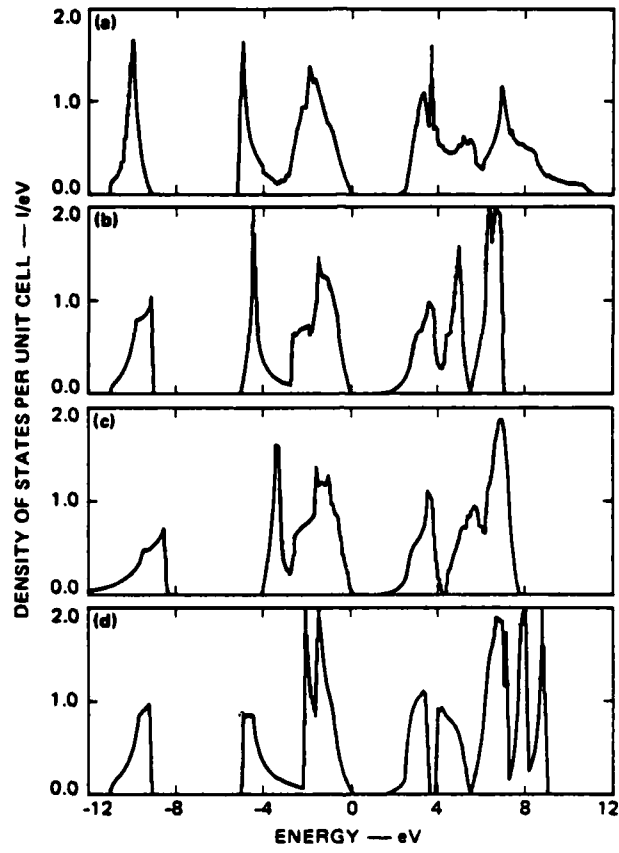


Figure 2

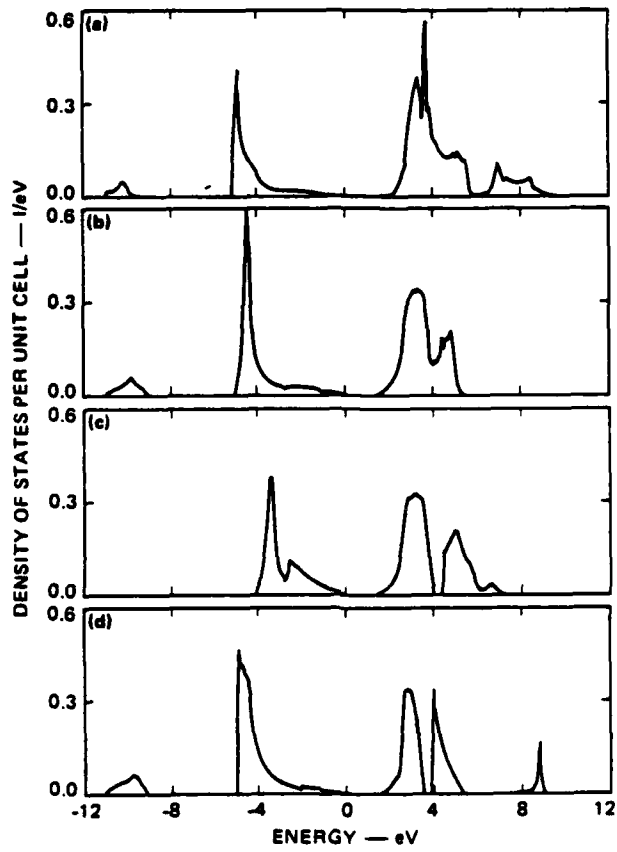


Figure 3

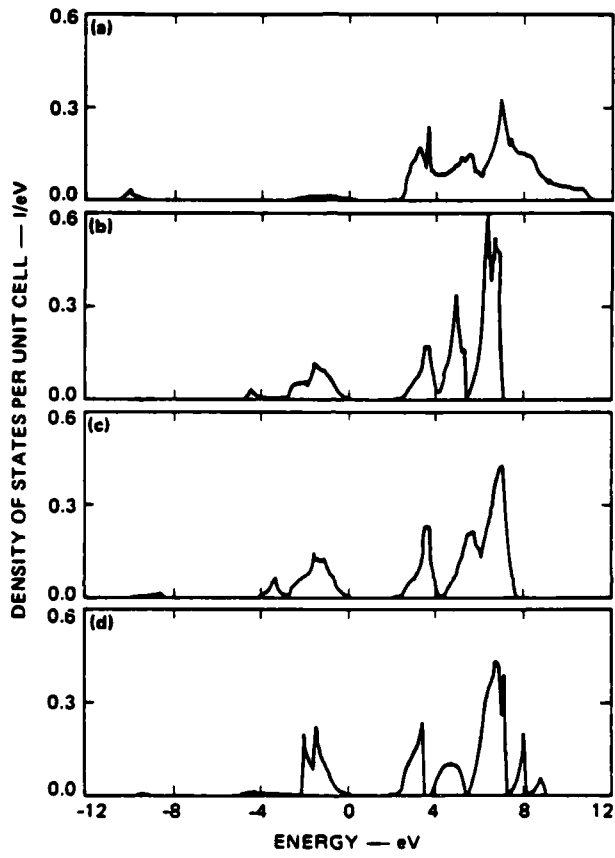


Figure 4

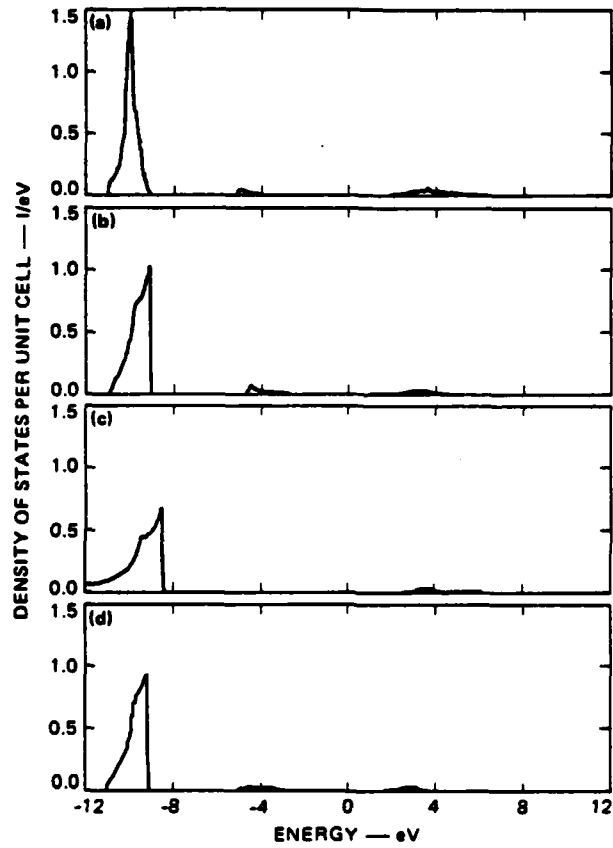


Figure 5

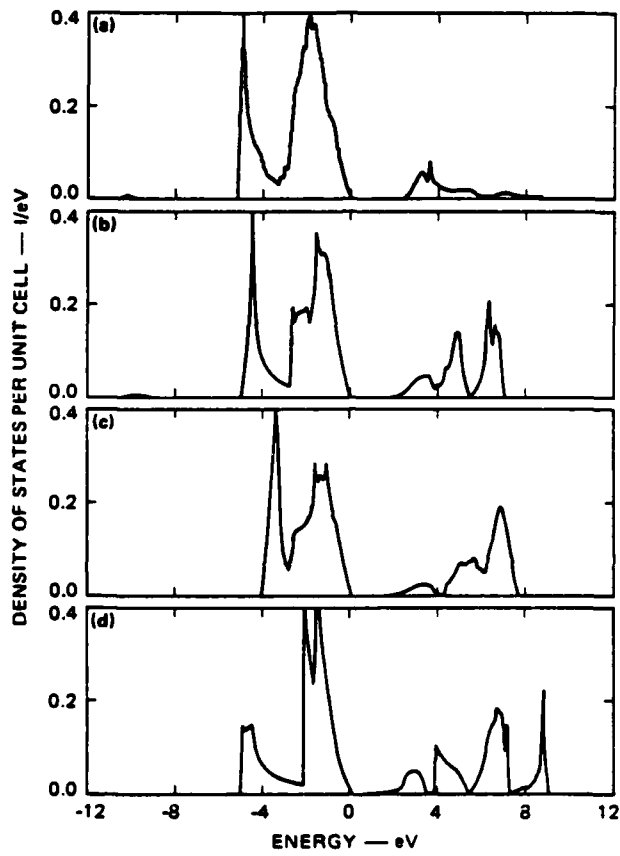


Figure 6

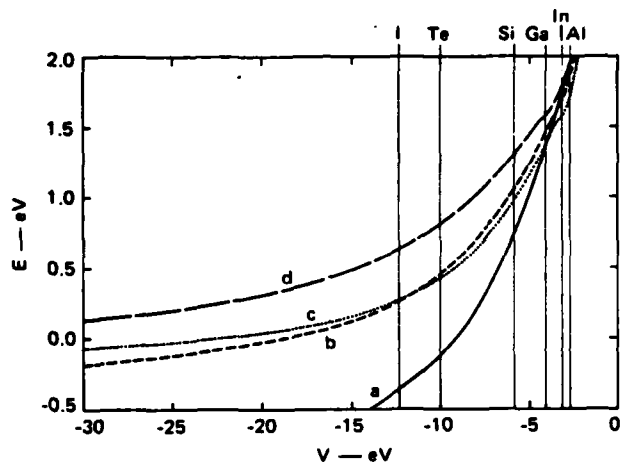


Figure 7

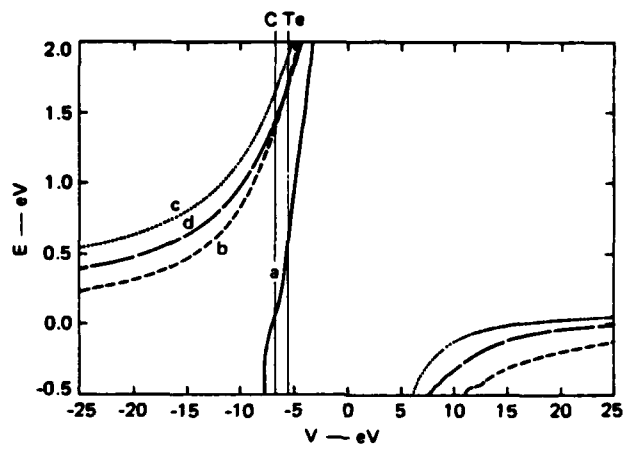


Figure 8

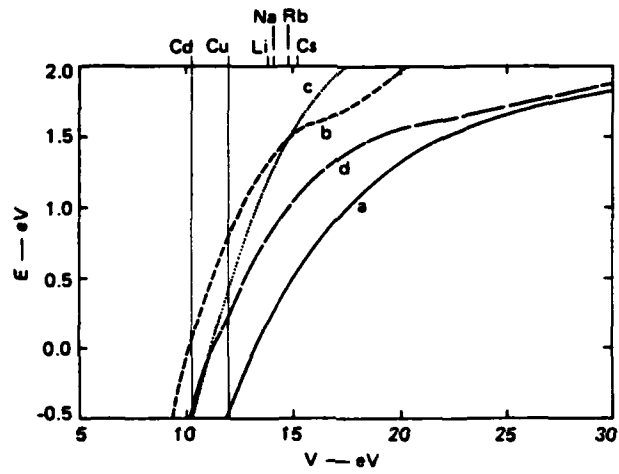


Figure 9

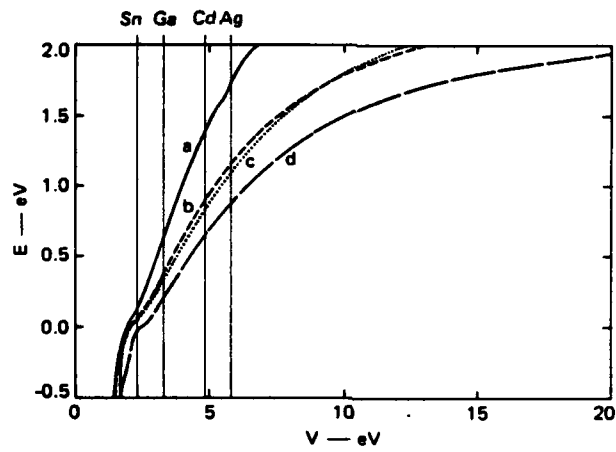


Figure 10

TABLE I. s- and p-state correlated term values in units of -eV.
 The top entry is the s-state, the second the $p_{1/2}$ -state, and
 the third the $p_{3/2}$ -state energy.
 (All energies are negative.)

I	II	III	IV	V	VI	VII
Li	Be	B	C	N	O	F
5.390	9.320	14.003	19.814	26.081	28.551	36.229
--	5.412	8.300	11.260	14.540	13.613	17.484
--	5.412	8.300	11.260	14.540	13.610	17.420
Na	Zn	Al	Si	P	S	Cl
5.140	9.390	11.780	15.027	19.620	21.163	25.812
--	4.237	5.980	8.150	10.610	10.449	13.136
--	4.011	5.980	8.150	10.550	10.360	13.010
K	Cd	Ga	Ge	As	Se	Br
4.340	8.990	13.230	16.396	20.015	21.412	24.949
--	4.313	6.000	7.880	10.146	10.188	12.353
--	4.097	5.850	7.694	9.810	9.750	11.840
Rb	Hg	In	Sn	Sb	Te	I
4.180	10.430	12.032	14.525	17.560	19.120	21.631
--	4.998	5.780	7.340	9.391	9.951	11.470
--	4.031	5.453	6.879	8.640	9.010	10.450
Cs			Pb			
3.890			15.250			
--			7.410			
--			5.979			
Cu						
7.720						
--						
--						
Ag						
7.570						
3.647						
3.487						
Au						
9.220						
4.349						
3.688						

TABLE II. Defect energy levels E and changes ΔE due to 1-eV change in the impurity potential parameter. All energies are in units of eV. VO stands for ideal vacancy.

Defect	Model a		Model b		Model c		Model d	
	E	ΔE						
Γ_6 on Cd site								
Ga	1.29	0.39	1.42	0.24	1.33	0.23	1.57	0.18
C	-0.21	0.09	0.38	0.09	0.36	0.13	0.74	0.08
Si	0.67	0.30	1.02	0.10	0.93	0.19	1.27	0.15
P	-0.19	0.11	0.39	0.09	0.38	0.08	0.75	0.08
O	<-0.5	--	-0.02	0.02	0.04	0.01	0.32	0.02
Te	-0.13	0.13	0.44	0.10	0.42	0.08	0.79	0.09
Cl	<-0.5	--	0.06	0.03	0.10	0.02	0.41	0.04
VO	<-0.5	--	<-0.5	--	-0.30	--	-0.20	--
Γ_7 on Cd site								
C	-0.02	0.37	1.32	0.22	1.59	0.20	1.39	0.19
Si	1.57	0.65	>2.0	--	>2.0	--	>2.0	--
P	0.16	0.38	1.48	0.26	1.73	0.23	1.52	0.21
O	<-0.5	--	0.89	0.14	1.22	0.13	1.03	0.12
Te	0.48	0.55	1.60	0.29	1.88	0.23	1.66	0.24
Cl	<-0.5	--	0.96	0.17	1.29	0.14	1.09	0.14
VO	<-0.5	--	0.00	--	0.21	--	0.06	--
Γ_6 on Te site								
Li	0.14	0.29	1.28	0.22	1.15	0.35	0.76	0.25
Cu	<-0.5	--	0.54	0.42	0.12	0.52	0.03	0.32
Γ_7 on Te site								
Ag	1.89	0.32	1.26	0.22	1.21	0.23	0.99	0.20
Cd	1.66	0.34	1.11	0.26	1.05	0.26	0.85	0.22
Ga	0.98	-0.49	0.61	0.33	0.55	0.32	0.40	0.30
Si	-0.07	0.40	-0.11	-0.36	-0.13	0.38	-0.38	0.72
Sn	0.28	0.47	0.15	0.31	0.13	0.24	0.02	0.28

END
FILMED

5-86

DTIC